UNIVERSITY OF CALIFORNIA
RIVERSIDE

Designing New Structures of Magnetic Materials: Cases of Metal Borides and Metal Chalcogenides

A Dissertation submitted in partial satisfaction
of the requirements for the degree of

Doctor of Philosophy

in

Chemistry

by

Jan Phillip Scheifers

March 2020

Dissertation Committee:
Dr. Boniface B. T. Fokwa, Chairperson
Dr. Ming Lee Tang
Dr.Yadong Yin

The Dissertation of Jan Phillip Scheifers is approved:

Committee Chairperson

University of California, Riverside

Für Papa

Acknowledgments

Some of the research presented in here has previously been published as:

Jan P. Scheifers, Boniface P. T. Fokwa: *Unprecedented Selective Substitution of Si by Cu in the New Ternary Silicide $Ir_{4-x}CuSi_2$*. Manuscript submitted to Z. Kristallogr. Cryst. Mater.

Ryland Forsythe, Jan P. Scheifers, Yuemei Zhang, Boniface Tsinde Polequin Fokwa: *HT-NbOsB: Experimental and Theoretical Investigations of a New Boride Structure Type Containing Boron Chains and Isolated Boron Atoms*. European Journal of Inorganic Chemistry 02/2018; 2018(28)., DOI:10.1002/ejic.201800235

Jan P. Scheifers, Michael Küpers, Rashid Touzani, Fabian C. Gladisch, Rainer Poettgen, Boniface P. T. Fokwa: *1D iron chains in the complex metal-rich boride $Ti_{5-x}Fe_{1-y}Os_{6+x+y}B_6$ ($x = 0.66(1)$, $y = 0.27(1)$) representing an unprecedented structure type based on unit cell twinning*. Manuscript in preparation

Jan. P Scheifers, Boniface P.T. Fokwa: *Follow the boride brick road: paving the way towards rational structure design*. Manuscript in preparation

Jan P. Scheifers, Nika G. Bakshi, Justin Flores, Boniface P.T. Fokwa: *High-T_c, ferromagnetic boride $TiFe_{1-x}Os_{2+x}B_2$*. Manuscript in preparation

Palani R. Jothi, Jan P. Scheifers, Yuemei Zhang, Mohammed Alghamdi, Dejan Stekovic, Mikhail E. Itkis, Jing Shi, Boniface Tsinde Polequin Fokwa: *$Fe_{5-x}Ge_2Te_2$ - A New Exfoliable Itinerant Ferromagnet with High Curie Temperature and Large Perpendicular Magnetic Anisotropy*. physica status solidi (RRL) - Rapid Research Letters 12/2019;, DOI:10.1002/pssr.201900666

I would like to thank all co-authors, in particular my co-first authors. R. Forsythe and M. Küpers for their contributions. Other manuscripts, that have been published while in the Graduate Program at UC Riverside, but which are not explicitly part of the dissertation are listed below:

Melina Witt, Judith Bönnighausen, Fabian Eustermann, Aline Savourat, Jan P. Scheifers, Boniface P.T. Fokwa, Carsten Doerenkamp, Hellmut Eckert, Oliver Janka: E*xtending the knowledge on the quaternary rare earth nickel aluminum germanides of the $RENiAl_4Ge_2$ series (RE=Y, Sm, Gd–Tm, Lu) – structural, magnetic and NMR-spectroscopic investigations*. Zeitschrift fur Naturforschung B 01/2020;, DOI:10.1515/znb-2019-0176

Amir A. Rezaie, Zheng Yan, Jan P. Scheifers, Jian Zhang, Juchen Guo, Boniface P. T. Fokwa: *Synthesis and Li-ion Electrode Properties of Layered MAB phases $Ni_{n+1}ZnB_n$ (n = 1, 2)*. Journal of Materials Chemistry A 01/2020; 8(4)., DOI:10.1039/C9TA12937E

Abishek K. Iyer, Yuemei Zhang, Jan P. Scheifers, Boniface P.T. Fokwa: *Structural variations, relationships and properties of M_2B metal borides*. Journal of Solid State Chemistry 12/2018; 270., DOI:10.1016/j.jssc.2018.12.014

Linxiao Geng, Jan P. Scheifers, Jian Zhang, Krassimir N. Bozhilov, Boniface P. T. Fokwa, Juchen Guo: *Crystal Structure Transformation in Chevrel Phase Mo_6S_8 Induced by Aluminum Intercalation*. Chemistry of Materials 11/2018; 30(23)., DOI:10.1021/acs.chemmater.8b03312

Pritam Shankhari, Jan P. Scheifers, Martin Hermus, Kunio Yubuta, Boniface P. T. Fokwa: *Unexpected Trend Deviation in Isoelectronic Transition Metal Borides $A_3T_5B_2$ (A = group 4, T = group 9): $Ti_3Co_5B_2$- vs. Perovskite-Type Studied by Experiments and DFT Calculations*. Zeitschrift für anorganische Chemie 10/2017; 643(21)., DOI:10.1002/zaac.201700271

Palaini R Jothi, Yumei Zhang, Jan P. Scheifers, Hyounmyung Park, Boniface P. T. Fokwa: *Molybdenum diboride nanoparticles as highly efficient electrocatalyst for the hydrogen evolution reaction*. 09/2017; 1(9)., DOI:10.1039/C7SE00397H

Hyounmyung Park, Yuemei Zhang, Jan P. Scheifers, Palani R. Jothi, Andrew Encinas, Boniface P. T. Fokwa: *Graphene-and Phosphorene-like Boron Layers with Contrasting Activities in Highly Active Mo_2B_4 for Hydrogen Evolution*. Journal of the American Chemical Society 09/2017; 139(37)., DOI:10.1021/jacs.7b07247

Linxiao Geng, Jan P. Scheifers, Chengyin Fu, Jian Zhang, Boniface P. T. Fokwa, Juchen Guo: *Titanium Sulfides as Intercalation-Type Cathode Materials for Rechargeable Aluminum Batteries*. ACS Applied Materials & Interfaces 06/2017; 9(25)., DOI:10.1021/acsami.7b04161

Hyounmyung Park, Andrew Encinas, Jan P. Scheifers, Yuemei Zhang, Boniface P. T. Fokwa: *Boron-Dependency of Molybdenum Boride Electrocatalysts for the Hydrogen Evolution Reaction*. Angewandte Chemie International Edition 04/2017; 56(20)., DOI:10.1002/anie.201611756

Hyounmyung Park, Andrew Encinas, Jan P. Scheifers, Yuemei Zhang, Boniface P. T. Fokwa: *Boron-Dependency of Molybdenum Boride Electrocatalysts for the Hydrogen Evolution Reaction*. Angewandte Chemie 04/2017; 129(20)., DOI:10.1002/ange.201611756

Jan P. Scheifers, Yuemei Zhang, Boniface P. T. Fokwa: *Boron: Enabling Exciting Metal-Rich Structures and Magnetic Properties*. Accounts of Chemical Research 08/2017; 50(9)., DOI:10.1021/acs.accounts.7b00268

I would also like to thank all co-authors of those publications for their contribution and their input. Moreover, I acknowledge the financial support by UC Riverside (Dissertation Year Award) and the NSF (CARRER award to Dr. Fokwa, DMR-1654780).

Furthermore, I would like to thank everybody who helped me - in whichever way - to get to the point in my life at which I am writing the final words of this – my – dissertation:

First and foremost, I would like to thank my advisor, Dr. Boniface Fokwa, for the opportunity to work in his group, for his guidance and advice, his trust and support, his time and patience as well as for the freedom to focus on what I found most interesting. I am very grateful for this and everything else he has done for me.

Moreover, I would like to thank the master students Ryland Forsythe and Michael Küpers, whom I got to work with and who made a made big contribution to this thesis. I may very well have learned more from them than they have learned from me and this thesis would not be the same without their hard work.

I had the great pleasure to work with several highly talented undergraduate students, Vikas Shulka, Raymond D. Nguyen, Justin Flores and Nika G. Bakshi. They worked under my guidance in the laboratory and they prepared sample mixtures and carried out syntheses and I am very thankful for their help.

I would like to take the chance to thank my coworkers in the Fokwa group at UC Riverisde, Ardalan Rezaie, Eunsoo Lee, all my former coworkers, Dr. Pritam Shankhari, Dr. Hyounyoung Park, Dr. Martin Hermus, Dr. Mohammed Mbarki, Dr. Rachid Touzani, Andreas Möller as well as Dr. Teresa Ortner and Dr. Abishek Iyer for their support and

their friendship. I could not have been luckier that they happened to work in the same laboratory with me. I am very grateful that we got the chance to work together, solve problems together, share ideas and become friends.

This acknowledgment section would not be complete without me trying to express how thankful I am Dr. Yuemei Zhang, also a former coworker in the Fokwa group. She is not only a great solid-state chemist but an amazing person. She was and still is always willing to answer my questions. She listened to all my ideas, no matter how stupid they were.

I am deeply grateful for the unconditional love and support of my friends and family in Riverside, in Aachen, in Wuppertal, or wherever they may be. For reasons I do not understand, they stuck with me in good days and in bad days and I do not think I could be any luckier to have them in my life. They mean the world to me… and then I found a Crystal in the hallway and I lost my heart. Until then I thought I could not be happier, but I was wrong.

I think at this point it is quite obvious that I do not know the right words in neither German nor English (or any other language) to express how thankful I am, so I will finally stop attempting to do so here. I am certain that I forgot to mention someone here and it is impossible to list everyone who supported me, but that does not mean that I am less thankful for them.

Thank you so much everyone.

ABSTRACT OF DISSERTATION

Designing New Structures of Magnetic Materials through Structural Relationships: Cases of Metal Borides and Metal Chalcogenides

by

Jan Phillip Scheifers

Doctor of Philosophy, Graduate Program in Chemistry
University of California, Riverside, March 2020
Dr. Boniface P. T. Fokwa, Chairperson

We are in the middle of a changing paradigm in solid-state chemistry: shifting away from analyzing the structures of crystalline compounds to understand the structure-property relations towards the targeted synthesis of new materials with properties desirable for specific applications – known as the materials-by-design strategy.

This approach requires control over the obtained products and their structures, which is still an enormously challenging task, especially for intermetallics. Intermetallics are non-molecular crystalline solids based on two or more metals with a stoichiometry that is not continuously variable and for which the crystal structure differs from the structure of the involved elements. Metal-rich borides are a subgroup of intermetallics with huge structural variety and highly interesting properties. Many metal borides are hard (or even superhard), have extremely high melting points, and exhibit fascinating magnetic properties (if they contain magnetically active elements).

This work primarily focuses on metal-rich borides and their structural relations, but it includes some chalcogenides as well. A ternary niobium boride, $Nb_{1-x}Os_{1+x}B$ with a new

crystal structure was discovered, presenting itself to be a missing link. Its discovery led to the identification of a new class of borides containing over a dozen different crystal structures. The structure-building principles were explored, and it was found that all of these crystal structures can be described using the same primary and secondary building blocks. The structure of $Ti_{5-x}Fe_{1-y}Os_{6+x+y}B_6$, another boride in a new crystal structure with interesting magnetic properties due to 1-dimensional Fe-chains, can be explained in the same conceptual framework. Moreover, for the first time, hitherto unknown crystal structures with exciting magnetic properties can be predicted by applying these structure-building principles. The new $TiFe_{1-x}Os_{2+x}B_2$, which was predicted using such principles, is one of the few ternary metal-borides without rare-earth elements that is ferromagnetic above room temperature.

The structure-building principles with their predictive power can serve as guidelines for obtaining metal borides with specific properties. Therefore, they are an important step towards materials-by-design. Moreover, they could aid in understanding how and why observed structures form while others do not, a crucial step to control and ultimately manipulate the formation of these compounds in the future.

Table of Contents

List of Tables

List of Figures

Chapter 1: Introduction

Starting with the new millennium, we have witnessed a change of paradigm in solid-state chemistry. Instead of understanding each structure and the corresponding structure-property relation for newly synthesized compounds before finding potential applications, specific properties for applications are aimed for, when planning the synthesis of compounds.

However, this approach requires sufficient control over the experimentally obtained product and its structure. Control over the product's crystal structure is still a major challenge in the field of intermetallic compounds, where most new crystal structures to this day are found serendipitously.

What is needed to predict the outcome of a synthesis and to target certain properties are reliable structure-building principles to rationally design crystal structures and tailor material's properties to their intended application.

Structure-building principles have been developed parallel to the discovery of crystal structures over the last century starting shortly after the discovery of X-ray diffraction [1,2]. Initially simple concepts like closely packed spheres [3,4] and ionic radii ratios [5] were developed and turned out to be extremely helpful in order to understand many relatively simple crystal structures and compounds. Later, other concepts like the intergrowth method for intermetallics [6] or the principle of secondary building units in zeolites [7,8] were established. But these rules or guidelines fall short for compounds with a more complex bonding situation like it is encountered in intermetallic borides.

Boron was synthesized from boric acid in the early years of the 19th century before it was recognized as an element in 1824 [9,10]. Since then, it has been the subject of many studies, because of its unique chemical properties, which are the result of its tendency to form covalent bonds combined with being electron-deficient, i.e. more valence orbitals than valence electrons. This is displayed in the dimer formation of borane or the dodecaborate anion $[B_{12}H_{12}]^{2-}$ [11]. The icosahedral structure resulting from 3-center-2electron bonds is a common motif in highly boron-rich compounds and in many of its allotropes. To this day boron and its compounds remain a challenge in the solid-state community [12]. Only recently - 200 years after its discovery - the ground-state allotrope of boron seems to finally be identified [13].

Compounds of boron and metals are called borides and come in hundreds of different structures; some extremely boron-rich such as YB_{66} [14], some containing only a very small amount of boron such as $Nd_2Fe_{14}B$ [15]. They are classified according to their metal-to-boron ratio (M:B) [16]. The boron-rich borides (M:B > 4) contain a 3-dimensional B-framework with the metal atoms located in voids in the framework. Very metal-rich borides (M:B > 3) on the other hand contain individual B-atoms in a metal matrix.

Boron's electron deficiency is also reflected in the compounds it forms and their M:B ratio. Taking the binary metal boride with the highest M:B ratio for each metal $(M:B)_{max}$, we find that the average $(M:B)_{max}$ of each group of the periodic table increases with the group number (see **Figure 1**).

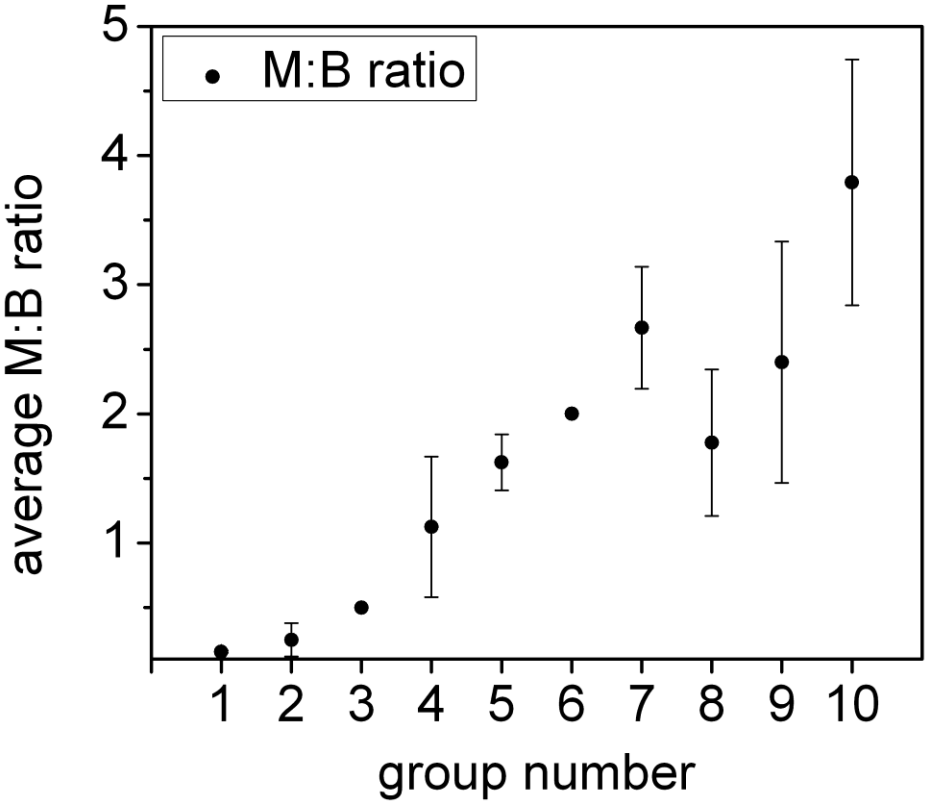

***Figure 1**: average M:B ratio of the most metal-rich binary boride*

That is, because the more valence electrons the metal atom has the fewer boron-boron bonds are necessary to compensate for the electron deficiency. Alkaline metals only have one VE, which is shared with the boron atoms, so many B-B bonds are needed, which results in a 3-dimensional B-network with many B- and few metal-atoms. Metals like Ir or Pd have many VE, which can participate in bonding necessitating fewer B-B bonds and resulting in higher M:B ratios.

The research presented here will focus on metal-rich borides with $1 < M:B < 8$. For metal borides with M:B around 2, many different structures have been reported [17]. Several of which contain small, "molecule-like" boron units, with B─B distances around 1.8 Å. Such short interatomic distances are commonly identified as indicator for a covalent B─B bond. All these B_n-units can be considered small fragments of the infinite, graphene-like honeycomb B-layers of the AlB_2-type structure [18]. The B_n-fragments are representative for the covalent bonding in metal borides. But metallic bonding and (partial) charge transfer also contribute to the chemical bonding in these compounds making their chemical description not straightforward, which in turn results on the one hand in not obvious structure-building principles and on the other hand a unique set of physical properties.

Borides exhibit a huge variety of highly useful properties. Very boron-rich borides are semiconductors just like elemental boron itself, upon increasing M:B ratio they become metallic due to the increasing portion of metallic bonding. In some cases such as TiB_2, the electrical conductivity can exceed the conductivity of the corresponding metal despite containing 67 at.-% boron [19].

The covalent bonds contribute to the high hardness and incompressibility as well as to the high melting points of metal borides. This makes them very useful as cutting tools or as wear-resistant coatings. ReB_2 was found to be superhard (for small indentation loads) and able to scratch diamond [20].

YB_{66} is the boride with the lowest M:B ratio that adopts its own crystal structure. Its large face-centered cubic unit cell contains over 1500 B-atoms, most of which are part of the

characteristic B_{12}-icosahedra [21]. Due to the heavy Y and its large lattice parameter (a = 23.4 Å), it is used as a monochromator in X-ray optics.

LaB_6 is used as a thermionic emitter in electron optics, because of its low work function [22].

MgB_2 is another boride with highly exciting properties. Like many other borides it becomes superconductive. Its unusually high critical temperature of 39 K makes it unique among non-copper-oxide superconductors [23]. MgB_2 coils are used as electromagnets in scientific equipment such as MRI instruments, particle accelerators and nuclear fusion experiments [24].

In contrast, $Nd_2Fe_{14}B$ is a very metal-rich boride, which is used not as an electromagnet, but as permanent magnet in various applications. It is the strongest commercially available permanent magnet (by energy product) [15] and it is used in many applications ranging from hard disks over speakers to all kinds of electric motors.

One of the core-projects in the Fokwa group has been directed towards finding and enhancing new permanent, but rare-earth free boride magnets. In previous studies, 1-dimensional (1D) chains of magnetically active *3d*-elements have been identified as structural features that show promising magnetic properties. Several compounds with such structural motifs have been synthesized and fine control of their magnetic properties has been achieved by manipulating both the magnetically active metal as well as the surrounding metal atoms [25–28].

In this thesis, structure-building principles for a new class of metal-rich borides are identified, explored and finally used to make predictions of new crystal structure, which will enable the rational design of (magnetic) metal-rich borides. Furthermore, multiple new compounds and crystal structures in this class of materials have been experimentally obtained, their crystal structure analyzed in detail and some of their properties characterized.

Moreover, some of the principles are shown to be useful for different types of materials as well. The valence electron (VE) count is found to play a very important role in the class of Re_3B-based borides as it determines the electronic stability in this class of borides. However, it provides a stability range for boride perovskites and explains the unprecedented substitution of Si by Cu in the newly discovered $Ir_{4-x}CuSi_2$. The intergrowth principle on the other hand is applied to rationalize the structures of Fe_3GeTe_2 and $Fe_5Ge_2Te_2$ which allows the prediction of the series $(Fe_2Ge)_n(FeTe_2)$.

The compounds in the series $(Fe_2Ge)_n(FeTe_2)$ belong to the emerging group of 2-dimensional (2D), van der Waals magnets, that has attracted immense scientific interest over the last couple of years [29–31]. Van der Waals (vdW) materials are layered chalcogenides, for which the lone pairs of two adjacent chalcogenide-layers point towards each other [30]. Consequently, there are no strong chemical bonds such as covalent or ionic bonds present between the two layers resulting in thin slabs – usually only a few atoms thick – stacked on top of each other and held together by weak vdW interactions. Over the last 15 years after the discovery of graphene many 2D materials

have been discover, many of which are vdW materials such as Molybdenum disulfide (MoS_2) [32]. However, only about a handful of them intrinsically contain magnetically active *3d*-metals like Fe_3GeTe_2, $Cr_2Ge_2Te_6$ are $MnBi_2Te_4$ [33–35]. These materials and their exfoliated monolayers are predicted to be a key component in future spintronic, where digital information is processed in form of magnetic spins.

This dissertation consists of the relevant manuscripts written for publication with each chapter representing an individual manuscript or parts thereof, which have been or will be published as a journal article. As such, each chapter contain detailed information on the experimental procedures and methods making a chapter on methods redundant. In **chapter 2**, a new ternary niobium osmium boride and its crystal structure are presented, which turned out to be a missing link in the structure-building principles. Next in **chapter 3**, the crystal structure of the new boride, $Ti_{5-x}Fe_{1-y}Os_{6+x+y}B_6$, is introduced which is closely related to the aforementioned niobium osmium boride. In **chapter 4**, a new group of complex metal-rich borides is identified and common the structure-building principles are postulated and correlated to the existing crystal structures. Based on the principles elucidated in **chapter 4**, a new metal-rich Osmium boride with magnetically active *3d*-metal and its magnetic properties is presented in **chapter 5**. In **chapter 6**, a new ternay Iridium silicide is presented representing how structure-building principles can also apply for intermetallics other than borides. Before ending with a short summary and concluding remarks in **chapter 8**, the crystal structure of $Fe_{5-x}Ge_2Te_2$ is presented and the intergrowth series $(Fe_2Ge)_n(FeTe_2)$ is established in **chapter 7**.

References

1. Eckert, M. Max von Laue and the discovery of X-ray diffraction in 1912. *Ann. Phys.* **524**, A83–A85 (2012).

2. Bragg, W. H. & Bragg, W. L. The reflection of X-rays by crystals. *Proc. R. Soc. London. Ser. A, Contain. Pap. a Math. Phys. Character* **88**, 428–438 (1913).

3. Conway, J. H. Sphere Packings, Lattices, Codes, and Greed. in *Proceedings of the International Congress of Mathematicians* 45–56 (Birkhäuser Basel, 1995). doi:10.1007/978-3-0348-9078-6_7.

4. Weisstein, E. W. Sphere Packing.

5. Pauling, L. THE PRINCIPLES DETERMINING THE STRUCTURE OF COMPLEX IONIC CRYSTALS. *J. Am. Chem. Soc.* **51**, 1010–1026 (1929).

6. Grin', Y. N. The Intergrowth Concept as a Useful Tool to Interpret and Understand Complicated Intermetallic Structures. in *Modern Perspectives in Inorganic Crystal Chemistry* 77–96 (Springer Netherlands, 1992). doi:10.1007/978-94-011-2726-4_5.

7. Baerlocher, C., McCusker, L. & Olson, D. *Atlas of zeolite framework types*. (2007).

8. Gramlich-Meier, R. & Meier, W. M. Constituent units and framework conformations in zeolite networks. *J. Solid State Chem.* **44**, 41–49 (1982).

9. Davy, H. III. The Bakerian Lecture. An account of some new analytical researches on the nature of certain bodies, particularly the alkalies, phosphorus, sulphur, carbonaceous matter, and the acids hitherto undecompounded; with some general observations on chemical. *Philos. Trans. R. Soc. London* **99**, 39–104 (1809).

10. Berzelius, J. J. Untersuchungen über die Flussspatsaure und deren merkwürdigste Verbindungen. *Ann. Phys.* **10**, 113 (1824).

11. Pauling, L. THE ARCHITECTURE OF MOLECULES. *Proc. Natl. Acad. Sci.* **51**, 977–984 (1964).

12. Albert, B. & Hillebrecht, H. Boron: Elementary Challenge for Experimenters and Theoreticians. *Angew. Chemie Int. Ed.* **48**, 8640–8668 (2009).

13. White, M. A., Cerqueira, A. B., Whitman, C. A., Johnson, M. B. & Ogitsu, T. Determination of Phase Stability of Elemental Boron. *Angew. Chemie Int. Ed.* **54**, 3626–3629 (2015).

14. Richards, S. M. & Kaspar, J. S. The crystal structure of YB66. *Acta Crystallogr. Sect. B Struct. Crystallogr. Cryst. Chem.* **25**, 237–251 (1969).

15. Givord, D., Li, H. S. & Moreau, J. M. Magnetic properties and crystal structure of Nd2Fe14B. *Solid State Commun.* **50**, 497–499 (1984).

16. Rogl, P. Competition Between Trigonal Prisms and other Coordination Polyhedra in Borides, Carbides, Silicides and Phosphides. in *Modern Perspectives in Inorganic Crystal Chemistry* 267–278 (Springer Netherlands, 1992). doi:10.1007/978-94-011-2726-4_13.

17. Iyer, A. K., Zhang, Y., Scheifers, J. P. & Fokwa, B. P. T. Structural variations, relationships and properties of M2B metal borides. *J. Solid State Chem.* **270**, 618–635 (2019).

18. Scheifers, J. P., Zhang, Y. & Fokwa, B. P. T. Boron: Enabling Exciting Metal-Rich Structures and Magnetic Properties. *Acc. Chem. Res.* **50**, 2317–2325 (2017).

19. Rahman, M., Wang, C. C., Chen, W., Akbar, S. A. & Mroz, C. Electrical Resistivity of Titanium Diboride and Zirconium Diboride. *J. Am. Ceram. Soc.* **78**, 1380–1382 (1995).

20. Chung, H. Y. *et al.* Synthesis of ultra-incompressible superhard rhenium diboride at ambient pressure. *Science (80-.).* **316**, 436–439 (2007).

21. Wong, J. *et al.* YB66: A new soft-X-ray monochromator for synchrotron radiation. *Nucl. Inst. Methods Phys. Res. A* **291**, 243–249 (1990).

22. Lafferty, J. M. Boride cathodes. *J. Appl. Phys.* **22**, 299–309 (1951).

23. Nagamatsu, J., Nakagawa, N., Muranaka, T., Zenitani, Y. & Akimitsu, J. Superconductivity at 39 K in magnesium diboride. *Nature* **410**, 63–64 (2001).

24. Tomsic, M. *et al.* Overview of MgB_2 Superconductor Applications. *Int. J. Appl. Ceram. Technol.* **4**, 250–259 (2007).

25. Hermus, M., Yang, M., Grüner, D., DiSalvo, F. J. & Fokwa, B. P. T. Drastic Change of Magnetic Interactions and Hysteresis through Site-Preferential Ru/Ir Substitution in $Sc_2FeRu_{5-x}Ir_xB_2$. *Chem. Mater.* **26**, 1967–1974 (2014).

26. Mbarki, M., St. Touzani, R. & Fokwa, B. P. T. Unexpected Synergy between Magnetic Iron Chains and Stacked B_6 Rings in $Nb_6Fe_{1-x}Ir_{6+x}B_8$. *Angew. Chemie Int. Ed.* **53**, 13174–13177 (2014).

27. Fokwa, B. P. T., Lueken, H. & Dronskowski, R. Rational Design of Complex Borides - One-Electron-Step Evolution from Soft to Semi-Hard Itinerant Ferromagnets in the New Boride Series Ti2FeRu5-nRhnB2 ($1 \leq n \leq 5$). *Eur. J. Inorg. Chem.* **2011**, 3926–3930 (2011).

28. Fokwa, B. P. T., Eck, B. & Dronskowski, R. Ti2Rh6B - a new boride with a double perovskite-like structure containing octahedral Rh6 cluster. *Zeitschrift für Krist.* **221**, 445–449 (2006).

29. Huang, B. *et al.* Layer-dependent ferromagnetism in a van der Waals crystal down to the monolayer limit. *Nature* **546**, 270–273 (2017).

30. Ajayan, P., Kim, P. & Banerjee, K. Two-dimensional van der Waals materials. *Phys. Today* **69**, 38–44 (2016).

31. Burch, K. S., Mandrus, D. & Park, J. G. Magnetism in two-dimensional van der Waals materials. *Nature* vol. 563 47–52 (2018).

32. Fleischauer, P. D., Lince, J. R., Bertrand, P. A. & Bauer, R. Electronic structure and lubrication properties of molybdenum disulfide: a qualitative molecular orbital approach. *Langmuir* **5**, 1009–1015 (1989).

33. Deiseroth, H.-J., Aleksandrov, K., Reiner, C., Kienle, L. & Kremer, R. K. Fe3GeTe2 and Ni3GeTe2 – Two New Layered Transition-Metal Compounds: Crystal Structures, HRTEM Investigations, and Magnetic and Electrical Properties. *Eur. J. Inorg. Chem.* **2006**, 1561–1567 (2006).

34. Gong, C. *et al.* Discovery of intrinsic ferromagnetism in two-dimensional van der Waals crystals. *Nature* **546**, 265–269 (2017).

35. Li, J. *et al.* Intrinsic magnetic topological insulators in van der Waals layered MnBi2Te4-family materials. *Sci. Adv.* **5**, eaaw5685 (2019).

Chapter 2: A New Ternary Boride Structure Type Containing Boron Chains and Isolated Boron Atoms - Experimental and Theoretical Investigations of $Nb_{1-x}Os_{1+x}B$

Ryland Forsythe, Jan P. Scheifers, Yuemei Zhang, and Boniface P.T. Fokwa

Abstract

Single crystals and bulk samples of the new ternary compound $Nb_{(1-x)}Os_{(1+x)}B$ (x = 0.17) were synthesized by arc-melting of the elements in a water-cooled crucible under an argon atmosphere. The samples were characterized by X-ray diffraction and energy-dispersive X-ray spectroscopy (EDX) measurements. Furthermore, the crystallographic, electronic, and bonding characteristics have been studied using density functional theory. The title compound crystallizes with a new orthorhombic structure type in the space group *Pnma* (no. 62) with the lattice parameters a = 11.283(2) Å, b = 3.0101(4) Å, and c = 12.883(2) Å. The structure contains isolated boron atoms in osmium trigonal prisms, and infinite boron chains in face-sharing niobium trigonal prisms. Electronic structure relaxation has confirmed the crystallographic parameters, and crystal orbital Hamilton population (COHP) bonding analysis was used to understand the chemical bonding. It is shown that a local stabilizing effect from replacing Nb with Os is favored despite a global destabilization. It is suggested that a Group VI metal may be more appropriate for the niobium sites.

Introduction

The family of metal-rich borides displays a staggering array of crystal structures which exhibit diverse chemical and physical properties, and are increasingly gathering the attention of solid-state chemists, material scientists and physicists. [12,36–38] There are many common structural motifs in these compounds, mainly controlled by the metal to boron ratio. Isolated boron atoms tend to occur in high M:B ratios, such as in the M_3B (M=Re, Tc) or $Ti_3Co_5B_2$ type structures. [39,40] These isolated boron atoms are commonly found at the center of a trigonal prism made up of metal atoms (MB_6). At lower M:B ratios, around 2:1, more diverse boron fragments are formed, such as B_2 dumbbells, B_4 or B_5 [41] chains or trigonal planar fragments, or B_6 rings. [36] In all these cases, the metal atoms form an arrangement of trigonal prisms, which are connected by a shared rectangular face. This allows boron atoms to form covalent B-B bonds. If all those prisms then share two of their rectangular faces with neighboring prisms at a 1:1 metal to boron ratio infinite zig zag boron chains are formed, such as the FeB, CrB, and MoB structure types. [42] In MoB alternating boron chains are arranged perpendicularly to each other, in contrast to the parallel arrangement in CrB and FeB. The chains in FeB are canted with respect to each other, compared to the CrB chains which are all zig zag along the same direction. For even lower M:B ratios boron layer and 3D networks are observed. In all cases these M:B ratios serve as guidelines more than rules.

Moving from binary systems to ternaries and beyond, the picture becomes even more complex. Due to different electronegativities, sizes, affinities, etc., between the metals different boron fragments can form with each metal, which allows for an interesting

fragment-based approach to these crystal systems. Many combinations have been previously reported, including isolated boron atoms inside trigonal prisms together with most of the fragments listed above. A few examples include $Re_5Co_2B_4$ (isolated B and B_2 dumbbells) [43], $Ti_7Rh_4Ir_2B_8$ (isolated B and B_6 rings) [44], and $Ti_{1+x}Rh_{2-x+y}Ir_{3-y}B_3$ (isolated B and zig-zag B4 chains). [45] Interestingly, there is already a known NbOsB compound with the $Ti_{1+x}Rh_{2-x+y}Ir_{3-y}B_3$ structure type, which contains zigzag B_4-units. [46] Herein, we report on the synthesis, crystal chemistry, electronic structure and chemical bonding analysis of a new high temperature modification of this compound adopting a new structure type in which isolated B and infinite zigzag B-chains exist, a combination which has only been found in the o-Ni_4B_{3-x} structure. [47,48]

Results and Discussion

The $Nb_{(1-x)}Os_{(1+x)}B$ phase was synthesized using a 1:2:2 (Nb:Os:B) ratio for the starting pellet. This produced 62.4(9) wt% of the $Nb_{(1-x)}Os_{(1+x)}B$ (*Pnma,* no. *62*) phase, obtained from the Rietveld refinement of the powder data. It was observed that the side product (elemental osmium) had slightly larger lattice parameters than the literature values, which suggests interstitial atom (boron) or substitution with the larger Nb, or both. The data and lattice parameters from this refinement are summarized in Table S1 and Figure S2 of the appendix. The refinement model is in close agreement with the single crystal refinement below (**Table 1**). EDX of a single crystal confirmed the metal ratio, which showed a Nb:Os ratio of 2.5:3.3 (Figure S3), which is in good agreement with the single crystal refinement considering the rough surface of the crystal.

Table 1: *Single crystal refinement parameters of* $Nb_{0.84}Os_{1.17}B$.

Formula weight (g/mol)	310.17
F (000)	127.7
Crystal size (mm)	0.03 x 0.02 x 0.10
θ range (°)	$3.159 \leq \theta \leq 33.794$
hkl range	$-17 \leq h \leq 16$
	$-4 \leq k \leq 4$
	$-19 \leq l \leq 19$
Reflections (independent reflections)	4692 (991)
Number of parameters refined	49
Space group; Z	*Pnma* (no. 62), 12
a (Å)	11.283(2)
b (Å)	3.0101(4)
c (Å)	12.883(2)
V (Å^3)	437.54(5)
Calculated density (g cm^{-3})	14.105
Absorption coefficient μ (mm^{-1})	8.84
Absorption correction	Numerical
GooF	1.118
*R*1; *wR*2	0.0441; 0.0938
Difference peak/hole (e Å^{-3})	5.02/-4.92
ICSD entry no.	433752

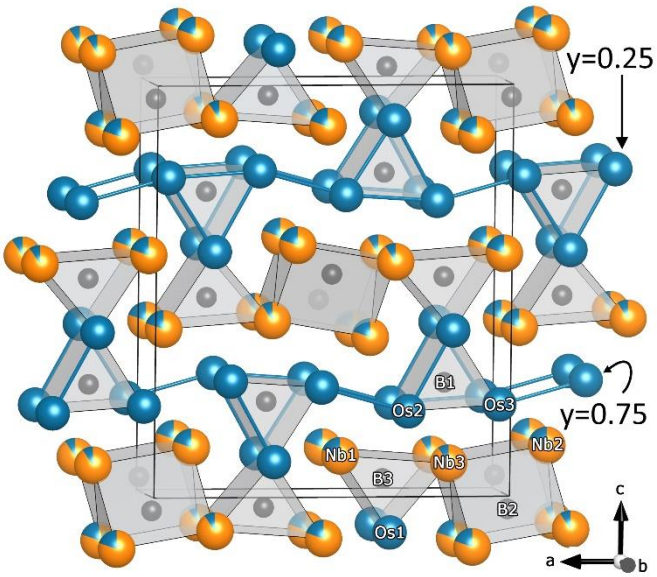

Figure 2: *The extended structure of $Nb_{1-x}Os_{1+x}B$, looking down the b-direction. Both atoms form trigonal prisms with boron centers, in perpendicular directions to each other. From this direction the osmium substructure is clear. Alternating layers are offset in the b-direction.*

After solving the structure (orthorhombic space group *Pnma*), all niobium sites were found to be partially occupied by osmium (niobium occupancies: 0.80(1), 0.80(1), 0.90(1), respectively). The mix-occupancies lead to a $Nb_{0.84(1)}Os_{1.17(1)}B$ stoichiometry which can be generalized by the formula $Nb_{1-x}Os_{1+x}B$, where the maximal amount of osmium x = 0.17(1) at the niobium sites has probably been reached because excess of osmium was used during the synthesis. The partial occupancies were also found in the powder data [Nb: 0.82(3), 0.79(3), 0.87(3), respectively].

This new structure type (**Figure 2**) is composed of two main subunits, the first being the infinite boron chain extending into the *b*-direction. This chain is contained within face sharing niobium prisms, each of which shares two of its three faces. All three niobium sites reside in fully capped pentagonal prisms (**Figure 3**) which have the large pentagonal face perpendicular to the *b* direction. In addition, osmium atoms partially occupy all

niobium sites. The other subunit is composed of osmium trigonal prisms, all of which contain a boron atom. These trigonal prisms are bound to adjacent osmium prisms at two of their three corners; the third is corner sharing with a mixed trigonal prism, which serves as a link between the two subunits. This mixed trigonal prism is corner sharing with both the osmium trigonal prisms and the niobium trigonal prisms. Because the niobium and osmium triangular prisms are perpendicular to each other, each osmium layer is offset from the next by half of the length of the *b*-direction.

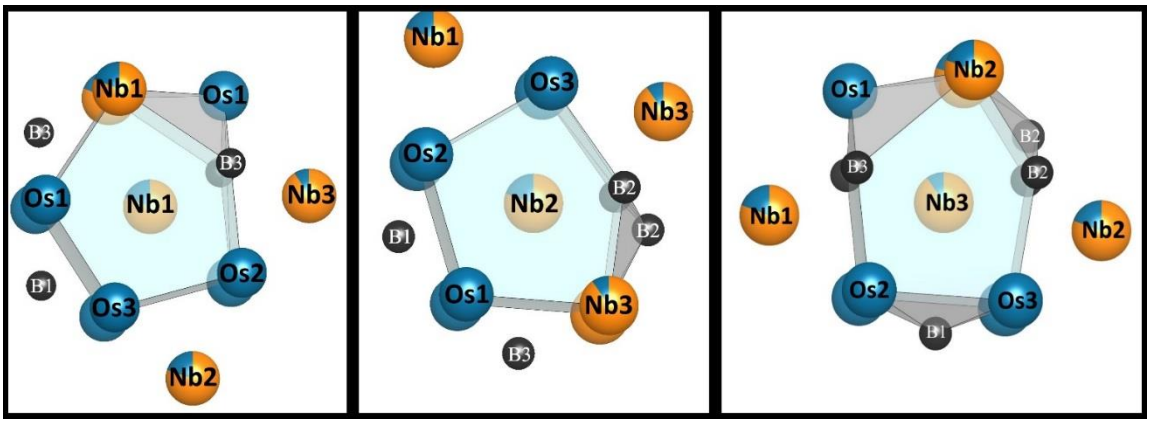

Figure 3: *The coordination polyhedra for the three niobium positions. In this paper, niobium atoms will be shown in orange, osmium in blue, and boron in black. All polyhedra here are fully capped pentagonal prisms.*

The $Nb_{1-x}Os_{1+x}B$ structure (**Figure 2**) is strikingly similar to the orthorhombic Ni_4B_{3-x} structure (**Figure 4**, left), sharing the same *Pnma* space group and very similar lattice parameters [$a = 11.9540(8)$, $b = 2.9815(3)$, $c = 6.5684(5)$]. [47] Both contain infinite boron chains perpendicular to the layer of boron-filled trigonal prisms. However, in the Ni_4B_{3-x} structure, the prisms containing the boron chains are corner sharing in the *c*-direction, whereas in the $Nb_{1-x}Os_{1+x}B$ structure they are separated by different trigonal prisms. This can be related to the M:B ratios, 2:1 vs 4:3, where the ratio with higher boron content

(that of Ni_4B_{3-x} structure) leads to more boron chain fragments and thus to condensation of their prisms sharing. These metal trigonal prisms are also offset by half a length in the *b*-direction, due to the staggering of the chain fragment. This new structure also shares many similarities to the recently discovered NbRuB (*Pmma*) [49] and the $Ti_{1+x}Rh_{2-x+y}Ir_{3-y}B_3$ (*Pbam*, also adopted by the LT NbOsB) [45] structure types (**Figure 4**, middle and right, respectively), such as late transition metal (osmium, ruthenium) forming trigonal prisms which are connected via inter-prism bonds and contain isolated boron atoms. These prisms form puckered layers in the *ab*-plane, shown in **Figure 2**. The Os_6B prisms are the same as the Re_3B substructure in NbRuB. [49] In contrast to the NbRuB structure, the layers of Os_6B prisms in the $Nb_{1-x}Os_{1+x}B$ structure are offset by half a length in the b direction (**Figure 2**). In the present case, the Os_6B prism offset is compensated by the niobium prisms, which are aligned perpendicularly and face sharing. In the NbRuB structure, the niobium and boron form trigonal Nb_6B prisms, which are alternatingly face sharing and edge sharing along the *a*-direction, with B_2-dumbbell pairs forming in the face sharing trigonal prisms. However, in the new $Nb_{1-x}Os_{1+x}B$ structure,

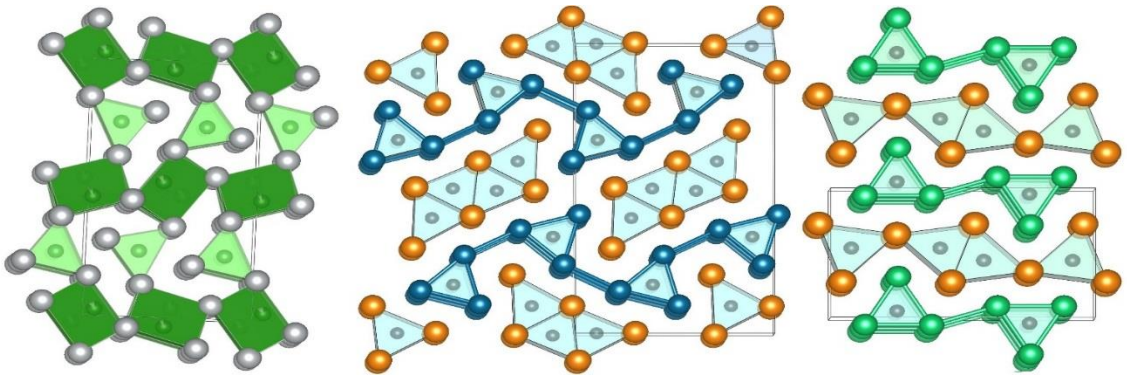

***Figure 4**: The Ni_4B_{3-x} (Left: Pnma, 62), NbOsB (Middle: Pbam, 55, $Ti_{(1+x)}Rh_{(2-x)}Ir_3B_3$ type), and NbRuB (Right: Pmma, 51) structures are shown for comparison. Nickel is shown in grey and ruthenium is shown in bright green.*

the Nb_6B prisms are always sharing two faces with each other forming chains in the *b*-direction. This is extremely similar to the boron chain found in FeB. [42] This perpendicular arrangement of trigonal prisms is in contrast with the typical parallel alignment found in metal-rich borides. [36]

It is interesting to calculate the volumes of the niobium prisms, to see if the discrepancy in the partial osmium substitutions could be structurally driven. The calculated volumes are as follows: V_{Nb1}=38.6 Å^3, V_{Nb2}=36.3 Å^3, and V_{Nb3}=33.9 Å^3. The volume decreases from the coordination prisms Nb1 to Nb2, and to Nb3. At first glance, it would appear that Nb1 and Nb2 would be similar in volume, and they would if it were not for the rather large difference in one of the metal-boron bonds. The metallic bonds are all of similar length, and so is one of the metal-boron bonds. However, the bond between Nb1 and B3 is 2.89 Å in the Nb1 polyhedra, whereas in the Nb2 polyhedra the B2-Nb3 bond is only 2.51 Å. Combining the decreasing volume for the three polyhedra with the fact that niobium is a larger metal than osmium, which would lead to the expectation of niobium being preferentially on a larger site (Nb1), it becomes clear that the main driving force for Nb/Os substitution is not structural. Something unusual for borides are the mixed trigonal Nb_4Os_2B prisms on B3, with two niobium atoms and one osmium atom on each triangular face, which connect the face-sharing niobium FeB fragments to the extended osmium layers. Similar mixed trigonal prisms can be found in the TiNiSi (*Pnma,* no. 62), $Ti_{(1+x)}Rh_{(2-x)}Ir_3B_3$, and NbCoB (*Pmnn*, no. 59) structure types, amongst others. B1coordination is similar environment, but the prism in this case is entirely osmium. Of

note is that both prisms are fully capped. Both B1 and B3 coordination are significantly different from B2, which makes up the boron chain. This chain has a bond angle of 116.2(8)^{o}, which is different from the ideal 120^{o} if the boron sat at the center of an equilateral prism. The boron sits in an off-center position in all three polyhedra. For B1 and B3 this is due to the anisotropic coordination environment.

For the B2 infinite chain, the distortion is primarily due to the distortion of the niobium prisms in the FeB fragment. Compared to the ideal NbB structure [50], the Nb-Nb distance in the trigonal face of the prisms has been compressed roughly 10%, from 3.3 Å to 2.95 Å. At the same time, the Nb-Nb distance parallel to the boron chain has been compressed from 3.16 Å to 3.01 Å. However, the aspect ratio for both structures is almost identical, at 0.96 for NbB, and 0.95 for the structure reported here. This compression also explains the shortened B-B bond distance, from 1.86 Å in NbB to 1.77 Å here. This bond length is on the shorter end of the typical range of B-B bonds, which falls between 1.7 and 1.9 Å [51], and is reasonable considering the atomic radius of boron is ~0.8 Å. Because the 3.01 Å Nb-Nb bond length in the *b* direction is linked to the height of the osmium trigonal prisms, there is a structural balance between compressing the niobium bonds and stretching the osmium bonds. Thus, the smaller osmium atom substituting onto the niobium sites may occur in part to relieve the strain resulting from this imbalance. Also, it may be possible that a larger atom on the osmium sites would relieve some of this stress and allow the niobium fragment to relax. Finally, the angle between sites Nb2-Nb3-Nb2 is not a perfect 90^{o}, but is actually 88.6^{o}, meaning the FeB fragment actually has a

parallelogram cross-section. The niobium richer Nb3 site is pushed slightly further apart due to a larger average size, and the Nb2 site is brought together. This distortion supports the mixed occupancy found in the single crystal refinement.

Chemical Bonding Analysis

Chemical bonding analysis was carried out by using the crystal orbital Hamilton population (COHP) approach. [52] These populations were integrated up to the Fermi energy to obtain a semi-quantitative value (ICOHP) which reflects the bond strength between a pair of atoms. Calculations are done on the $Nb_{(1-x)}Os_{(1+x)}B$ composition with x=0, and we have evaluated the effects of the osmium substitution by shifting the Fermi energy relative to the band structure according to the rigid band model. The ICOHP approximates bond strength, where an increase in the negative ICOHP represents a stronger bond, and vice versa. As a general trend, osmium interactions show a decrease in the -ICOHP with an increased VEC, while niobium interactions that did not include osmium show a larger increase in the -ICOHP. By comparing the ICOHP values for the different bonds in the structure (Table S4, supporting information), a sense of which interactions are stronger or weaker can be established.

COHP plots for some representative bonds are shown in Figure 4. The COHP plots suggest that Nb-Nb and Nb-B interactions still have bonding states above the Fermi level which can be filled with additional electrons (**Figure 5**, left). In contrast, Os-Nb and Os-B interactions are forced to populate antibonding bonds (**Figure 5**, right). Neither Os-Os

bonds nor the B2-B2 chain are significantly impacted. In particular, the face sharing niobium trigonal prisms, benefit immensely from the osmium substitution. This suggests that the substitution results in strongly stabilized Nb-Nb interactions, despite a small overall destabilizing effect. Interestingly, the site with the least substitution is also the site with the smallest coordination environment, even though osmium is a smaller atom than niobium. This is the opposite of what would be expected and suggests the driving force is more electronic than structural. The Nb3 site is the only metal site that is coordinated to both the infinite boron chain and isolated boron atoms.

By examining this site in the context of boron rich borides, the higher niobium occupancy makes sense. Boron rich metals are typically formed with earlier transition metals, due to their relatively lower electronegativity. [53] Accordingly, the Nb3 site prefers less Os and more Nb than the other two Nb sites. Looking at the combined COHP plot, **Figure 5**, and the density of states (DOS) plot in **Figure 6**, there is a pseudo-gap near the Fermi level. This window allows the Fermi level to shift without a significant impact on the stability, which in turn is what allows the partial osmium substitution to occur. (With x=0, Fermi falls in the minimum. Os substitution increases the electron density). The Fermi shift (from the added electrons) still falls within this range, and there is another local minimum within the error of the occupancy. This is reflected by the small negative total COHP peak above the Fermi energy, as well as the highly antibonding states for the Os3-Os3 bond at the upper limit of this window.

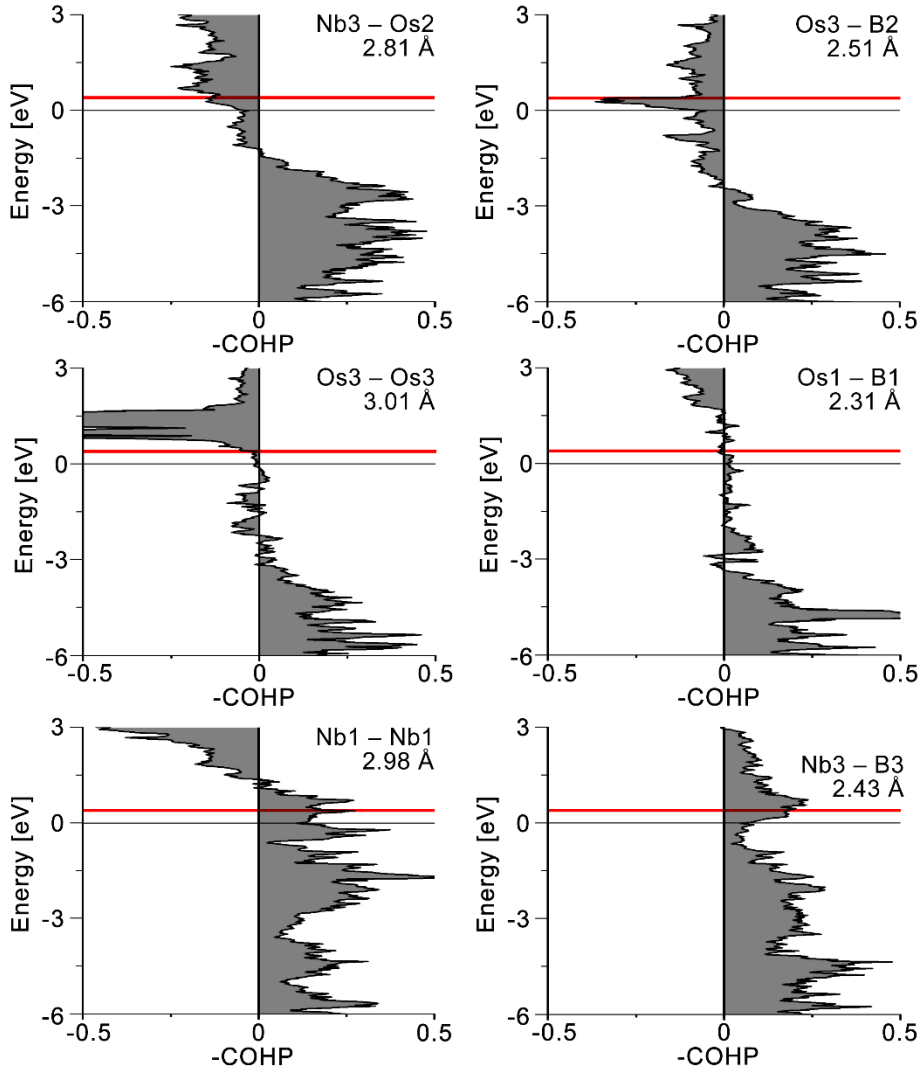

***Figure 5**: COHP plots for selected bonds. Notice that the negative of the COHP is being plotted, by convention. Negative COHP values represent bonding states for a given energy level. The Fermi energy is for the stoichiometric NbOsB, with no osmium substitution.*

All of this supports the notion that this structure could also be stable with a group 6 element on the niobium sites such as molybdenum, or even mixed sites with a more electropositive atom such as zirconium on the Nb3 site. The synthesis of such compounds is still in progress. It was recently found experimentally that LT-TaRuB crystallizes with $Ti_{1-x}Rh_{2+x-y}Ir_{3-y}B_3$ structure type while HT-TaRuB adopts the NbRuB structure type.

Because another modification of NbOsB was recently reported to crystallize with the $Ti_{1-x}Rh_{2+x-y}Ir_{3-y}B_3$ structure type, it is interesting to find out the thermodynamic stability relative to the new modification as well as the NbRuB structure type. DFT calculations were thus performed to determine the total energies of these related structure types, so that a thermodynamic comparison could be made.

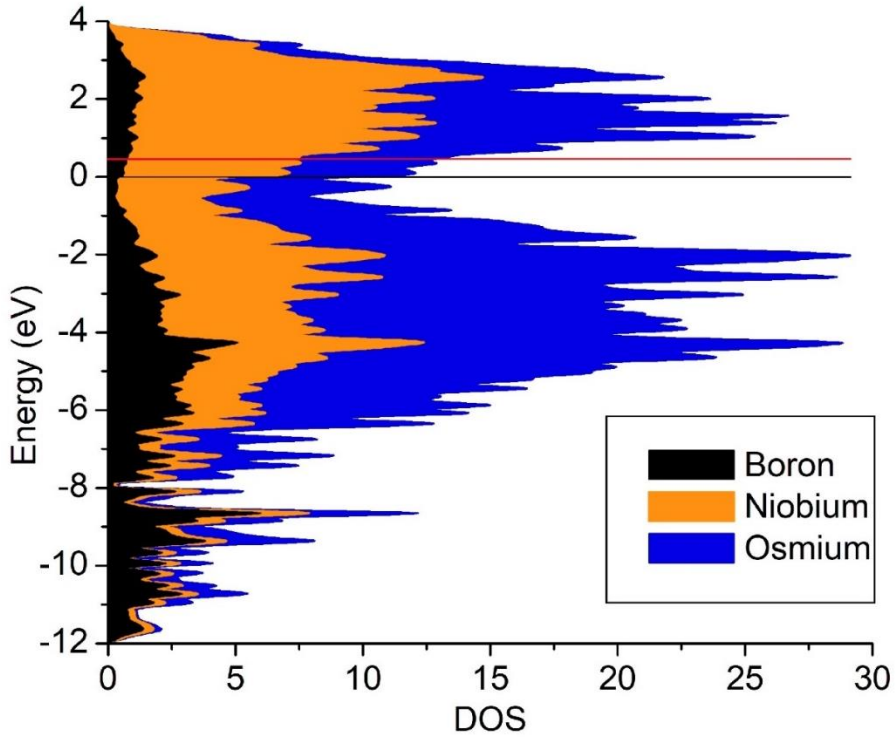

Figure 6: *Density of states for $Nb_{(1-x)}Os_{(1+x)}B$ structure and projected DOS for Nb and Os. For this calculation x=0.The fermi energy is set to zero.*

These calculations suggest that the $Ti_{1-x}Rh_{2+x+y}Ir_{3-y}B_3$ structure type is the most stable at 0 K by 3.2 kJ/mol per formula unit. However, the $Nb_{1-x}Os_{1+x}B$ is more stable than the NbRuB-type structure by 5.7 kJ/mol per formula unit.

This trend is in line with prior calculations for the Ta-Ru-B phase space [54], and suggests that the new phase is a high temperature modification of NbOsB ($Ti_{1-x}Rh_{2+x-y}Ir_{3-y}B_3$-type).

Conclusion

A new ternary boride structure has been discovered, with a unique combination of structural motifs common to other borides with higher and lower M:B ratios. Both infinite boron chains (FeB fragment) and isolated boron atoms within trigonal prisms (Re_3B-fragment) are present. Single crystal XRD confirms partial substitution of osmium onto the niobium sites, indicating that the stoichiometric structure is electron deficient. DFT and COHP analysis were performed to show unfilled bonding states in the theoretical stoichiometric NbOsB phase, which was combined with structural analysis to explain the partial substitution of osmium onto the niobium sites. It was observed that a small number of Nb-Nb and Nb-B bonds were highly stabilized at the cost of a large number of slightly unfavorable Os-Nb and Os-B interactions. This localized stabilization compensates for the highly compressed FeB fragment. It is predicted that a group 6 metal would be more appropriate for the niobium site, and that a larger metal on the osmium site may help relieve internal strain between the osmium and niobium substructures.

Experimental Section

Synthesis and Characterization: The $Nb_{(1-x)}Os_{(1+x)}B$ compound was prepared from elemental powders of niobium (>99.8%, Alfa Aesar), osmium (>99.9%, Arcos Organics), and boron (amorphous & crystalline, >99%, Alfa Aesar). The powders were ground and mixed in a 1:2:2 ratio, respectively, then pressed into pellets. The pellets were then arc-melted in a water-cooled copper crucible under argon atmosphere, using a tungsten electrode and 40 A of current. The argon was purified by passage through silica gel,

molecular sieves, and titanium sponge (950 K). The pellet was rotated in the crucible a couple of times and remelted during the arc procedure to ensure homogeneity. Weight losses during the melting process were negligible. The final product from each synthesis was a metal bead, which was then crushed to obtain powder and single crystals for further analysis.

Phase analysis was performed by X-ray powder diffraction at room temperature with a Rigaku MiniFlex 600, using a Cu Kα radiation source (λ=1.5418 Å). Rietveld refinement (full-matrix least-squares refinement) was performed using the FULLPROF program. [55] Energy-dispersive X-ray spectroscopy (EDX) was used on single crystals to verify the metal ratio (Figure S3). An attempt was made to improve the yield by starting with a 1:1:1 composition, but this led mainly to the Nb_2OsB_2 phase.

Crystal Structure Determination: The single crystals were isolated using an optical microscope and were affixed to a glass capillary for X-ray diffraction with a Rigaku XtaLAB mini. The crystallographic data are summarized in Table S4 below. The structure was solved using direct *ab-initio* methods, and refined using the SHELX programs (full-matrix least-squares based on F^2). [56,57] The metal atoms were refined using anisotropic thermal displacement parameters, and the boron atoms were refined isotropically. Semi-empirical corrections and numerical absorption corrections based on the crystal geometry were applied. [58]

Computational Methods: The Vienna Ab-initio Simulation Package (VASP) [59] was used to perform ab-initio DFT calculations for structural optimization via the projector augmented wave (PAW) method [60]. Exchange and correlations were treated with the generalized gradient approximation (GGA) functional as parameterized by Perdew, Burke, and Ernzerhof [61] with an energy cut-off of 500 eV. For structural relaxation, a convergence threshold of 0.01 eV/Å was used. The lattice parameters increased by ~1% during this relaxation, consistent with the expectations for GGA. The DOS was determined (Figure 6), and shows the fermi energy sits at a pseudogap, indicating metallic character. Interestingly, the increased VEC would shift the Fermi energy up, out of the local minimum, but it would fall in the next highest minima.

Electronic calculations were done using the linear muffin-tin orbitals approximation (LMTO) as implemented in TB-LMTO 4.7. [62] Exchange and correlation were treated with the LDA functional by Kohn and Sham. [63] A k-mesh of 6 x 24 x 6 was used, which gives 208 k-points in the irreducible Brillouin zone. No empty spheres were needed to achieve 100% filling of the unit cell. The basis sets include: 5s, 5p, 4d, and 4f for niobium; 5s, 5p, 6d, and 6f for osmium; 2s, 2p, and 3d for boron. The f orbitals for osmium and niobium and the d orbital for boron were treated by the Löwdin downfolding technique.[64]

References

12. Albert, B. & Hillebrecht, H. Boron: Elementary Challenge for Experimenters and Theoreticians. *Angew. Chemie Int. Ed.* **48**, 8640–8668 (2009).

36. Scheifers, J. P., Zhang, Y. & Fokwa, B. P. T. Boron: Enabling Exciting Metal-Rich Structures and Magnetic Properties. *Acc. Chem. Res.* **50**, 2317–2325 (2017).

37. Yeung, M. T., Mohammadi, R. & Kaner, R. B. Ultraincompressible, Superhard Materials. *Annu. Rev. Mater. Res.* **46**, 465–485 (2016).

38. Mori, T. Novel physical properties of rare earth higher borides. *J. Phys. Conf. Ser.* **176**, 012036 (2009).

39. Villars, P. & Calvert, L. D. 『*Person's Handbook of Crystallographic Data for Intermetallic Phases*』. (ASM International, 1991).

40. Kuz'ma, Yu.B.; Yarmolyuk, Y. P. The crystal structure of Ti3Co5B2. *Zhurnal Strukt. Khimii* **12**, 458 (1971).

41. Ade, M., Kotzott, D. & Hillebrecht, H. Synthesis and crystal structures of the new metal-rich ternary borides Ni12AlB8, Ni12GaB8 and Ni 10.6Ga0.4B6-examples for the first B 5 zig-zag chain fragment. *J. Solid State Chem.* **183**, 1790–1797 (2010).

42. Lundstrom, T. Structure, defects and properties of some refractory borides. *Pure Appl. Chem.* **57**, 1383–1390 (1985).

43. Chepiga, M.V.; Kuzma, Yu.B.; Kripyakevich, P. I. Crystal structure of the (Re, Co)7 B4 compound. *Dopovidi Akad. Nauk Ukr. RSR, Seriya A Fiz. ta Mat. Nauk.* 856–858 (1972).

44. Fokwa, B. P. T. & Hermus, M. All-Boron Planar B(6) Ring in the Solid-State Phase Ti(7) Rh(4) Ir(2) B(8). *Angew. Chemie Int. Ed.* **124**, 1734–1737 (2012).

45. Goerens, C. & Fokwa, B. P. T. The complex metal-rich boride Ti1+xRh2−x+yIr3−yB3 (x=0.68, y=1.06) with a new structure type containing B4 zigzag fragments: Synthesis, crystal chemistry and theoretical calculations. *J. Solid State Chem.* **192**, 113–119 (2012).

46. Zheng, Q. *et al.* Synthesis, crystal structure and properties of the new superconductors TaRuB and NbOsB. *J. Phys. Condens. Matter* **27**, 415701 (2015).

47. Rundqvist, S. *et al.* Crystal Structure Refinements of Ni3B, o-Ni4B3, and m-Ni4B3. *Acta Chemica Scandinavica* vol. 21 191–194 (1967).

48. Malik, Z., Grytsiv, A., Rogl, P., Giester, G. & Bursik, J. Phase relations and structural features in the system Ni-Zn-B. *J. Solid State Chem.* **198**, 150–161 (2013).

49. Mbarki, M., Touzani, R. St. & Fokwa, B. P. T. Experimental and Theoretical Investigations of the Ternary Boride NbRuB with a Layerlike Structure Type. *Eur. J. Inorg. Chem.* **2014**, 1381–1388 (2014).

50. Schob, O. & Parthé, E. AB compounds with Sc, Y and rare earth metals. I. Scandium and yttrium compounds with CrB and CsCl structure. *Acta Crystallogr.* **19**, 214–224 (1965).

51. Khazaei, M., Ranjbar, A., Arai, M., Sasaki, T. & Yunoki, S. Electronic properties and applications of MXenes: a theoretical review. *J. Mater. Chem. C* **5**, 2488–2503 (2017).

52. Dronskowski, R. & Bloechl, P. E. Crystal orbital Hamilton populations (COHP): energy-resolved visualization of chemical bonding in solids based on density-functional calculations. *J. Phys. Chem.* **97**, 8617–8624 (1993).

53. Fokwa, B. P. T. Borides: Solid-State Chemistry. in *Encyclopedia of Inorganic and Bioinorganic Chemistry* 1–14 (John Wiley & Sons, Ltd, 2014). doi:10.1002/9781119951438.eibc0022.pub2.

54. Mbarki, M., Touzani, R. S., Rehorn, C. W. G., Gladisch, F. C. & Fokwa, B. P. T. New ternary tantalum borides containing boron dumbbells: Experimental and theoretical studies of Ta2OsB2 and TaRuB. *J. Solid State Chem.* **242**, 28–33 (2016).

55. Rodriguez-Carvajal, J. *FULLPROF 2000: A Rietveld Refinement and Pattern Matching Analysis Program*. *Abstract of the Satellite Meeting on Powder Diffraction of the XV Congress of the IUCr, Toulouse, France* (2008).

56. Sheldrick, G. M. A short history of SHELX. *Acta Crystallogr. Sect. A Found. Crystallogr.* **64**, 112–122 (2008).

57. Sheldrick, G. M. Crystal structure refinement with SHELXL. *Acta Crystallogr. Sect. C Struct. Chem.* **71**, 3–8 (2015).

58. Sheldrick, G. M. SADABS, Program for Empirical Absorption Correction of Area Detector Data; Göttingen, Germany, 1996. (1996).

59. Kresse, G. & Joubert, D. From ultrasoft pseudopotentials to the projector augmented-wave method. *Phys. Rev. B* **59**, 1758–1775 (1999).

60. Blöchl, P. E. Projector augmented-wave method. *Phys. Rev. B* **50**, 17953–17979 (1994).

61. Perdew, J. P., Burke, K. & Ernzerhof, M. Generalized Gradient Approximation Made Simple. *Phys. Rev. Lett.* **77**, 3865–3868 (1996).

62. Tank, R. W. & Jepsen, O. The STUTTGART TB-LMTO-ASA program. *Cell* 1–27 (1998).

63. Kohn, W. & Sham, L. J. Self-consistent equations including exchange and correlation effects. *Phys. Rev.* **140**, 1133–1138 (1965).

64. Lowdin, P.-O. A Note on the Quantum-Mechanical Perturbation Theory. *J. Chem. Phys.* **19**, 1396–1171 (1951).

Chapter 3: 1D iron chains in the complex metal-rich boride $Ti_{5-x}Fe_{1-y}Os_{6+x+y}B_6$ (x = 0.66, y = 0.27) representing an unprecedented structure type based on unit cell twinning

*Jan P. Scheifers, Michael Küpers, Rashid Touzani, N.G. Bakshi, Fabian C. Gladisch, Rainer Poettgen, Boniface P. T. Fokwa**

Abstract:

An new metal-rich boride, $Ti_{4.34(1)}Fe_{0.73(1)}Os_{6.93(2)}B_6$, crystallizing in a new structure type (space group *Cmcm*, no. 63) is prepared by arc-melting. The complex boride contains both isolated boron-atoms and infinite zigzag Boron chains (B−B distance of 1,74 Å), which by itself is rare among metal-rich borides. In addition, the structure also contains isolated 1D iron chains running parallel to the B-chains. This combination of structural features is already unique, but the most striking aspects of this new structure type are that the isolated Fe-chains are offset from each other and that the distances between then are different in different crystallographic directions. The unique structure with its fascination features is described for the first time based on the single crystal solution, compared to other boride structures and derived from the recently published $Nb_{1-x}Os_{1-x}B$ (*Pnma*). The chemical bonding is analyzed with regard the 1D Fe-chains and the resulting magnetic properties using DFT calculations. These calculations predict strongly preferred ferromagnetic ordering within each chain, but only small energy differences for different magnetic interactions between these chains. This intermetallic compound offers the opportunity to study new configurations and interactions of magnetically active elements in metal borides.

Introduction

Metal borides come in a huge variety of crystal structures, as there are more than 150 different structure types reported for binary and ternary borides. Their interesting physical properties draw attention to them like their mechanical hardness (ReB_2) [65], magnetism ($Nd_2Fe_{14}B$) [15] or superconductivity (MgB_2) [23]. In their search for new and exotic magnetic phenomena in the solid state, researchers became interested in the field of low dimensional magnetism. Materials with low dimensional substructures of magnetic elements are therefore attracting a lot of research interest. Multiple of these materials have been discovered among the group of metal borides. For example, one dimensional chains of magnetically active elements (M) in $A_2MT_{5-x}T'_xB_2$ (A = Sc, Ti, Zr, Hf; T/T' = Ru, Rh, Ir) [27,66–68] are present in the $Ti_3Co_5B_2$-structure type or in $Nb_6Fe_{1-x}Ir_{6+x}B_8$ [26]. Furthermore, ladders and scaffolds of magnetically active elements can be found in $Zn_{11}Rh_{18}B_8$-types compounds with the compositions $Ti_{9-x}M_{2+x}Ru_{18}B_8$ (M=Fe, Mn) [69]. Just recently, spin frustration and magnetically ordering was discovered in $TiCrI_2B_2$, containing one-dimensional stacks of Cr_3 triangles [70]. However, the distances between neighboring chains within each structure are the same in most of those compounds since they usually adopt tetragonal or hexagonal structures with the magnetic chains running along the *c*-direction. Moreover, these chains are not offset from each other along their direction due to the layered structures of most metal-rich borides.

Metal borides can structurally be classified according to the metal-to-boron ratio (M:B) [16]. While metal borides with high metal content (large M:B) show only isolated

boron-atoms, with decreasing M:B-ratio, boron fragment as well as one-, two- and three-dimensional boron-networks can be found. Borides with a M:B- ratio of 2:1 are just at the edge between borides with isolated boron atoms and borides with extended B-networks. As such, they often contain covalently bonded Bn-substructures that resemble fragments of the planar B-honeycomb layers found in AlB_2 along with isolated B-atoms. These boron fragments, like B_2-dumbbells, zigzag fragments, trigonal planar B_4-units, B_6-rings and infinite B-chains are known [71].

Herein we report the synthesis and crystal structure of the novel boride $Ti_{4.34(1)}Fe_{0.73(1)}Os_{6.93(2)}B_6$, that contains infinite B-chains, isolated B-atoms as well as 1D Fe-chains in a layered structure. The distances between the parallel chains are not all the same due to the orthorhombic crystal structure and the presences of zigzag B-chains

Experimental section:

Synthesis and Characterization: $Ti_{4.34(1)}Fe_{0.73(1)}Os_{6.93(2)}B_6$ was synthesized by arc-melting the elements in a water-cooled copper crucible under an Ar atmosphere using a tungsten electrode. Two separate batches of starting materials Ti (Arcos Organics, 99.7%), Os (Chempur, 99.99%), Fe (Umicore AG & Co. KG, 99.99%) and B (Chempur, 99.9%) were weighted in the atomic ratios 2 Ti : 1 Fe: 2 Os : 2 B and 2 Ti : 1 Fe : 3 Os : 3B. Each mixture was pressed into a pellet and arc-melted under argon; the Ar has been purified before over silica gel, molecular sieves and Ti sponge (950 K). The first batch was briefly melted and only once, while the second batch was melted multiple times for several seconds each to ensure good homogeneity of the samples. Weight losses during the

melting process were negligible. Small beads of a gray product with metallic luster were obtained. The second batch had several small silvery crystals on the surface.

Both batches were crushed, and the fragments were checked for single crystals using a stereo microscope. The second batch contained several needle-shaped single crystals suitable for X-ray structure analysis (details below).The rest of the samples were ground into fine powder and powder X-ray diffraction patterns were collected using a Rigaku MiniFlex 600benchtop diffractometer (reflection geometry) using graphite monochromatized Cu-$K_{\alpha 1}$ (λ = 1.541 Å) radiation and a scintillation counter (SC-70) detector. A Rietveld refinement was performed using the FullProf suite 2017 [55,72,73] and the results were plotted with WinPLOTR. [74] Single crystals were measured on a STOE IPDS II diffractometer with graphite-monochromised Mo-Kα radiation (λ = 0.71073 Å). A numerical absorption correction was performed for the 4573 measured reflections. The structure was solved using direct methods (SHELXS97 implemented in WinGX [56,75,76]) and refined using the SHELXL programs. All metal sides were refined with anisotropic displacement parameters, while the boron sites were refined isotropically. The chemical composition was checked by EDX.

Computational methods:

The ab-initio total energy and molecular dynamics program "Vienna *Ab-initio* Simulation Package" (VASP) [77,78] was used for structural optimization with the projector-augmented wave (PAW) method [59]. Exchange and correlation in this density functional theory (DFT)-based method were treated with the generalized gradient approximation

(GGA) functional as parameterized by Perdew, Burke and Ernzerhof (GGA-PBE) [61] using an energy cut-off of 500 eV for the plane waves. As starting lattice parameters and Wyckoff positions for the calculations we used the experimentally obtained structure parameters. Cell shape and volume variation were allowed during the structural optimization until a total energy self-consistency of 10^{-6} eV and until the self-consistency for the ionic relaxation of 0.01 eV/A.

As mixed occupancies are found experimentally for Fe, Os and Ti, we choose to simplify the model used in our calculations by assuming 100% Fe on the M3-site and 100% Os on the sites M1 and M2. This will not cause any major differences as the VE count and the character of the orbitals involved does not change. Furthermore, we assume the sites Ti and T2 to be fully occupied by Ti. This, in contrast, will slightly affect the electronic structure because of the small change in the VE count from 96.6 VE to 94 VE. This small difference however, can easily be taken into account using the rigid-band model (RBM), which will cause a small shift between the Fermi-levels of the experimentally obtained structure and the calculated model due to the small, but known difference in the VE count.

The magnetic ground-state was calculated by performing electronic structure calculations with initial magnetic moments on the Fe-site in the optimized structure while allowing spin-polarization and comparing the resulting total energies of the different spin arrangements (see below). In order to generate spin arrangements with antiferromagnetic interactions along the a-axis a 2x1x1 supercell is used. The k-point mesh was chosen to

be 9x3x3. We have used the algorithm by Monkhorst and Pack [79] to generate the k-point mesh.

Chemical bonding analyses were carried out using the tight-binding, linear muffin-tin orbitals with the atomic spheres approximation (TB-LMTO-ASA) [62] as implemented in the TB-LMTO 4.7 program. The bonding analysis was done by calculation of the density-of-states (DOS), the crystal orbital Hamilton population (COHP) [52] and its integrals (ICOHP). The ICOHP can be seen as a semi-quantitative bonding energy which measures covalent contributions in solids. Because –COHP values are plotted, negative –COHPs are antibonding states, positive ones are bonding states and non-bonding states have –COHPs of zero. The Fermi level (E_F) of the simplified model was set to 0 eV.

Results

X-ray powder diffraction: The sample with the composition 2 Ti : 1 Fe: 2 Os : 2 B contained mainly $TiFe_{1-x}Os_{2+x}B_2$ (see **chapter 5**) and elemental Os, but also additional reflections that could be indexed using the unit cell found by single crystal diffraction. The Rietveld refinement confirms that about 10 wt.-% of the sample corresponds to $Ti_{5-x}Fe_{1-y}Os_{6+x+y}B_6$.

The other sample with the composition 2 Ti : 1 Fe : 3 Os : 3B did not show reflections of this compound even though single crystals of $Ti_{5-x}Fe_{1-y}Os_{6+x+y}B_6$ could be isolated from the fragments.

Single crystal diffraction of $Ti_{5-x}Fe_{1-y}Os_{6+x+y}B_6$

The crystal structure was determined by single crystal X-Ray diffraction methods. The diffraction pattern containing 838 unique reflections can be indexed using an orthorhombic unit cell in the space group no. 63 (*Cmcm*) with the lattice parameters a = 2.982(1) Å, b = 13.057(6) Å and c = 21.17(1) Å (see **Table 2**).

Solving the crystal structure results in 7 different metal sites and three boron sites appear in the electron density map after a few refinement cycles (see **Table 3**). Mixed occupancies are found on three out seven metal sites: T1: 83.6(9) % Ti and 16.4(9) % Os, T2: 82.6(8) % Ti and 17.4(8) % Os, M1: 73(1) % Fe, 27(1) % Os. This results in the final composition $Ti_{4.34(1)}Fe_{0.73(1)}Os_{6.93(2)}B_6$ or x = 0.66(1) and y = 0.21(1) for $Ti_{5-x}Fe_{1-y}Os_{6+x+y}B_6$. The presence of the metals is confirmed by EDX on a single crystal.

The final R-values for the refinement of the single crystal structure are R_1 = 0.0428 and wR_2 = 0.0775. The unit cell contains two identical layers of atoms shifted by ½ *b* + ½ *c* and stacked along the *a*-axis. The structure can be understood as being built up by two different building units: MT_2B and $TiOs_4M_6B_4$. Both building units (see **Figure 7**) are already known in other complex metal borides.

***Table 2**: Results of the single crystal refinement of the new $Ti_{4.34(1)}Fe_{0.73(1)}Os_{6.93(2)}B_6$.*

Chemical formula	$Ti_{4.34(1)}Fe_{0.73(1)}Os_{6.93(2)}B_6$
Formula weight [g/mol]	1634.07
Crystal system, space group	orthorhombic, *Cmcm*, no. 63
Lattice parameters	a = 2.982(1) Å b = 13.057(6) Å c = 21.17(1) Å α = β = γ = 90°
Volume [Å^3], Z	824.2(7), 4
Density [Mg/m^3]	13.169
Absorption coefficient [mm^{-1}]	111.703
F(000)	2688
Crystal size [mm^3]	0.189 x 0.161 x 0.021
Θ range [°]	1.924 to 30.940
Index ranges	$-4 \leq h \leq 4$, $-17 \leq k \leq 17$, $-30 \leq l \leq 30$
Reflections (collected / independent / R(int))	4581 / 738 / 0.1355
data/restraints/parameters	738 / 0 / 50
Goodness-of-fit on F2	1.073
Final R indices (I>2sigma(I))	R1 = 0.0428, wR2 = 0.0775
R indices (all data)	R1 = 0.0729, wR2 = 0.0936
Extinction coefficient	0.00030(4)
Largest diff. Peak / hole [e$^-$/Å^3]	5.178 / -5.432

***Table 3**: Wyckoff sites, fractional coordinates, occupancies and equivalent displacement parameters for all atoms in $Ti_{4.34(1)}Fe_{0.73(1)}Os_{6.93(2)}B_6$ as obtained from single-crystal X-ray diffraction.*

site	Wyckoff site	*x*	*y*	*z*	Occupancy [%]	U_{eq} [Å²]
B1	*8f*	½	0.297(3)	0.334(1)	100	0.006(3)
B2	*8f*	½	0.220(3)	0. 490(1)	100	0.006(3)
B3	*8f*	½	0.539(3)	0.370(1)	100	0.006(3)
Os1	*8f*	0	0.4126(1)	0.3492(1)	100	0.007(1)
Os2	*8f*	0	0.5591(1)	0.4434(1)	100	0.006(1)
Os3	*8f*	0	0.6218(1)	0.3152(1)	100	0.006(1)
T1	*8f*	½	0.2216(3)	0.4069(2)	84(1) Ti / 16(1) Os	0.011(1)
T2	*8f*	½	0.3842(3)	0.4560(2)	83(1) Ti / 17(1) Os	0.016(1)
Ti	*4c*	½	0.4677(6)	¼	100	0.005(1)
M	*4c*	0	0.2665(3)	¼	73(1) Fe / 27(1) Os	0.003(1)

The core of the MT_2B-unit is a boron zigzag-chain (B2), which is coordinated within trigonal prisms of T1 and T2. These prisms are face-sharing two of the rectangular faces with each other, so the B-atom inside form the infinite zigzag chains along the *a*-axis. The third rectangular face of the trigonal prisms is capped by the M2 position. The B-B-distance within the chain is 1.78(2) Å, with a B-B-B angle of 114,326(1) °. This building unit can be found in all complex metal borides containing infinite boron-zigzag-chains. The simplest structure containing B-zigzag chains is the β-FeB-type structure adopted by TiB [80]. Here, the trigonal Ti-prisms around the Boron atoms are capped by Ti-atoms of adjacent Ti_6B prism. The B-B distance in TiB is 1.82 Å with a B-B-B angle of 113.4 °. The shorter B-B distance in $Ti_{5-x}Fe_{1-y}Os_{6+x+y}B_6$ is most likely a consequence of the sites T1 and T2 being partially occupied by the smaller Os.

Another boride with both zigzag B-chains and isolated B-atoms is $Al_3Ru_9B_8$ [81]. In this hexagonal structure, the B-chains run along the *c*-direction. The B-B distance is slightly shorter (1.747(6) Å) and the B-B-B angle is slightly smaller (113.0 (6) °). However, in this compound the trigonal prisms coordinating the B-chain are formed by the smaller, late-transition metal Ru instead of Ti.

Recently, we discovered $Nb_{1-x}Os_{1+x}B$, another ternary Os-boride, that contains both zigzag B-chains and isolated B-atoms [82]. Despite the larger B-B-B angle of 116 °, the environment of the B-chains in $Nb_{1-x}Os_{1+x}B$ is very similar to the MT_2B-units. The B-B distance in $Nb_{1-x}Os_{1+x}B$ is 1.77(5) Å and each of the two metal-sites coordinating the B-chains show mixed occupancies of the early transition metal with Os. Even the small differences in the occupancies between the T1 and T2 are reflected in $Nb_{1-x}Os_{1+x}B$, where one Nb-site (Nb2) contains 80.4% Nb and the other site (Nb3) contains 90.5% Nb, compared to 86.8(5)% Ti and 90.1(5)% Ti on T1 and T2, respectively.

The second building block in $Ti_{5-x}Fe_{1-y}Os_{6+x+y}B_6$ is $TiOs_4M_6B_4$. The core of this building unit is a Ti-Atom with a complex coordination geometry. The Ti-Atom is centered in a distorted pentagonal prism of four Os-, four M1- and two M3-sites with four of the five rectangular faces being capped by isolated Boron atoms. On the fifth rectangular face, the pentagonal prism is capped by a M3-position of the next $TiOs_4M_6B_4$-building unit.

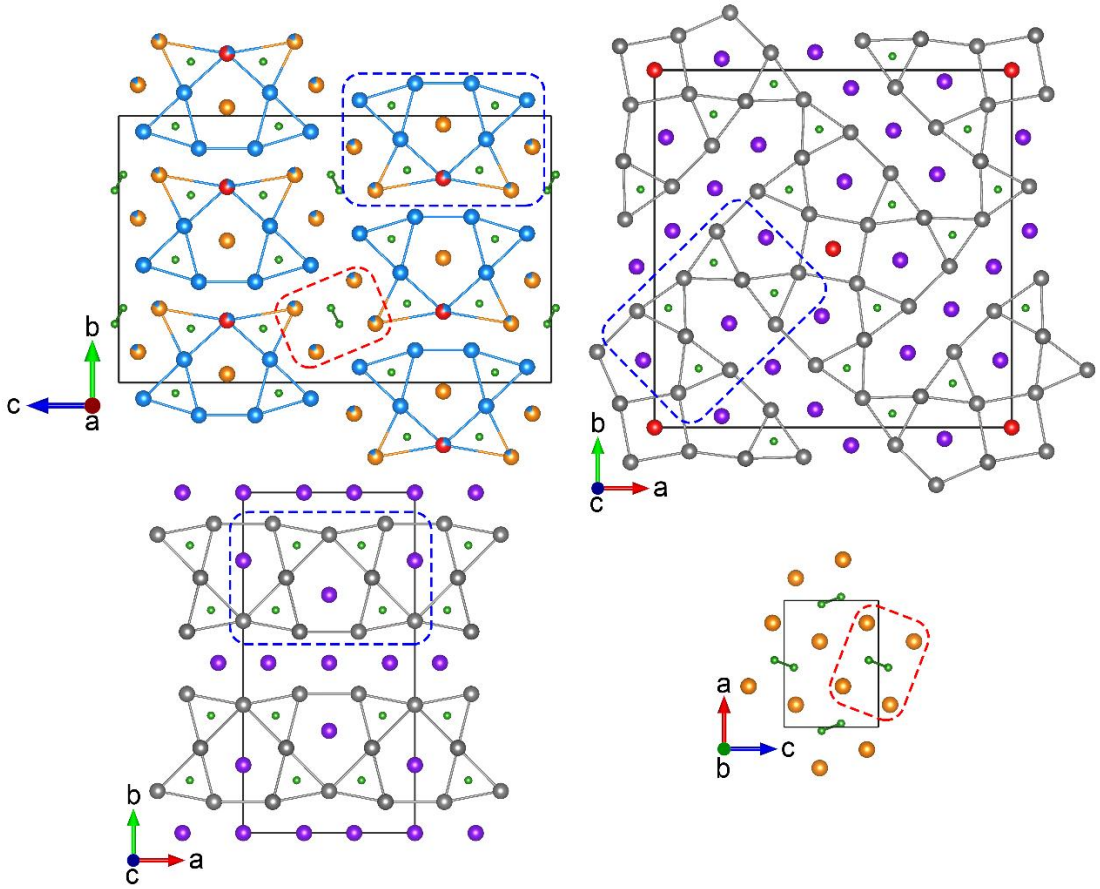

***Figure 7**: $Ti_{5-x}Fe_{1-y}Os_{6+x+y}B_6$ (top left) with highlighted $TiOs_4M_6B_4$ (blue dashed line) and MT_2B (red dashed line) building blocks compared with $Zn_9Fe_2Rh_{18}B_8$ (top right), $Zn_5Rh_8B_4$ (bottom left) and TiB (bottom right). Ti-atoms orange, Os blue, B green, Fe red, Zn in purple and Rh in gray.*

Similar face capped pentagonal prisms, stacked on top of each other along one axis can also be found in other complex metal borides (see **Figure 7**), like for example in the $Zn_5Rh_8B_4$- [83], the $Ti_3Co_5B_2$- [40]or the $Zn_{11}Rh_{18}B_8$-structure-type [84].

Exciting from a physics point of view is the existence of the M3-sides in this unit with ca. 75 % Fe content resulting in one-dimensional Fe-chains along the *a*-axis, which makes $Ti_{5-x}Fe_{1-y}Os_{6+x+y}B_6$ a potential candidate for low dimensional magnetic ordering. Metal borides, especially those showing low-dimensional arrangements of magnetically

active *3d* elements can show extraordinary magnetic properties, as it was found for example in $A_2MT_{5-x}T'_xB_2$ (A = Sc, Ti, Zr or Hf; T/T' = Ru, Rh or Ir) [27,66,67,85,86] in the $Ti_3Co_5B_2$-structure type. In contrast to these compounds, in which the magnetic atoms are coordinated by tetragonal prisms formed exclusively by other metal atoms, the M3 site in $Ti_{5-x}Fe_{1-y}Os_{6+x+y}B_6$ is directly coordinated by two isolated B-atoms (B1). The Fe-B distance is 2.35(3) Å indicating strong interactions between these two atoms. From other structures such as $TiFe_{1-x}Os_{2+x}B_2$ or $Nb_6Fe_{1-x}Ir_{6+x}B_8$ [26] it is known that magnetic interactions along the Fe-chains are strengthened by coordinating B-atoms, making $Ti_{5-x}Fe_{1-y}Os_{6+x+y}B_6$ and its magnetic properties even more exciting since an enhanced ordering temperature can be expected.

The most interesting feature is that the Fe-chains are offset by ½ *a*, which makes this structure unique among the borides with 1D Fe-chains. The distance between the Fe-chains is 6.526(7) Å in *b*-direction but 10.594 (5) Å in *c*-direction. In other borides with 1D Fe-chains the chains are usually equidistant from each other as those borides crystallize in tetragonal or hexagonal structures with the Fe-chains running along the *c*-direction. The actual distances between Fe-atoms of different chains however are slightly larger (6.697(3) Å and 10.698(5) Å, respectively) as the chains are offset from each other. This unique arrangement of well separated Fe-chains could lead to unexpected magnetic behavior. Unfortunately, we have not been able to synthesize suitable samples for magnetic property measurements yet as all of them contain other magnetic compounds such as $TiFe_{1-x}Os_{2+x}B_2$.

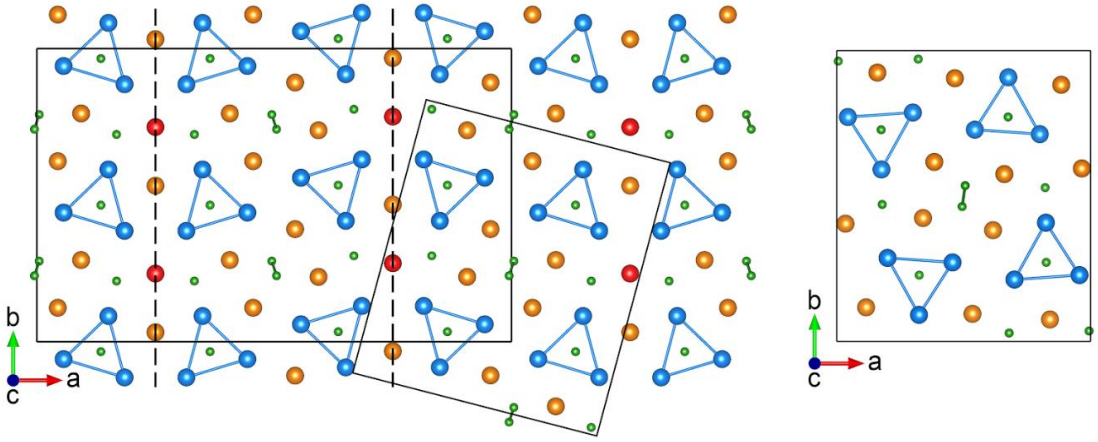

***Figure 8**: $Ti_{5-x}Fe_{1-y}Os_{6+x+y}B_6$ (non-standard setting) with indicated twin boundaries (left) and $Nb_{1-x}Os_{1+x}B$ (right).*

If we focus on the Osmium atoms instead of Titanium, we find that the Os-rich sites together form boron-centered (B3) trigonal prisms that are stacked along the a-direction with all three rectangular faces being capped by Ti. The zigzag B-chains are located in between the capped Os-prisms. This is strikingly similar to the previously mentioned $Nb_{1-x}Os_{1+x}B$ (see **Figure 8** and **chapter 2**). In fact, both the Os-prisms as well as the zigzag B-chains are basically identical in the two structures. There are, however, two main differences: the previously discussed Fe-chains (M3 site) of $Ti_{5-x}Fe_{1-y}Os_{6+x+y}B_6$ do not have an equivalent in $Nb_{1-x}Os_{1+x}B$; the other difference is the Ti forming the center of the $TiOs_4M_6B_4$-unit. It is capping two of the Os-prisms simultaneously, which is not observed in $Nb_{1-x}Os_{1+x}B$. The M3 site as well as the Ti-site have a lower multiplicity than the other sites in the crystal structure, because they are located on a mirror plane at z = ¼ and z = ¾. The structure in between is identical with the $Nb_{1-x}Os_{1+x}B$-type structure. Therefore, $Ti_{5-x}Fe_{1-y}Os_{6+x+y}B_6$ is a twinned variant of the $Nb_{1-x}Os_{1+x}B$-type structure. The

unit cell twinning doubles the unit cell and thus doubles the number of zigzag B-chains per unit cell compared to the $Nb_{1-x}Os_{1+x}B$-type structure. Moreover, it splits one out of the three Nb-sites in the $Nb_{1-x}Os_{1+x}B$-type structure into the two crystallographic different Ti- and M3-site of $Ti_{5-x}Fe_{1-y}Os_{6+x+y}B_6$.

DFT calculations:

The non-spin polarized density of states (DOS) of $Ti_{5-x}Fe_{1-y}Os_{6+x+y}B_6$ has been calculated and it shows that $Ti_{5-x}Fe_{1-y}Os_{6+x+y}B_6$ is - as expected - metallic since a non-zero DOS at the Fermi-level (E_F) is predicted. In fact, not a gap but a peak is observed at the Fermi-level (see **Figure 9**), which is commonly taken as signal for an electronic instability. A look at the partial DOS reveals that Fe mainly contributes to the peak at E_F, so the electronic instability can potentially be resolved by spin-polarization.

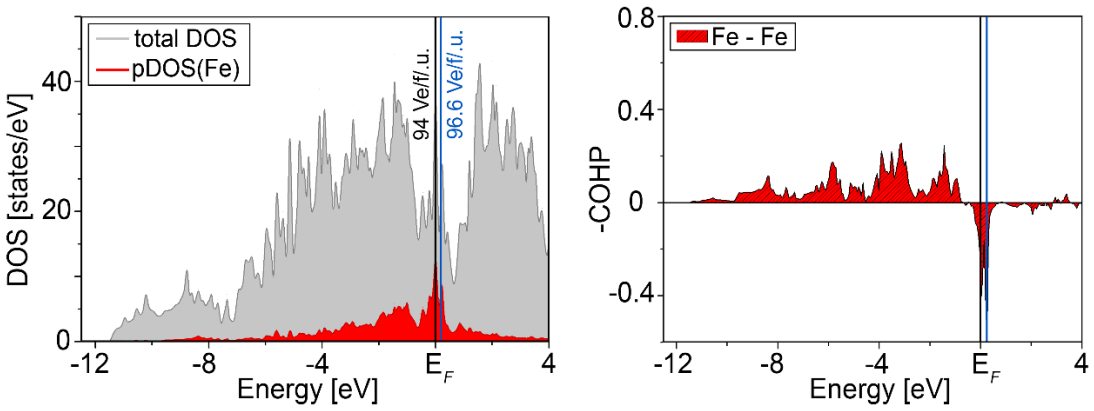

***Figure 9**: non-spin polarized DOS (left) of $Ti_{5-x}Fe_{1-y}Os_{6+x+y}B_6$ and COHP of the Fe-Fe bond (right) along the a-axis.*

Thus, we carried out spin-polarized electronic structure types using different models for the spin ordering. With allowed spin-polarization the peak caused by the states of Fe disappears (see **Figure 10**). All spin arrangements calculated (see **Figure 11**) are at least 130 meV lower in energy than the non-spin polarized case. Therefore, spin polarization would most likely cause magnetic ordering in $Ti_{5-x}Fe_{1-y}Os_{6+x+y}B_6$, if the temperature is low enough.

Since $Ti_{5-x}Fe_{1-y}Os_{6+x+y}B_6$ is related to $Nb_{1-x}Os_{1+x}B$ by unit cell twinning, we focused our attention on the bonds around the twin boundary for the COHP analysis. The bonding situation in $Nb_{1-x}Os_{1+x}B$ has been analyzed in detail elsewhere [82]. The COHP plots show strongly antibonding Fe-Fe interactions, which seem to be the origin of the electronic instability.

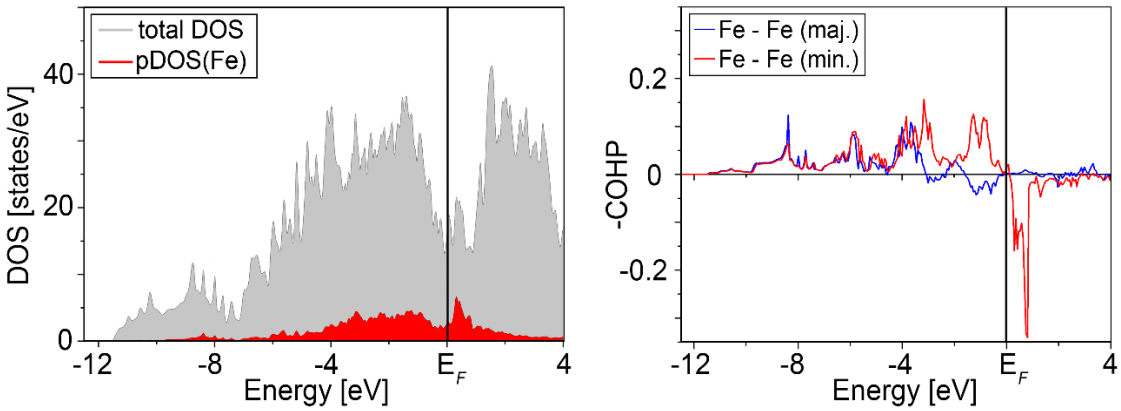

***Figure 10**: spin-polarized DOS (left) and partial DOS of Fe (right) in $Ti_{5-x}Fe_{1-y}Os_{6+x+y}B_6$.*

The magnetic ground-state is predicted an antiferromagnetic ordering (AFM-1, see **Figure 11**) with ferromagnetic interactions with each M3-chain as well as between M3-chains on the same mirror plane. The coupling between M3-chains on different mirror planes (z=0.25 and z=0.75) is weak due to the long distance of 10.7 Å and antiferromagnetic. Antiferromagnetic interactions within each M3-chain are strongly unfavorable as the total energy is at least 160 meV higher than for ferromagnetic interactions within each M3-chain.

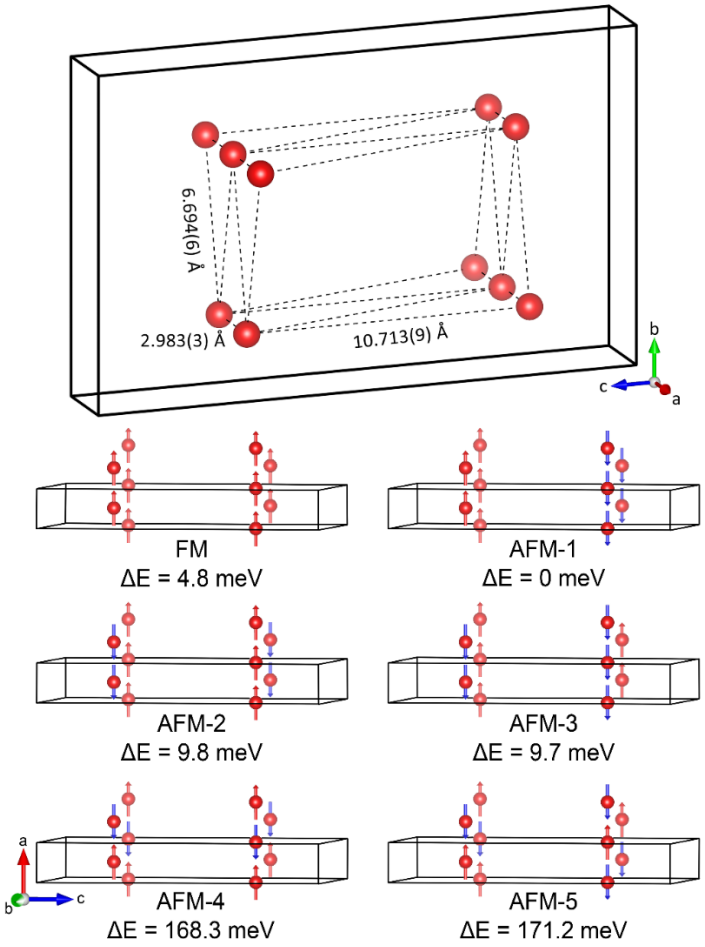

Figure 11: *Fe-Fe distances in $Ti_{5-x}Fe_{1-y}Os_{6+x+y}B_6$ after relaxation (top) and the six magnetic structures used in the calculations including their energy difference (bottom).*

Conclusion

We have synthesized a new complex metal boride $Ti_{5-x}Fe_{1-y}Os_{6+x+y}B_6$ (x = 0.46, y = 0.28) that contains both zigzag boron chains and 1-dimensional Fe-chains. The structure is a twinned quaternary variant of the recently published $Nb_{1-x}Os_{1+x}B$. For the first time, we find chains of magnetically active *3d* elements that are offset and well separated from each other. The short intra-chain Fe-Fe distance and the coordination by isolated boron atoms hint at the possibility of magnetic ordering in this new compound. Our DFT calculations indicate an electronic instability due to Fe-Fe interactions along the chains, which can be resolved by spin-polarization. We predict an antiferromagnetic ground-state with ferromagnetic coupling of spins with each Fe-chain.

The new crystal structure is a perfect example of the structural similarities in a lot of complex metal borides. Well-known structural motifs are combined forming a new complex metal boride crystal structure. This shows the great potential of complex metal borides for designing new crystals structures being built up out of known building units for specific physical properties such as low dimensional magnetism.

Acknowledgments

The authors would like to acknowledge the financial support by UC Riverside (Dissertation Year Award to J. P. S.) and the NSF (CARRER award to B P.T. F, DMR-1654780).

References

15. Givord, D., Li, H. S. & Moreau, J. M. Magnetic properties and crystal structure of Nd2Fe14B. *Solid State Commun.* **50**, 497–499 (1984).

16. Rogl, P. Competition Between Trigonal Prisms and other Coordination Polyhedra in Borides, Carbides, Silicides and Phosphides. in *Modern Perspectives in Inorganic Crystal Chemistry* 267–278 (Springer Netherlands, 1992). doi:10.1007/978-94-011-2726-4_13.

23. Nagamatsu, J., Nakagawa, N., Muranaka, T., Zenitani, Y. & Akimitsu, J. Superconductivity at 39 K in magnesium diboride. *Nature* **410**, 63–64 (2001).

26. Mbarki, M., St. Touzani, R. & Fokwa, B. P. T. Unexpected Synergy between Magnetic Iron Chains and Stacked B_6 Rings in $Nb_6Fe_{1-x}Ir_{6+x}B_8$. *Angew. Chemie Int. Ed.* **53**, 13174–13177 (2014).

27. Fokwa, B. P. T., Lueken, H. & Dronskowski, R. Rational Design of Complex Borides - One-Electron-Step Evolution from Soft to Semi-Hard Itinerant Ferromagnets in the New Boride Series Ti2FeRu5-nRhnB2 ($1 \leq n \leq 5$). *Eur. J. Inorg. Chem.* **2011**, 3926–3930 (2011).

55. Rodriguez-Carvajal, J. *FULLPROF 2000: A Rietveld Refinement and Pattern Matching Analysis Program*. *Abstract of the Satellite Meeting on Powder Diffraction of the XV Congress of the IUCr, Toulouse, France* (2008).

56. Sheldrick, G. M. A short history of SHELX. *Acta Crystallogr. Sect. A Found. Crystallogr.* **64**, 112–122 (2008).

59. Kresse, G. & Joubert, D. From ultrasoft pseudopotentials to the projector augmented-wave method. *Phys. Rev. B* **59**, 1758–1775 (1999).

61. Perdew, J. P., Burke, K. & Ernzerhof, M. Generalized Gradient Approximation Made Simple. *Phys. Rev. Lett.* **77**, 3865–3868 (1996).

62. Tank, R. W. & Jepsen, O. The STUTTGART TB-LMTO-ASA program. *Cell* 1–27 (1998).

65. Chung, H. Y. *et al.* Synthesis of ultra-incompressible superhard rhenium diboride at ambient pressure. *Science (80-.).* **316**, 436–439 (2007).

66. Fokwa, B. P. T., Lueken, H. & Dronskowski, R. Rational synthetic tuning between itinerant antiferromagnetism and ferromagnetism in the complex boride series Sc2FeRu 5-nRhnB2($0 \leq n \leq 5$). *Chem. - A Eur. J.* **13**, 6040–6046 (2007).

67. Hermus, M., Yang, M., Grüner, D., DiSalvo, F. J. & Fokwa, B. P. T. Drastic Change of Magnetic Interactions and Hysteresis through Site-Preferential Ru/Ir Substitution in $Sc_2FeRu_{5-x}Ir_xB_2$. *Chem. Mater.* **26**, 1967–1974 (2014).

68. Shankhari, P., Zhang, Y., Stekovic, D., Itkis, M. E. & Fokwa, B. P. T. Unexpected Competition between Antiferromagnetic and Ferromagnetic States in Hf2MnRu5B2: Predicted and Realized. *Inorg. Chem.* **56**, 12674–12677 (2017).

69. Fokwa, B. P. T., Samolyuk, G. D., Miller, G. J. & Dronskowski, R. Ladders of a Magnetically Active Element in the Structure of the Novel Complex Boride $Ti_9Fe_2Ru_{18}B_8$: Synthesis, Structure, Bonding, and Magnetism. *Inorg. Chem.* **47**, 2113–2120 (2008).

70. Küpers, M., Lutz-Kappelman, L., Zhang, Y., Miller, G. J. & Fokwa, B. P. T. Spin Frustration and Magnetic Ordering from One-Dimensional Stacking of Cr_3 Triangles in $TiCrIr_2B_2$. *Inorg. Chem.* **55**, 5640–5648 (2016).

71. Scheifers, J. P., Zhang, Y. & Fokwa, B. P. T. Boron: Enabling Exciting Metal-Rich Structures and Magnetic Properties. *Acc. Chem. Res.* **50**, 2317–2325 (2017).

72. Rodriguez-Carvajal, J. FullProf: A Program for Rietveld Refinement and Profile Matching Analysis of Complex Powder Diffraction Patterns. in *Satellite Meeting on Powder Diffraction of the XV Congress of the IUCr* 127 (1990).

73. Rodríguez-Carvajal, J. Recent advances in magnetic structure determination by neutron powder diffraction. *Phys. B Condens. Matter* **192**, 55–69 (1993).

74. Roisnel, T. & Rodriguez-Carvajal, J. WinPLOTR: a Windows tool for powder diffraction patterns analysis. in *Materials Science Forum, Proceedings of the Seventh European Powder Diffraction Conference (EPDIC 7)* (eds. Delhez, R. & Mittenmeijer, E. J.) 118–123 (2000).

75. Farrugia, L. J. WinGX suite for small-molecule single-crystal crystallography. *J. Appl. Crystallogr.* **32**, 837–838 (1999).

76. Farrugia, L. J. WinGX and ORTEP for Windows : an update. *J. Appl. Crystallogr.* **45**, 849–854 (2012).

77. Kresse, G. Vienna ab initio simulation package. (1999).

78. Kresse, G. & Hafner, J. Ab initio molecular dynamics for liquid metals. *Phys. Rev. B* **47**, 558–561 (1993).

79. Monkhorst, H. J. & Pack, J. D. Special points for Brillouin-zone integrations. *Phys. Rev. B* **13**, 5188–5192 (1976).

80. Decker, B. F. & Kasper, J. S. The crystal structure of TiB. *Acta Crystallogr.* **7**, 77–80 (1954).

81. Hirt, S., Hilfinger, F. & Hillebrecht, H. Synthesis and crystal structures of the new ternary borides Fe3Al2B2 and Ru9Al3B8 and the confirmation of Ru4Al3B2 and Ru9Al5B8-x ($x \approx 2$). *Zeitschrift fur Krist. - Cryst. Mater.* **233**, 295–307 (2018).

82. Forsythe, R., Scheifers, J. P., Zhang, Y. & Fokwa, B. P. T. HT-NbOsB: Experimental and Theoretical Investigations of a Boride Structure Type Containing Boron Chains and Isolated Boron Atoms. *Eur. J. Inorg. Chem.* **2018**, (2018).

83. Hartung, H., Schiffer, J., Nagelschmitz, E. A. & Jung, W. Synthese und Kristallstrukturen des Zink-Rhodiumborids Zn5Rh8B4 und der Lithium-Magnesium-Rhodiumboride LixMg5−xRh8B4 (x = 1.1 und 0.5) und Li8Mg4Rh19B12. *Zeitschrift für Anorg. und Allg. Chemie* **633**, 1645–1650 (2007).

84. Eibenstein, U. & Jung, W. Zn11Rh18B8 and Zn10MRh18B8 with M = Sc, Ti, V, Cr, Mn, Fe, Co, Ni, Cu, Al, Si, Ge, Sn - New Ternary and Quaternary Zinc Rhodium Borides. *Zeitschrift für Anorg. und Allg. Chemie* **624**, 802–806 (1998).

85. Houben, A. *et al.* Synthesis, crystal structure, and magnetic properties of the semihard itinerant ferromagnet RhFe3N. *Angew. Chemie - Int. Ed.* **44**, 7212–7215 (2005).

86. Shankhari, P., Scheifers, J. P., Hermus, M., Yubuta, K. & Fokwa, B. P. T. Unexpected Trend Deviation in Isoelectronic Transition Metal Borides A3T5B2 (A = group 4, T = group 9): Ti3Co5B2- vs. Perovskite-Type Studied by Experiments and DFT Calculations. *Zeitschrift fur Anorg. und Allg. Chemie* **643**, (2017).

Chapter 4: Follow the boride brick road: paving the way towards rational structure design

*Jan. P Scheifers, Boniface P.T. Fokwa**

Department of Chemistry, University of California Riverside, Riverside

Abstract

In the present manuscript we identify a new class of complex metal borides based on the intergrowth of the AlB_2-type and Re_3B-type structures containing over ten different hexagonal or orthorhombic structure types. All structures are built from the same primary building unit – a capped trigonal prism centered around a boron atom. The orthorhombic structures are tiling variations of a secondary building unit, which corresponds to two of those trigonal prisms. All structures can be described by the general chemical formula *(insert)*$A_{6-x}A'_xT_6B_{2+y}$ with $0 \leq x \leq 3$ and $0 \leq y \leq 7$ and the occurrence of 1D-chains of magnetically active elements in certain structures is explained. Moreover, we identify a common feature in the electronic structure related to the primary building unit, which may be the reason for the electronic stability. Lastly, we apply the structure-building principles to predict new structure types and compounds with highly interesting magnetic properties.

Introduction:

In the 21st century the careful and more efficient use of limited resources becomes more and more important. One way to achieve those goals in materials chemistry and related fields would be to deliberately synthesize compounds with ideal properties for certain applications. This strategy is sometimes called materials-by-design and promises an immense potential. A fundamental problem in solid-state chemistry and for intermetallics in particular is the fact that to this day most new crystal structures, i.e. structure types, are discovered serendipitously. Therefore, new materials are often obtained by modifying existing compounds, which limits the options for designing new materials. Few computational tools like the USPEX algorithm [87] are available to predict new crystal structures but the way they arrive at a certain prediction can be difficult to rationalize and their predictions can sometimes represent the wrong local minimum of the energy landscape.

Metal borides – a class of intermetallics – come in a huge structural variety. To this day over 800 different crystal structures have been reported [88] describing thousands of metal borides (ICSD database entries as of Dec 2019). They exhibit a unique range of exciting properties useful in many applications. *Rogl* classified metal borides by their metal-to-boron ratio (M:B) [16]. The metal-to-boron ratio can vary over three orders of magnitude from 0.015 in YB_{66} to 16 in $Nd_2Fe_{14}B$ [14,15]. Depending on M:B, the boron connectivity changes from 3D boron networks (M:B < 0.167) to 2D layers (M:B = 2) to 1D boron chains (M:B = 1) and finally isolated B atoms (M:B > 2.5) [89].

In order to describe and categorize this immense number of different crystal structures *Grin* [6] developed the intergrowth concept which partitions complex crystal structures of extended solids into segments of simple known structure types. This elegant concept can be used to describe several metal-rich borides, among many other compounds. One example is the intergrowth of the hexagonal AlB_2-type structure (*P*6/*mmm*) with the CsCl-type ($Pm\bar{3}m$) structure in Mo_2FeB_2, $Nb_7Fe_3B_8$ [90] and the series $(CrB_2)_nCrAl$ [91]. Another example is MoAlB and the series VB, V_2B_3 and V_3B_4 [92], which can be described as intergrowth of the AlB_2-type and the W-type structures. The borocarbides of Nb and Mo are intergrowth structures of the AlB_2-type and the NaCl-type [93].

A particularly interesting and fruitful group of borides are the complex metal-rich borides with M:B = 2 [17], which exhibit a number of different boron subunits - B_n-fragments - combined with isolated B-atoms. Additional to the structural diversity, exciting physical properties have been observed among these borides such as low-dimensional, potentially frustrated magnetism in $TiCrIr_2B_2$ [70] and NbFeB [94,95], high temperature ferromagnetism in $TiFe_{1-x}Os_{2+x}B_2$ (see **chapter 5**, manuscript in preparation) and $Nb_6FeIr_6B_8$ [26,96] as well as superconductivity in NbRuB [54,97]. In the following manuscript, we will elaborate how these and many other crystal structures (in total over 15 different structure types) are related. Furthermore, we then define an entire class of complex metal-rich borides based on our identification of fundamental and secondary building blocks. We will provide preliminary results on the underlying chemistry and the guiding principles and even make predictions for yet to be discovered crystal structures based on the herein identified structure building principles.

Structure-building principles

The class of complex metal-rich borides is defined by the existence of isolated capped T_6B-prisms, which stack along their (pseudo-) trigonal axis. T is a *4d* or *5d* late transition metal (group VII - X). The T_6B-prism corresponds to a Re_3B-type component. Each T_6B-prism has to be capped by three A-atoms, resulting in the primary building unit (PBU) A_3T_6B (see **Figure 12**). A is either a main group metal or an early-transition metal. Each T_6B-prism can be capped by its own three A-atoms or the A-atoms can be shared between T_6B-prisms. If A-atoms are shared, an equal number of A'-atoms occur in the structure, which are not capping any T_6B-prism. Together A- and A'-atoms form an AlB_2-type component with a B_n-fragment in the crystal structure. Thus, many of the crystal structures in this class are Re_3B-AlB_2 intergrowth structures. The size of the Bn-fragment in the AlB_2-component depends on the character of A: a borophile A-metal allows for larger B_n-fragments than a borophobe A-metal.

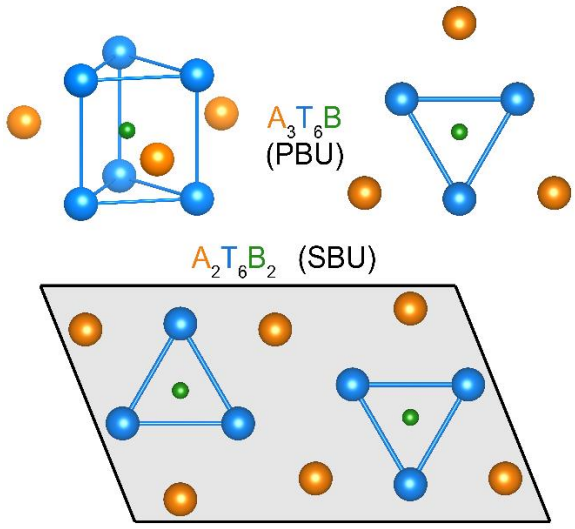

***Figure 12**: primary building unit and its projection (top); projection of the secondary building unit (bottom).*

In general, the crystal structures can either be orthorhombic or hexagonal depending on the A- and A'-atoms. If the number of A-atoms is a multiple of three (3A + 3A' or 6A + 0A'), a hexagonal structure is formed; in all other cases (5A+1A' or 4A+2A') an orthorhombic crystal structure is observed.

Furthermore, additional components can be inserted into those structures between the SBUs either expanding the AlB_2-component or as entirely different components. The resulting general chemical formula[1] for these compounds is

$$(insert)A_{6-x}A'_xT_6B_{2+y} \text{ with } 0 \leq x \leq 3 \text{ and } 0 \leq y \leq 7.$$

- The insert can be any compatible atom or group of atoms.
- A is an electropositive main group metal or an early transition metal and can be either borophile or borophobe
- A' is a (borophile) transition metal (group VI – X)
- T is an electronegative late-transition metal (4d or 5d, groups VII - X)
- x is the number of A'-chains and the number of shared-A atoms
- y is (a multiple of) the boron fragment

[1] Each formula unit contains two PBUs, resulting in two B-atoms and six T-atoms since the T-atoms are shared with the unit cell above and below in c-direction.

Two PBUs with opposite orientation form a secondary building unit (SBU), which can be arranged in many different tiling patterns such as aligned SBUs in NbRuB, offset SBUs in $Nb_{1-x}Os_{1+x}B$ or in a herring-bone pattern as in $Ti_{5-x}Fe_{1-y}Os_{6+x+y}B_6$ (see below). In case of orthorhombic $A_6T_6B_6$ (no insert, y = 0 and x = 4) borides, the tiling patterns can be described by shifting every other row of SBUs according to the following formula, if the unit cell settings are unified:

n * (1/6a + 1/2c) with $n \in \{\mathbb{z} \mid -3 \leq n \leq 3\}$[2],

if n = odd: zigzag B_∞-chain(s),

if n = even: $B_{2+|n|}$-fragment.

The hexagonal borides $A_6T_6B_{2+y}$ and $A_3A'_3T_6B_{2+y}$ can be derived from the orthorhombic $A_6T_6B_6$ borides following a similar tiling pattern. In this case every other PBU (or unit cell, respectively) is rotated by 180° around the c-axis and offset along one of the other axes.

Most of these compounds have between 96 and 105 valence electrons (VE) per generalized chemical formula independent of the size of the Bn-fragment, if we do not consider any inserts. This VE-count range coincides with a deep pseudo-gap at the Fermi-level E_F in the density of states (DOS), which is commonly associated with electronic

[2] $-3 \leq n \leq 3$ because of periodic boundary conditions.

stability. However, the topology of the B_n-fragment does not affect the electronic stability much, since those covalent bonds of the B_n-fragment are at very low energies in the DOS. Since all the structures are based on the A_3T_6B-PBU, the conclusion is that this building block is the cause of the structural stability and that it requires a certain number of VE. The ideal VE-count per PBU is 66 VE, but it can be as low as 63 VE/PBU.

Quaternary variants: distinguishing A and A'

The PBU in this class of borides is a capped trigonal prism with each A-atom capping only one T_6B prism, which ideally has the point group symmetry D_{3h}. However, the absence of the 3-fold rotation in orthorhombic cell reduces the point group of the PBU to C_{2v}. The lower symmetry requires two crystallographically different atoms to cap the rectangular faces of the trigonal prisms. The two different A-sites are indicated by the differing occupancies of Nb in $Nb_{1-x}Os_{1+x}B$ (3) [82].

Another possible option on how to arrange the PBUs is to have them share one or more capping A-atoms, which can have two consequences: *i*) the stoichiometry changes since less atoms are required to cap all T_6B-prisms or *ii*) a fraction of the usually capping A-atoms is no longer necessary to cap all the T_6B-prisms and those atoms are free to form other bonds in the structure while maintaining the same stoichiometry.

i) Assuming all capping A-atoms to be shared would obviously eliminate half of them. Thus, instead of six capping atoms for two T_6B-prisms, only three A-atoms are required, which yields a composition of $A_3T_6B_2$. This scenario is completely hypothetical as T_6B-prisms sharing all three capping atoms would result in large hexagonal channels along

the *c*-direction, which need to be filled somehow. However, the structure of $Nb_7Fe_3B_8$ - commonly described as AlB_2-CsCl intergrowth [90], can be viewed as a representation of case *i*) with all capping atoms being shared[3]. The resulting hexagonal channels are filled by stacks of B_6-rings alternating with an additional Nb-atom (see **Figure 13**). Subdividing the chemical formula into (Nb)($Fe_3Nb_6B_{2+6}$) shows Nb and the B_6-rings filling the channels in the $Fe_3Nb_6B_2$-framework, where Fe is the capping A-atom and Nb forms the T_6B-prisms[4].

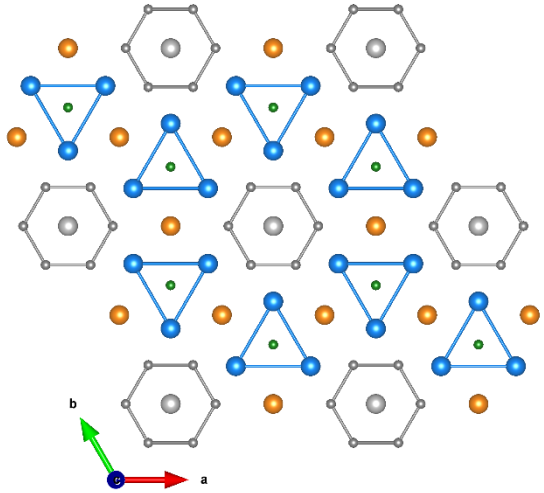

***Figure 13**: Structure of $Nb_7Fe_3B_8$.*

ii) This case is more relevant in context of complex ternary ATB borides with metal-to-boron ratio M/B = 2. In $Ti_{5-x}Fe_{1-y}Os_{6+x+y}B_6$, we have two Os_6B-prisms share a capping Ti-atom per SBU, so instead of six only five A-atoms are needed to cap all Os_6B-prisms. The remaining A'-atom (Fe) is not capping an OS_6B-prism and forms a linear Fe-chain along the c-direction on the twin boundary. Similarly, in NbOsB [46] two out of six

[3] Definitions for A and T are switched for $Nb_7Fe_3B_8$.

[4] Note that only three A-atoms and no A'-atoms are required, which would require adjusting the general chemical formula in section 1). Therefore, $Nb_7Fe_3B_8$ is not considered part of the Al_2-Re_3B intergrowth structures.

Nb-atoms are capping two Os_6B-prisms simultaneously, which results in two Nb-atoms not capping any Os_6B-prisms. Unsurprisingly, these two non-capping A'-atoms are selectively substituted in the isostructural quaternary $Ti_2Fe_{1-x}Ir_{3+x}B_3$ [98], where the Fe-atoms are arranged in two parallel chains along the *c*-direction.

Finally, if all three A-atoms surrounding each T_6B-prism are shared, the three other A'-atoms are not needed for capping the T_6B-prisms and instead they form three parallel chains running along the *c*-direction. As noted above, if all three capping atoms are shared, the compounds adopt a hexagonal structure. The three parallel chains of non-capping A'-atoms are thus forming a column of trigonal prisms. This is observed in $TiCrIr_2B_2$, where each capping Ti-atom is shared by two Ir_6B-prisms, which ultimately gives rise to Cr_3-triangles and trigonal B_4-fragments [70,99].

In summary, we find that with each capping A-atom that is shared by two T_6B-prisms, one chain of non-capping A'-atoms is generated (see **Figure 14**). If multiple A'-chains occur, they are adjacent to each other in the AlB_2-type component that contains the B_n-fragment. This leads to $A_{6-x}A'_xT_6B_{2+y}$ in the generalized chemical formula in section 1.

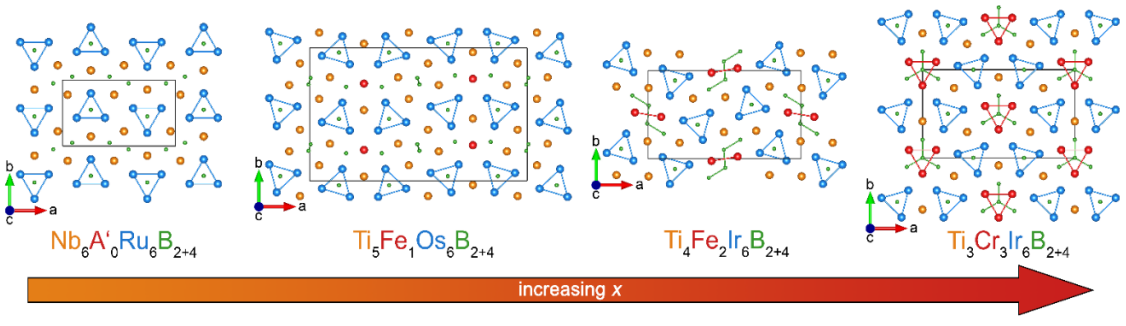

***Figure 14**: comparison of $A_{6-x}A'_xT_6B_6$ structures for varying x.*

Tiling of PBUs and SBUs:

In the series NbTB of ternary Niobium borides with M:B = 2 and T = Fe, Ru or Os, we find four different crystal structures: NbFeB crystallizes in the hexagonal ZrNiAl-type structure ($P\bar{6}2m$) [95], NbRuB (*Pmma*) [100], and the newly discovered $Nb_{1-x}Os_{1+x}B$ (*Pnma*) [82] are individual structure-types, while NbOsB (*Pbam*) belongs to the $Ti_{1+x}Rh_{2-x+y}Ir_{3-y}B_3$-type structure [46,101].

By limiting T to a group IIX transition metal it is insured that the valence electron count is constant though-out this series, which ensures that the structural differences are not caused by electronic effects[5].

All four structures are layered with two alternating layers and all boron atoms reside in trigonal metal prisms. In NbFeB, the Fe_6B-prisms are stacked along their trigonal faces forming columns, but they are not further connected to other Fe_6B-prisms. The Nb_6B-prisms are also stacked along their trigonal face, while they are interconnected via the edges that run parallel to the pseudo 3-fold axis. Since the Nb_6B-prisms are not connected by their rectangular faces, no short boron-boron contacts occur, i.e. no boron fragments. In contrast, the Nb_6B-prisms in the three other structures all share at least one (sometimes two) faces with other Nb_6B-prisms causing boron-boron bonds (around 1.8 Å). In NbRuB the boron-boron bond connects two boron atoms to a B_2-dumbbell, in NbOsB four boron atoms are connected to a zigzag B_4-fragment and in $Nb_{1-x}Os_{1+x}B$ the boron atoms inside

[5] a small deviation occurs for $Nb_{1-x}Os_{1+x}B$ due to mixed occupancies on the Nb-sites [82].

the Nb_6B-prisms form an infinite B_∞-chain as each Nb_6B-prism shares two of its three rectangular faces with other Nb_6B-prisms.

At a glance, these boron fragments and the four crystal structures appear quite different from each other. However, upon closer inspection we find adjoining stacks of T_6B-prisms with a distance of ca. 2.86 Å between each other for NbRuB and $Nb_{1-x}Os_{1+x}B$. This distance is less than 5% longer than the T-T distances in the trigonal face of the T_6B prisms alternates. The orientation of the T_6B-prisms alternates. If we unify the settings of the crystallographic unit cells with c-axis being perpendicular to the triangular faces of the T_6B-prisms and the adjoining stacks T_6B prisms being parallel to the *a'c'*-plane, we obtain the following (non-standard) space group symbols: *Pmam* for NbRuB and *Pnam* for $Nb_{1-x}Os_{1+x}B$[6]. Combining this with *Pbam* - the space group of NbOsB, it is obvious that the symmetry of the unit cells varies only in the *b'c'*-plane.

[6] NbRuB: *a' = a, b' = -c and c' = b*; Nb1-xOs1+xB: *a' = a, b' = c and c' = -b.*

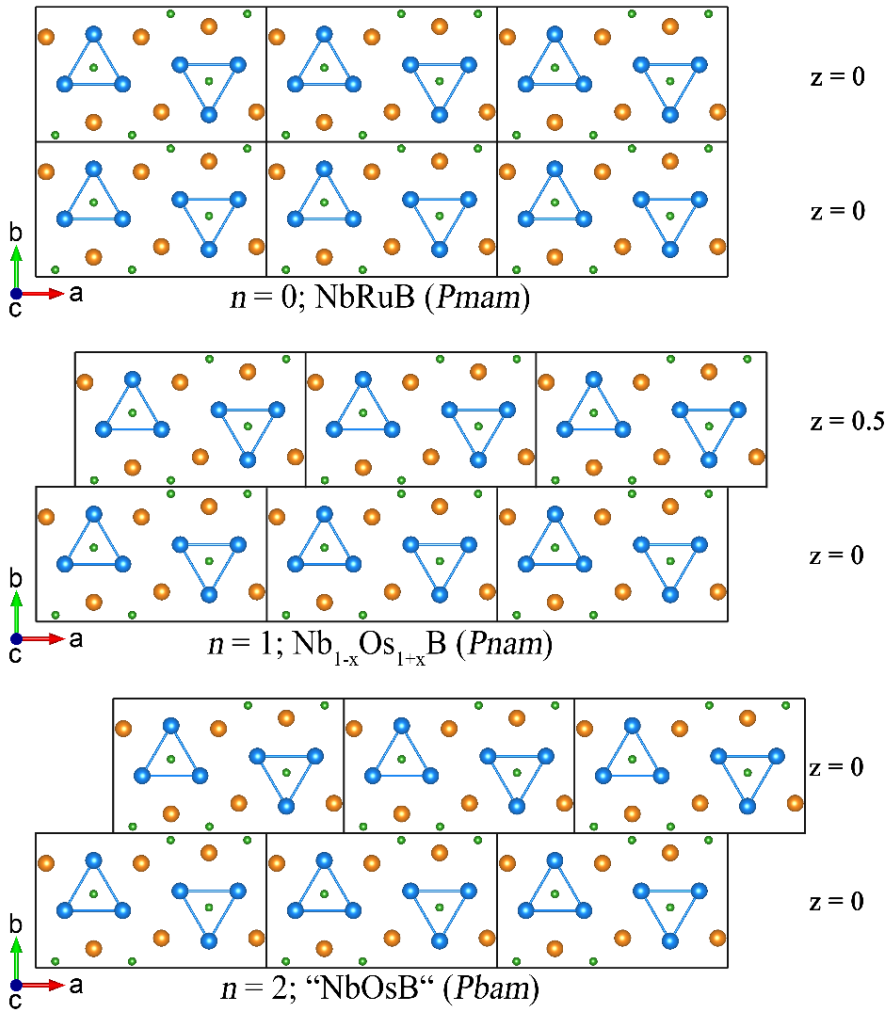

***Figure 15**: crystallographic shear along the a-direction results in three different crystal structures.*

Considering simply the projection along *c'*[7], one can see that the stacks of T_6B-prisms are aligned along *b'* in NbRuB but offset in $Nb_{1-x}Os_{1+x}B$ (**Figure 15**). If the unit cell of NbRuB is cut in half at 0.5*b'* the projection of NbRuB can be converted into the projection of $Nb_{1-x}Os_{1+x}B$ by shifting the halves against each other of ca. 1/6*a* (and 0.5*c'*)

[7] Allowed simplification since structures are layered with the two alternating layers perpendicular to *c'*. Changes in the *z*-component will be addressed if below.

along *a'*. This means the structures of NbRuB and $Nb_{1-x}Os_{1+x}B$ are related to each other by crystallographic shear. If the procedure is repeated, a structure is obtained that contains a zigzag B_4-fragment in the space group *Pbam* already indicating its close relation to the structure of NbOsB.

Taking a closer look at which part of the structures is shifted and how, we find that two adjoining T_6B-prisms and the six surrounding Nb-atoms capping the rectangular faces are the repeating SBU, which can be shifted against itself. The capping Nb-atoms form the face-sharing trigonal prisms of the AlB_2-type component, in which the Bn-fragment occurs. If the SBUs are stacked so they all align along the b-direction, the six Nb-atoms of adjacent SBUs form two edge-sharing triangles in the projection, i.e. two face-sharing trigonal prisms, which gives rise to the B_2-dumbbells in NbRuB. If the SBUs are shifted by 1/6*a*, the Nb-atoms in the projection form a rectangle. As the distance along the short side of this rectangle is too short and to accommodate two B-atoms in their preferred coordination the two adjacent SBUs have to be offset by 0.5*c*. If the SBUs are shifted by 2/6*a*, the Nb-atoms form four face-sharing trigonal prisms, which results in the zigzag B_4-fragment. Since no rectangles are formed in the projection, no offset of the SBUs in *c*-direction is required.

The relation to NbOsB is not as intuitive due to the glide-reflection twinning [102], but the resulting structure from the relation above for $n = 2$ contains the zigzag B_4-fragment and has the same space group as NbOsB. The difference is merely the orientation of B_4-

fragments to each other: they B_4-fragments in NbOsB are arranged in a herringbone pattern, while they are staggered but parallel to each other for n =2.

At this point, we have a simple relation - namely different possibilities for arranging the SBUs - between the three orthorhombic structures of NbRuB, $Nb_{1-x}Os_{1+x}B$ and NbOsB. The newly discovered $Ti_{5-x}Fe_{1-y}Os_{6+x+y}B_6$ (*Cmcm*, for details see **chapter 3**) represents another orthorhombic crystal structure based on the same SBUs. It is derived from n = 1 by unit cell twinning containing the corresponding zigzag B-chains. Consequently, the SBUs in $Ti_{5-x}Fe_{1-y}Os_{6+x+y}B_6$ are no longer arranged in rows along the *a*-direction but in a herringbone pattern. Thus, all orthorhombic structures are different tiling patterns of the SBU related by crystallographic shear and unit cell twinning. The arrangements of SBUs closely resemble different types of brickwork or tiling patterns as they occur in construction.

The hexagonal NbFeB is different from NbRuB and the Nb-Os-borides discussed above, because we have to look at the arrangement of the primary building units (PBUs) to find the connection to the orthorhombic structures instead of looking at the SBUs (see **Figure 16)**. The original hexagonal cell can be converted into an orthorhombic cell (*Cm2m*, $a' = a*\sqrt{3}$, $b' = b$ and $c' = c$), since *Cm2m* (non-standard settings of *Amm2*) is the maximal subgroup of $P\bar{6}2m$ with index 3 [103]. The projection of the unit cell shows that all PBUs (the Nb-capped T_6B-prisms) in NbFeB have the same orientation, while the orientation of the PBUs alternated along *a* for the orthorhombic structures. If every other PBU of NbFeB is rotated by 180° around *c* and shifted along *b*, we obtain the

NbRuB-type structure with B_2-dumbbells in face-sharing Nb-prisms. Similarly, if every other hexagonal unit cell in $TiCrIr_2B_2$ is rotated by 180° around the *c*-axis and shifted along *b,* the orthorhombic structure of the NbOsB with zigzag B_4 fragment is obtained[8]. This relation corresponds to glide-reflection twinning of the whole unit cell. Thus, the orthorhombic structures are specific tiling patterns of SBUs as we have shown above, while they also are specific tiling patterns of the hexagonal unit cells.

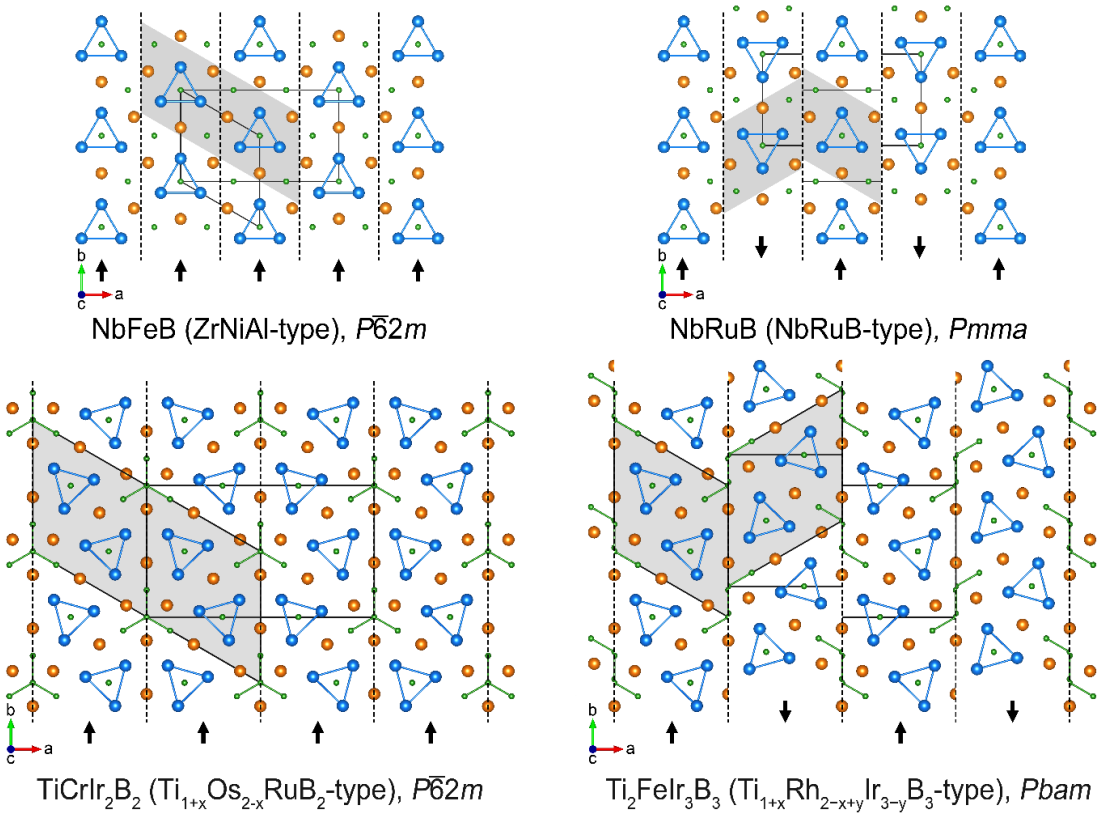

***Figure 16**: relation between hexagonal structures of NbFeB (top left) and $TiCrIr_2B_2$ (bottom left) with the orthorhombic structure of NbRuB (top right) and $Ti_2FeIr_3B_3$ (bottom right).*

[8] we do not distinguish between A and A' in TiCrIr2B2 here.

Hexagonal variants and the influence of A on the B_n-fragment

We have discussed two hexagonal structures above - NbFeB and $TiCrIr_2B_2$, both in $P\bar{6}2m$. While no A-atoms are shared in NbFeB, all three A-atoms are shared in $TiCrIr_2B_2$, which in turn leads to the trigonal A'-prisms (A' = Cr). In $Al_3Ru_9B_8$ (also $P\bar{6}2m$) all capping Al-atoms are shared by two Ru_6B-prisms [81]. The non-capping A'-atoms (here A' = Ru) are again forming a trigonal prism. In contrast to $TiCrIr_2B_2$, the A'_6-prisms are rotated by 60° around the *c*-axis and shifted by 0.5*c*. This leads to three zigzag B_∞-chains parallel to the *c*-direction instead of finite trigonal B_4-fragments. The two different orientations of the A'-prisms between $TiCrIr_2B_2$ and $Al_3Ru_9B_8$ are a consequence of the different size for A. If A is large, the $TiCrIr_2B_2$ structure is observed, but for smaller A the $Al_3Ru_9B_8$ structure is found.

In all three compounds the A-atom forms a strong chemical bond to boron atoms of the fragment and to the B-atom in the T_6B-prism. *A* is a boronphile metal, which includes all transition metal of group III - group X as well as Mg and Al. If A is replaced by an element, which does not form strong bonds to boron atoms, these bonds are avoided by decreasing the size of the boron fragment. Such borophobe elements are all the elements without an accessible *d*-subshell. This includes most main group metals like Li, Ga Ba or Sn as well as the transition metals Ag, Au, Zn *etc*. An interesting case is Cu with $3d^{10}4s^1$, which acts as borophobe metal in most cases, but the simple redox pair Cu^+/Cu^{2+} already shows that the *d*-orbitals can be accessed in some cases. Therefore, it is no surprise that a few examples like Pd_6CuB_3 [104] exists where Cu and B form strong

bonds. If the borophile A-atoms are replaced by borophobe A-atoms the terminal B-atoms of the B_n-fragment are lost to avoid A-B interactions (see **Figure 17**).

In case of NbFeB, the corresponding compound is In_3Ir_3B (both in $P\bar{6}2m$) [105]. In it a borophobe main-group metal, so the boron fragment of NbFeB - isolated B-atoms - lose the one and only B-atom resulting in In_3Ir_3B. Analogous, if Ti Is replaced by Li in $TiCrIr_2B_2$, the three terminal B-atoms of the trigonal B_4-fragment can no longer be accommodated and we arrive at $LiPt_3B$ (=$Li_3Pt_9B_3$, with A=Li, A'=Pt, T=Pt and one B-atom inside each Pt_6-prism) [106]. Lastly, Al can be replaced by Ga in $Al_3Ru_3B_8$, which causes every other B-atom of the zigzag B_∞-chain to be missing. The missing B-atom is unsurprisingly the outer one (from the center of the A'_6-prism), which would have a short B-A distance if present. The borophobe Ga and the missing B-atoms are observed in $Ga_{3-x}Ir_9B_5$ [107].

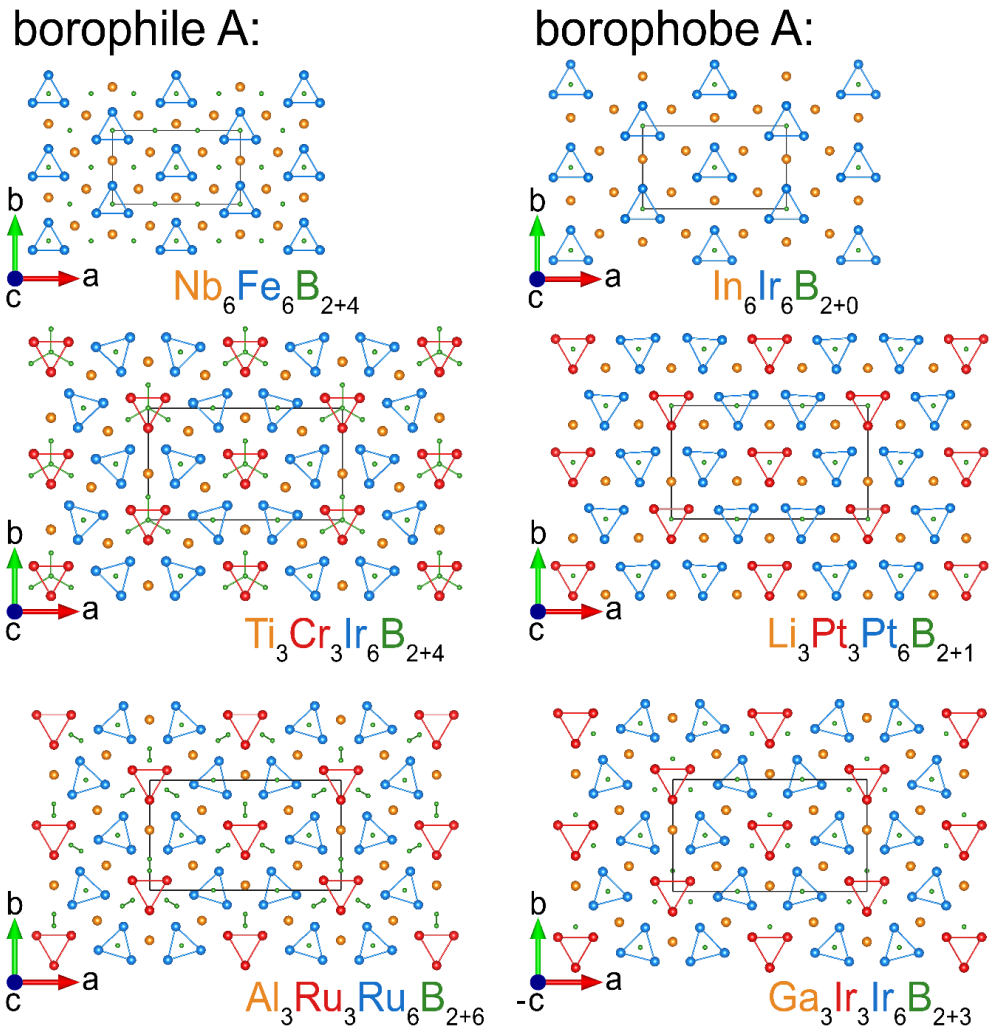

***Figure 17**: comparison between analogous compounds with borophile A (left) and borophobe A (right).*

In summary, each hexagonal structure can be formed with either a borophile or a borophobe A-element. The incorporation of a borophobe A-atom will eliminate the terminal B-atom(s) in the B_n-fragment in order to avoid short A-B distances, while the rest of the structure remains unchanged.

Insertions and eliminations: $Nb_6MIr_6B_8$, $Zn_5Ir_7B_3$ and Re_3B

So far, we have elucidated how different arrangements of PBUs and SBUs gives rise to several crystal structures, we have analyzed the relationship between capping A-atoms, shared A-atoms and non-capping A'-atoms and how this affects the crystal structures and we have explained how the boron-fragments depend on the characteristics of the A-atom. In the following paragraph we will show one more principle for how crystal structures are based on the same SBUs.

$Zn_5Ir_7B_3$ crystallizes in the space group *Pmma* [108] and contains one slab of SBUs. Following the above notation with *c* perpendicular to the two atomic layers in the unit cell, the space group symbol becomes *Pmam* (*a-cb*). This is already enough information to allow the conclusion that the slabs of the SBUs are aligned with each other along the *b*-direction ($n = 0$). The fact that A=Zn means that this structure contains either a small or no B_n-fragment since Zn is a borophobe metal.

A look at the actual crystal structure confirms the conclusions (see **Figure 18**). Interestingly, the slab of SBUs alternates with another slab along the b-direction. This second slab contains edge-sharing trigonal Ir_6B-prisms. The chemical formula can be split into the slab of A-capped T_6B prisms ($Zn_6Ir_6B_2$) and the second $Zn_4Ir_8B_4$-slab with edge-sharing Ir_6B prisms. Therefore, the structure of $Zn_5Ir_7B_3$ showcases that, additionally to different arrangements of SBUs, insertions in between the SBUs are possible in this class of complex metal-rich borides. Another great example for insertions

is the arrangement of SBUs with $n = 2$ (space group *Pbam*, zigzag B_4-fragment) and A being borophile. If sliced and sheared at an angle (cutting through the inner B-B bond of the B_4-fragment) a gap opens up, in which one Nb-atoms and two B-atoms can be inserted. This expands the B_4-fragment into the B_6-ring of the $Nb_7Ir_6B_8$ structure (deconstructed chemical formula $(Nb)Nb_6Ir_6B_{2+6}$) [109,110]. $Nb_7Ir_6B_8$ is an example for a cyclic twinning of the common SBU. $NbFe_{1-x}Ir_{6+x}B_8$ is a substitutional variant of $Nb_7Ir_6B_8$ with 1D Fe-chain [26]. These Fe-chains however are not a consequence of shared A-atoms as in the orthorhombic structures but from the selective substitution on the additional Nb-site.

Taking the NbRuB-type structure ($n = 0$) and eliminating all A-atoms will result in another experimentally observed structure. The elimination of Nb requires some rearrangement of the T_6B-prisms (every other prism shifts by $0.5c$ and $0.5b$) as the formerly capping A-atoms have to be replaced by T-atoms of adjacent T_6B-prisms to maintain the PBU. As the A-atoms are eliminated, the B_n-fragment is also eliminated which resided inside trigonal prisms of the A-atoms. Thus, the resulting structure consists exclusively of T_6B-prisms with each T-atom capping a rectangular face of another T_6B-prism. This structure is realized in Re_3B (*Cmcm* or in unified notation *Amam* with *cb-a*) [111]. Alternatively, the NbRuB-type structure can be considered an insertion of an AlB_2-type component into the Re_3B-type structure.

In this section, we have shown that insertions (and eliminations) are an important structure building principle in this class of crystal structures.

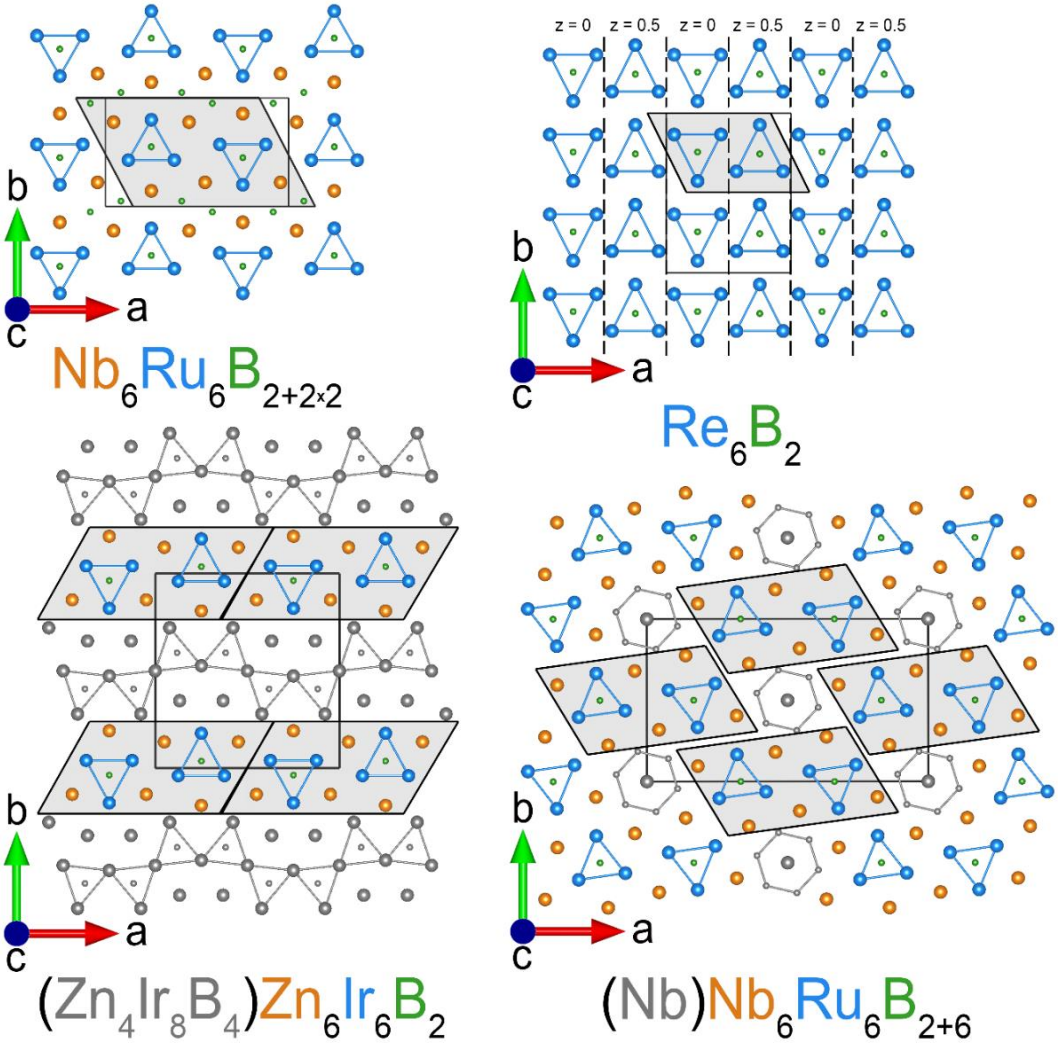

***Figure 18**: relation between the SBU (gray area) observed in NbRuB to other borides with insertions (gray atoms, bottom) and Re_3B (top right).*

Electronic structure

The narrow VE-count range has a couple interesting implications: If the A-metal is an electron-poor element such as Li, the T-metal has to be an electron-rich transition metal if the size of the Bn-fragment is the same. Taking $LiPt_3B$ as an example, A being the electron-poor Li requires the electron-rich Pt as A' and T-metals. For $TiCrIr_2B_2$ on the

other hand, the VE-count is identical (102 VE), but the electron-rich Pt (10 VE) on the A'-site has been replaced by Cr (6 VE), while Li (1 VE) and replaced by Ti (4 VE). The VE-count on the T-site decreases by only one VE per atom. The additional B-atoms of the larger B_n-fragment (borophile A) compensate for the rest. Analogous, the Nb_3Fe_6B-PBU in NbFeB has 66 VE, if the electron-rich Nb is replaced by the electron-poor Indium (3 VE), the VE-count on the T-site has to increase by 1 VE to counteract the VE loss. Thus, the PBUs of NbFeB and In_3Ir_3B are isoelectronic. The same holds true for the parent Ru_3B, where each Re-based PBU is capped by Re, which again makes a total of 66VE.

Another conclusion is that if the metal-atoms are relatively electron-poor, the size of the B_n-fragment must increase to maintain the VE-count per unit cell as long as a borophile A allows for that, e.g. $Al_3Ru_9B_8$ compared to $TiCrIr_2B_2$.

We calculated the total energies for multiple compounds with different tiling patterns while keeping the composition the same ($A_6T_6B_6$) and found energy differences between different structures to be as low as 8 meV/f.u. This is not surprising because the PBUs are not changed between structures only the tiling of the SBUs and whether A-atoms are shared or not.

Predictions

The identified building blocks and structure building principles not only help to categorize compounds and understand structural relationships but can also be applied to predict entirely new crystal structures.

In section 1) we implied a tiling pattern, which has not been discussed so far since it has not been observed experimentally, but the structure building principles presented here strongly suggest that it exists. For $n = 1$, a single zigzag B_n-chain occurs in $Nb_{1-x}Os_{1+x}B$. If $n = 3$, the SBUs are staggered (offset by 0.5 *a*' and 0.5 *c*'), which gives rise to two adjacent zigzag B_∞-chains parallel to the *c*'-direction (see **Figure 19**). The space group symbol for this structure is *Imma* (or *Imam* in the unified notation), which is the common supergroup of *Pmma*, *Pbam* and *Pnma*. Since no A-atom is shared, the chemical composition is ATB ($=A_6T_6B_6$), where A is a borophile metal. The VE-count/f.u. should be between 16 VE and 17.5 VE.

Unfortunately, there is a huge number of metal combinations for A and T that fulfill those requirements, but our prediction would be that A is an early transition-metal , which is electron-rich compared to other A-metals, because the two parallel B_∞-chains resemble the CrB-type structure. As a consequence, T has to be relatively electron-poor for a late-transition metal. One of many possible combinations is VRuB (16 VE), but we have not obtained the predicted structure in our experiments yet.

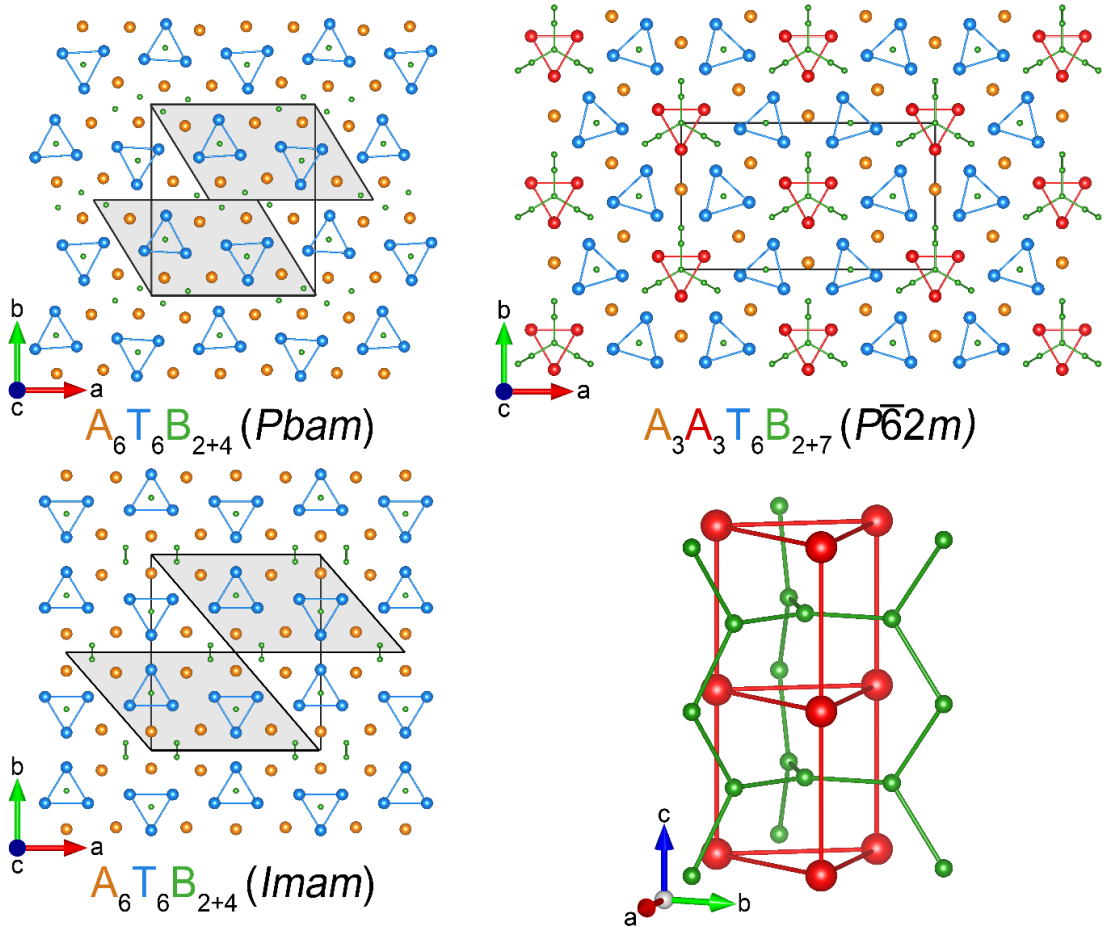

***Figure 19**: predicted structures of ATB with n = 2 (top right) and ATB with n = 3 (bottom left) as well as the structure of $AlMnRu_2B_3$ (top right) with perspective view of the Mn_3B_7 motif (bottom right)*

Another prediction is the combination of zigzag B_∞-chains in the $Al_3Ru_9B_8$ structure with the trigonal B_4-fragment of $TiCrIr_2B_2$. The central B-atom of the B_4-fragments could connect the three B_∞-chains. This kind of $^1{}_\infty B_7$-fragment has been found in $U_5Mo_{10}B_{24}$, but without the ideal 3-fold symmetry [112].

Since the VE-count of $Al_3Ru_9B_8$ is already 105 VE, which does not allow for another B-atom in the structure, we would suggest replacing the A'-metal (here Ru) by a transition metal of group VII such as Mn to remove 3 VE. This allows exactly one additional B-

atom per unit cell and the resulting composition is $AlMnRu_2B_3$ ($=Al_3Mn_3Ru_6B_9$). The borophile Al can remain as the A-atom because it allows the existence of a large B_n-fragment. This compound is predicted to show magnetic ordering.

Conclusion

In conclusion, we have defined a new class of complex metal-rich borides, that is based on the Re_3B-AlB_2 intergrowth and establish the underlying structure-building principles. All structures are based on capped trigonal prisms A_3T_6B as the primary building unit with 63 to 66 VE. A can be either a borophile or borophobe metal. If A is borophile and no A-atom is shared among two T_6B-prisms a boride with the chemical formula ATB is observed. The structure of ATB is hexagonal if the PBUs have all the same orientation or orthorhombic if PBUs have an antiparallel orientation. For the latter, two PBUs form a secondary building unit and each tiling pattern of those SBUs corresponds to an individual structure type and characteristic B_n-fragments. For each A-atoms shared between two T_6B-prisms, a 1D chain of non-capping A'-atoms occurs in the structure. Furthermore, we are able to show that additional subunits can be inserted in between the SBUs. Based on these structure-building principles, we can relate at least 13 different structure types to each other and use the same principles to make predictions for entirely new crystal structures. In the future, a framework like the one presented here will enable the easy categorization of new crystal structures and the underlying structure-building principles may even allow to rationally design compounds with new crystal structures and desirable properties.

References

6. Grin', Y. N. The Intergrowth Concept as a Useful Tool to Interpret and Understand Complicated Intermetallic Structures. in *Modern Perspectives in Inorganic Crystal Chemistry* 77–96 (Springer Netherlands, 1992). doi:10.1007/978-94-011-2726-4_5.

14. Richards, S. M. & Kaspar, J. S. The crystal structure of YB66. *Acta Crystallogr. Sect. B Struct. Crystallogr. Cryst. Chem.* **25**, 237–251 (1969).

15. Givord, D., Li, H. S. & Moreau, J. M. Magnetic properties and crystal structure of Nd2Fe14B. *Solid State Commun.* **50**, 497–499 (1984).

16. Rogl, P. Competition Between Trigonal Prisms and other Coordination Polyhedra in Borides, Carbides, Silicides and Phosphides. in *Modern Perspectives in Inorganic Crystal Chemistry* 267–278 (Springer Netherlands, 1992). doi:10.1007/978-94-011-2726-4_13.

17. Iyer, A. K., Zhang, Y., Scheifers, J. P. & Fokwa, B. P. T. Structural variations, relationships and properties of M2B metal borides. *J. Solid State Chem.* **270**, 618–635 (2019).

26. Mbarki, M., St. Touzani, R. & Fokwa, B. P. T. Unexpected Synergy between Magnetic Iron Chains and Stacked B_6 Rings in $Nb_6Fe_{1-x}Ir_{6+x}B_8$. *Angew. Chemie Int. Ed.* **53**, 13174–13177 (2014).

46. Zheng, Q. *et al.* Synthesis, crystal structure and properties of the new superconductors TaRuB and NbOsB. *J. Phys. Condens. Matter* **27**, 415701 (2015).

54. Mbarki, M., Touzani, R. S., Rehorn, C. W. G., Gladisch, F. C. & Fokwa, B. P. T. New ternary tantalum borides containing boron dumbbells: Experimental and theoretical studies of Ta2OsB2 and TaRuB. *J. Solid State Chem.* **242**, 28–33 (2016).

70. Küpers, M., Lutz-Kappelman, L., Zhang, Y., Miller, G. J. & Fokwa, B. P. T. Spin Frustration and Magnetic Ordering from One-Dimensional Stacking of Cr_3 Triangles in $TiCrIr_2B_2$. *Inorg. Chem.* **55**, 5640–5648 (2016).

81. Hirt, S., Hilfinger, F. & Hillebrecht, H. Synthesis and crystal structures of the new ternary borides Fe3Al2B2 and Ru9Al3B8 and the confirmation of Ru4Al3B2 and Ru9Al5B8-x (x ≈ 2). *Zeitschrift fur Krist. - Cryst. Mater.* **233**, 295–307 (2018).

82. Forsythe, R., Scheifers, J. P., Zhang, Y. & Fokwa, B. P. T. HT-NbOsB: Experimental and Theoretical Investigations of a Boride Structure Type Containing Boron Chains and Isolated Boron Atoms. *Eur. J. Inorg. Chem.* **2018**, (2018).

87. Glass, C. W., Oganov, A. R. & Hansen, N. USPEX-Evolutionary crystal structure prediction. *Comput. Phys. Commun.* **175**, 713–720 (2006).

88. Hellenbrandt, M. The inorganic crystal structure database (ICSD) - Present and future. in *Crystallography Reviews* vol. 10 17–22 (Taylor & Francis, 2004).

89. Fokwa, B. P. T. Borides: Solid-State Chemistry. in *Encyclopedia of Inorganic and Bioinorganic Chemistry* 1–14 (John Wiley & Sons, Ltd, 2014). doi:10.1002/9781119951438.eibc0022.pub2.

90. Zheng, Q. *et al.* Ternary borides Nb7Fe3B8 and Ta7Fe3B8 with Kagome-type iron framework. *Dalt. Trans.* **45**, 9590–9600 (2016).

91. Ade, M. & Hillebrecht, H. Ternary Borides Cr_2AlB_2, Cr_3AlB_4, and Cr_4AlB_6: The First Members of the Series $(CrB_2)_nCrAl$ with $n = 1, 2, 3$ and a Unifying Concept for Ternary Borides as MAB-Phases. *Inorg. Chem.* **54**, 6122–6135 (2015).

92. Kota, S. *et al.* Synthesis and characterization of an alumina forming nanolaminated boride: MoalB. *Sci. Rep.* **6**, 1–11 (2016).

93. Hillebrecht, H. & Gebhardt, K. Crystal Structures from a Building Set: The First Boridecarbides of Niobium. *Angew. Chemie Int. Ed.* **40**, 1445–1447 (2001).

94. Kuzma, Y., Tsolkovskii, T. & Baburova, O. The Systems Nb-Fe-B and Nb-Co-B. *Inorg. Mater.* **4**, 950–953 (1968).

95. Kuzma, Y. B. CRYSTAL STRUCTURES OF NbFeB AND TaFeB COMPOUNDS,. (1969).

96. Sharma, N., Mbarki, M., Zhang, Y., Huq, A. & Fokwa, B. P. T. Structural-Distortion-Driven Magnetic Transformation from Ferro- to Ferrimagnetic Iron Chains in B_6-based $Nb_6FeIr_6B_8$. *Angew. Chemie Int. Ed.* **57**, 10323–10327 (2018).

97. Xie, W. *et al.* Fragment-based design of NbRuB as a new metal-rich boride superconductor. *Chem. Mater.* **27**, 1149–1152 (2015).

98. Scheifers, J. P. *et al.* Transformation of trigonal planar B 4 into zigzag B 4 unit within the new boride series (Ti 1–x M x) 3 Ir 3 B 3 (x = ½ for M = V-Mn and x = ⅓ for M = Mn- Ni). *Solid State Sci.* (2020).

99. Fokwa, B. P. T., Von Appen, J. & Dronskowski, R. Synthesis of a missing structural link: The first trigonal planar B 4 units in the novel complex boride

Ti1+xOs 2-xRuB2 (x = 0.6). *Chem. Commun.* 4419–4421 (2006) doi:10.1039/b608903h.

100. Mbarki, M., Touzani, R. S. & Fokwa, B. P. T. Experimental and theoretical investigations of the ternary boride NbRuB with a layerlike structure type. *Eur. J. Inorg. Chem.* 1381–1388 (2014) doi:10.1002/ejic.201301488.

101. Goerens, C. & Fokwa, B. P. T. The complex metal-rich boride Ti 1xRh 2-xyIr 3-yB 3 (x=0.68, y=1.06) with a new structure type containing B 4 zigzag fragments: Synthesis, crystal chemistry and theoretical calculations. *J. Solid State Chem.* **192**, 113–119 (2012).

102. Andersson, S. & Hyde, B. G. Twinning on the unit cell level as a structure-building operation in the solid state. *J. Solid State Chem.* **9**, 92–101 (1974).

103. Ivantchev, S., Kroumova, E., Madariaga, G., Pérez-Mato, J. M. & Aroyo, M. I. SUBGROUPGRAPH: A computer program for analysis of group-subgroup relations between space groups. *J. Appl. Crystallogr.* **33**, 1190–1191 (2000).

104. Sologub, O. L., Hester, J. R., Salamakha, P. S., Leroy, E. & Godart, C. Ab initio structure determination of new boride CePt 3 B, a distorted variant of CaTiO 3. **337**, 10–17 (2002).

105. Kluenter, W. & Jung, W. In3Ir3B, In3Rh3B and In5Ir9B4, the First Indium Platinum Metal Borides. *ChemInform* **37**, no-no (2006).

106. Mirgel, R. & Jung, W. The ternary alkali metal platinum borides LiPt3B, NaPt3B1+x and Na3Pt9B5 - new structure variants of the CeCo3B2 type. *J. Less-Common Met.* **144**, 87–99 (1988).

107. Petry, K., Klünter, W. & Jung, W. Zn3Pt9B4, Ga2, 7Ir9B5und Ga3Pt9B4, Zink- und Gallium-Übergangs-metallboride mit neuen Kanalstrukturen. *Zeitschrift fur Krist. - New Cryst. Struct.* **209**, 151–156 (1994).

108. Eibenstein, U., Klünter, W. & Jung, W. Zn5Ir7B3, Zn5Rh7B3 und Zn7+xRh9–xB3 (x≈0,4) – neue ternäre Zink-Platinmetallboride. *Zeitschrift für Anorg. und Allg. Chemie* **625**, 719–724 (1999).

109. Fokwa, B. P. T. & Hermus, M. All-Boron Planar B6 Ring in the Solid-State Phase Ti7Rh4Ir2B8. *Angew. Chemie Int. Ed.* **51**, 1702–1705 (2012).

110. Zheng, Q. *et al.* TM 7 TM' 6B 8 (TM = Ta, Nb; TM' = Ru, Rh, Ir): New compounds with [B 6] ring polyanions. *Inorg. Chem.* **51**, 7472–7483 (2012).

111. Aronsson, B., Bäckman, M., Rundqvist, S., Varde, E. & Westin, G. The Crystal Structure of Re3B. *Acta Chem. Scand.* **14**, 1001–1005 (1960).

112. Konrad, T. & Jeitschko, W. U5Mo10B24, a boride containing three different kinds of boron polyanions. *Journal of Alloys and Compounds* vol. 233 (1996).

Chapter 5: High-T_c ferromagnetic boride $TiFe_{1-x}Os_{2+x}B_2$

*Jan P. Scheifers, Nika G. Bakshi, Justin Flores, Boniface P.T. Fokwa**

Abstract:

Herein, we present the synthesis and properties of a new ferromagnetic metal-boride $TiFe_{0.64(1)}Os_{2.36(1)}B_2$ with a Curie temperature of 523(2) K It is synthesized from the elements by arc-melting and its structure is elucidated and confirmed by single crystal and powder X-ray diffraction. It belongs to the $Ti_{1+x}Os_{2-x}RuB_2$-type structure and its unit cell contains equilateral triangles of iron atoms. In contrast to the isostructural $TiCrIr_2B_2$, we do observe mixed occupancy of the Fe-site, but the ordering temperature, the Weiss constant and the magnetic moment are all significantly higher for $TiFe_{0.64(1)}Os_{2.36(1)}B_2$. indicating that the magnetic order changes from ferrimagnetic in $TiCrIr_2B_2$ to ferromagnetic in $TiFe_{0.64(1)}Os_{2.36(1)}B_2$.

The results are supported by DFT calculations, which reproduce the experimental magnetic moment with excellent agreement. They also reveal very little energy difference between different magnetic models as long as the Fe-atoms stacked on top of each other in the c-direction interact ferromagnetically with each other. This indicates that the stacked Fe-triangles act more like individual chains than like triangles despite the short Fe-Fe distance of 2.648(5) Å.

Introduction:

Complex metal-rich borides show an astonishing variety of crystal structures featuring small B_n fragments that can be derived from the infinite, graphene-like honeycomb layers of the AlB_2-type structure [18]. In many cases selective substitution can be used to introduce magnetically active *3d* elements into existing crystal structures. A great example is the $Ti_7Rh_4Ir_2B_8$-type structure of $Nb_7Ir_6B_8$ [110], where the substitution of the early transition metal by Fe leads to the formation of 1D Fe-chains in $Nb_6FeIr_6B_6$ [26] and ferromagnetic ordering above room temperature. Similarly, site selective substitution yields 1D chains of Mn or Fe in the $Ti_3Co_5B_2$-type structure, while adjusting the valence electron count (VEC) in the solid solution series $Sc_2Fe(Ru/Rh)_5B_2$ [66] or $Sc_2Fe(Ru/Ir)_5B_2$ [67] allows to finely tune the magnetic properties. A recent example is $TiCrIr_2B_2$ [113]. This compound combines a rare trigonal B_4-fragment with equilateral triangles of Cr in its crystal structure. Predominantly anti-ferromagnetic interactions between the Cr-atoms and their triangular arrangement may indicate a good candidate material for geometric frustration. Magnetic measurements however revealed ferrimagnetic ordering at 275 K and only weak frustration. Here, we use the strategy of selective substitution to obtain two new compounds - $TiFe_{1-x}Os_{2+x}B_2$ and $TiNi_{1-x}Os_{2+x}B_2$ - with magnetically active *3d*-elements in the $Ti_{1.6}Os_{1.4}RuB_2$-type structure [114]. We present their crystal structures based on single crystal diffraction experiments and calculate their electronic properties using ab-initio methods. $TiFe_{1-x}Os_{2+x}B_2$ turned out to be the boride with B_n-fragment with the highest ordering temperature to this date as it orders ferromagnetically at 523(3) K.

Experimental:

Powders of the elements were mixed in the following ratios 2 Ti : 1 Fe : 4 Os : 4 B and 1 Ti : 1 Ni : 2 Os : 2 B before being pressed into pellets. The pellets were inserted into a custom-build arc-furnace and briefly melted under purified Ar by applying a current of 25 A. The obtained samples are air-stable metallic beads that are crushed for further characterization.

The powder X-ray diffraction patterns for both samples were collected with a RIGAKU MiniFlex 600 benchtop diffractometer used in reflection geometry, equipped with graphite monochromatized Cu-$K_{\alpha 1}$ (λ = 1.543 Å) radiation and a scintillation counter (SC-70) detector. A Rietveld refinement was performed using the FullProf suite 2017 [55] and the results were plotted with WinPLOTR. [74]

Irregularly shaped single crystals were extracted from the fragments of the broken beads under a light microscope. The single-crystal intensity data were collected on a RIGAKU XtaLABmini benchtop diffractometer with graphite monochromator using Mo-K_{α} (λ = 0.71073 Å) radiation with SHINE optics. An analytical numeric absorption correction of the intensity data was necessary due to the heavy metals. [115] The structure solution and refinement (full matrix least squares on F^2) were carried out with the SHELX-2008 software suite [57,116]. The non-centrosymmetric space group $P\bar{6}2m$ (no. 189) was found to be correct during the refinement for both compounds after merohedral twinning had been treated using the TWIN command in SHELX (twin law $\bar{1}00$ $0\bar{1}0$ 001). All metal atoms were refined with anisotropic displacement parameters, while the boron positions

were refined isotropically without any restrictions. To finalize the results Addsym and Structure Tidy routines implemented in Platon [117] and embeded in WINGX 2014.1 [75,116] were performed and the obtained structure was visualized using VESTA. [118]

Computational Methods: Electronic structure and total energy calculations were performed using Vienna *ab-initio* simulation package (VASP) [77,78] with the projector augmented wave (PAW) method of Blöchl. [60] For all calculations the generalized gradient approximation (GGA) was used and exchange and correlation were treated by the Perdew-Burke-Enzerhoff (PBE) functional. [119] The k-point grid was generated using the Monkhorst package. [79] For the calculations a simplified structural model has been used were we assumed the site 3*f* to be fully occupied by Fe. In case of $TiFe_{0.64}Os_{2.36}B_2$, this does not affect the electronic structure as Os and Fe have the same valence electron count (VEC). All electronic structures have been calculated after an initial structure relaxation and the Fermi-level E_F is set to 0 eV.

Results:

The powder diffraction data showed reflections that could be indexed with a hexagonal cell as well as reflections that matched with Os. The powder diffraction pattern was refined using an initial model based on $TiCrIr_2B_2$ ($Ti_{1+x}Os_{2-x}RuB_2$-type structure, space group $P\bar{6}2m$, no. 189), where Cr is replaced by Fe or Ni respectively and Ir by Os. Additionally, mixed occupancy of Fe and Os (Ni and Os, respectively) on the *3f* site has been refined.

Table 4: *Results of the Rietveld refinements for $TiFe_{1-x}Os_{2+x}B_2$ and $TiNi_{1-x}Os_{2+x}B_2$.*

compound	$TiFe_{1-x}Os_{2+x}B_2$	Os
Space group	$P\bar{6}2m$	$P6_3/mmc$
a [Å]	8.826(1)	2.7175(7)
c [Å]	3.0282(5)	4.308(2)
x	0.32(1)	-
R_{Bragg}	8.91	4.74
R_f	5.34	3.70
Fraction [wt.-%]	58(1)	41.5(9)

compound	$TiNi_{1-x}Os_{2+x}B_2$	Os
Space group	$P\bar{6}2m$	$P6_3/mmc$
a [Å]	8.8316(9)	2.7288(2)
c [Å]	3.0351(4)	4.3303(4)
x	0.40(1)	-
R_{Bragg}	9.06	4.25
R_f	5.61	1.95
Fraction [wt.-%]	76(1)	24.1(6)

Table 5: *Results of the single crystal refinements for $TiFe_{0.64}Os_{2.36}B_2$ and $TiNi_{0.68}Os_{2.32}B_2$.*

Chemical formula	$TiFe_{0.64}Os_{2.36}B_2$	$TiNi_{0.68}Os_{2.32}B_2$
Formula weight [g/mol]	554.14	550.27
Crystal system, space group	Hexagonal, $P\bar{6}2m$, no. 189	
Lattice parameters	a=b=8.8183(4) Å c=3.0199(2) Å α=β=90° ɣ=120°	a=b=8.841(1) Å c=3.0325(4) Å α=β=90° ɣ=120°
Volume [$Å^3$], Z	203.37(2), 3	205.27(5), 3
Density [Mg/m^3]	13.574	13.354
Absorption coefficient [mm^{-1}]	116.068	114.293
F(000)	684	682
Θ range [°]	2.667 to 33.754	2.660 to 33.646
Index ranges	$-13 \leq h \leq 13$, $-13 \leq k \leq 13$, $-4 \leq k \leq 4$	$-13 \leq h \leq 10$, $-13 \leq k \leq 13$, $-4 \leq k \leq 4$
Reflections (collected / independent / R(int))	3638 / 346 / 0.0926	1823 / 341 / 0.0737
data/restraints/parameters	346 / 0 / 22	341 / 0 / 22
Goodness-of-fit on F^2	1.074	1.106
Final R indices (I>2sigma(I))	R1 = 0.0279 wR2 = 0.0592	R1 = 0.0387 wR2 = 0.0844
R indices (all data)	R1 = 0.0312 wR2 = 0.0608	R1 = 0.0430 wR2 = 0.0872
Absolute structure parameter	0.01(5)	-
Extinction coefficient	0.0026(6)	0.0000(6)
Largest diff. Peak / hole [e-/$Å^3$]	3.024 / -4.127	4.607 / -3.970

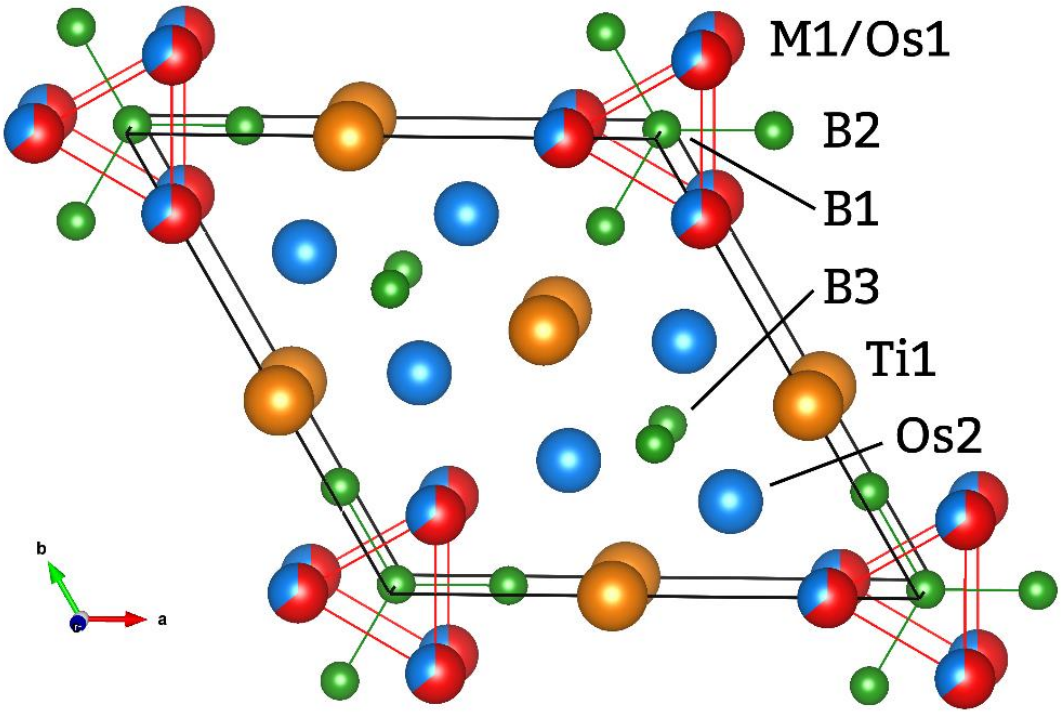

***Figure 20**: crystal structure of $TiM_{1-x}Os_{2+x}B_2$ (M = Fe or Ni: red, Os: blue, Ti: orange and B: green).*

Single crystal structures for both compounds are in excellent agreement with the Rietveld refinements (see **Table 5**). The structures (see **Figure 20**) are isostructural with $TiCrIr_2B_2$, where the site *6j* is occupied by Os instead of Ir. On the Cr site (*3g*) we find a mixture of Fe and Os and Ni and Os, respectively. The sites of Ti (also *3g*) and of the three different boron atoms (B1 on *1a*, B1 on *3f* and B3 on *2d*) are the same as in $TiCrIr_2B_2$. This leaves the most striking structural feature of this crystal structure - the trigonal planar B_4-fragment - unchanged.

The B-B bonds distances are 1.87(4) Å and 1.85(6) Å for $TiFe_{0.64}Os_{2.36}B_2$ and $TiNi_{0.68}Os_{2.32}B_2$, respectively, which is in the normal range for B-B bonds in metal borides but slightly longer than in $TiCrIr_2B_2$. This seems counterintuitive as both Cr and Ir are larger than Fe, Ni and Os. Despite this fact, the volumes of $TiFe_{0.64}Os_{2.36}B_2$ and $TiNi_{0.68}Os_{2.32}B_2$ are both larger than the volume of $TiCrIr_2B_2$. That is because the *a* lattice parameter is about 3% larger but the *c* lattice parameter is roughly 5% shorter. The change in the aspect ratio also affects the other important feature of the structures: equilateral triangles of the *3d* transition metals Fe and Ni, respectively. The distances within the equilateral triangles are 2.648(5) Å and 2.674(5) Å, while the distances between the triangles in *c*-direction are 3.0199(2) Å and 3.0325(5) Å for $TiFe_{0.64}Os_{2.36}B_2$ and $TiNi_{0.68}Os_{2.32}B_2$, respectively. Combined with the smaller atomic radii for Fe and Ni compared to Cr, the interactions between these atoms are expected to be weaker within each triangle, but stronger along the *c*-direction. This is important as the site is mainly occupied by the magnetically active *3d* metal. $TiCrIr_2B_2$ has been found to be a weakly frustrated, itinerant ferrimagnet. From a crystal structure point of view both compounds can be expected to be even less frustrated than $TiCrIr_2B_2$. Taking into account that many complex transition metal-rich borides with Ni do not show magnetic ordering, no magnetic ordering is expected for $TiNi_{0.68}Os_{2.32}B_2$.

***Table 6**: Wyckoff sites, fractional coordinates, occupancies and equivalent displacement parameters for all atoms in $TiFe_{0.642(9)}Os_{2.358(9)}B_2$ and $TiNi_{0.68(1)}Os_{2.32(1)}B_2$ as obtained from single-crystal X-ray diffraction.*

atom	Wyckoff site	*x*	*y*	*z*	Occupancy [%]	U_{eq} [Å²]
Os2	*6j*	0.4629(1)	0.2747(1)	0	100	0.004(1)
Fe1	*3g*	0.1734(1)	0.1734(1)	0.5	64.2(9)	0.008(1)
Os1	*3g*	0.1734(1)	0.1734(1)	0.5	35.8(9)	0.008(1)
Ti1	*3g*	0	0.4205(7)	0.5	100	0.004(1)
B3	*2d*	0.3333	0.6667	0.5	100	0.006(7)
B2	*3d*	0	0.212(4)	0	100	0.011(7)
B1	*1a*	0	0	0	100	0.05(3)
atom	Wyckoff site	*x*	*y*	*z*	Occupancy [%]	U_{eq} [Å²]
Os2	*6j*	0.4633(1)	0.2747(2)	0	100	0.005(1)
Ni1	*3g*	0.1746(4)	0.1746(4)	0.5	68(1)	0.009(1)
Os1	*3g*	0.1746(4)	0.1746(4)	0.5	32(1)	0.009(1)
Ti1	*3g*	0	0.420(1)	0.5	100	0.006(2)
B3	*2d*	0.3333	0.6667	0.5	100	0.01(1)
B2	*3d*	0	0.209(6)	0	100	0.01(1)
B1	*1a*	0	0	0	100	0.02(2)

Another important aspect for metal-rich borides is the valence electron count (VEC) as it has been shown to limit the composition space in which certain structures such as the perovskite structure can exist [120]. The previously reported $TiCrIr_2B_2$ and $Ti_{1.6}Os_{2.4}B_2$ have a VEC of 34 e^-/f.u. (102 e^-/u.c.) and 31.6 e^-/f.u. (94.8 e^-/u.c.), respectively. $TiFe_{0.64}Os_{2.36}B_2$ also has a VEC of 34 e^-/f.u. (102 e^-/u.c.) identical to the VEC of

$TiCrIr_2B_2$, while $TiNi_{0.68}Os_{2.32}B_2$ has 35.4 e^-/f.u. (106.2 e^-/u.c.). The aliovalent substitutions of Cr by Fe and Ir by Os cancel each other out and an isoelectronic and isostructural compound with a different magnetically active element is obtained. Despite the similarities with $TiCrIr_2B_2$, the magnetic properties of $TiFe_{0.64}Os_{2.36}B_2$ are distinctly different as we are going to demonstrate below.

DFT results

No significant differences between the experimentally obtained structure and the relaxed structures are observed and the observed differences are expected for calculations using GGA and a simplified structural model.

The density of states (DOS) of both compounds (see **Figure 21**) shows a gap at -8 eV characteristic for metal-rich borides with finite B_n-fragments. Where we expect the other characteristic feature in the DOS of metal-rich borides - a deep pseudo-gap around the E_F, we find a large peak for $TiFeOs_2B_2$ instead. Looking at the partial DOS, this peak can be assigned to Fe, indicating an electronic instability, which is in many cases resolved by spin-polarization [121,122]. This peak at E_F is absent in $TiNiOS_2B_2$, which is another indication for unlikely spin-polarization in this compound.

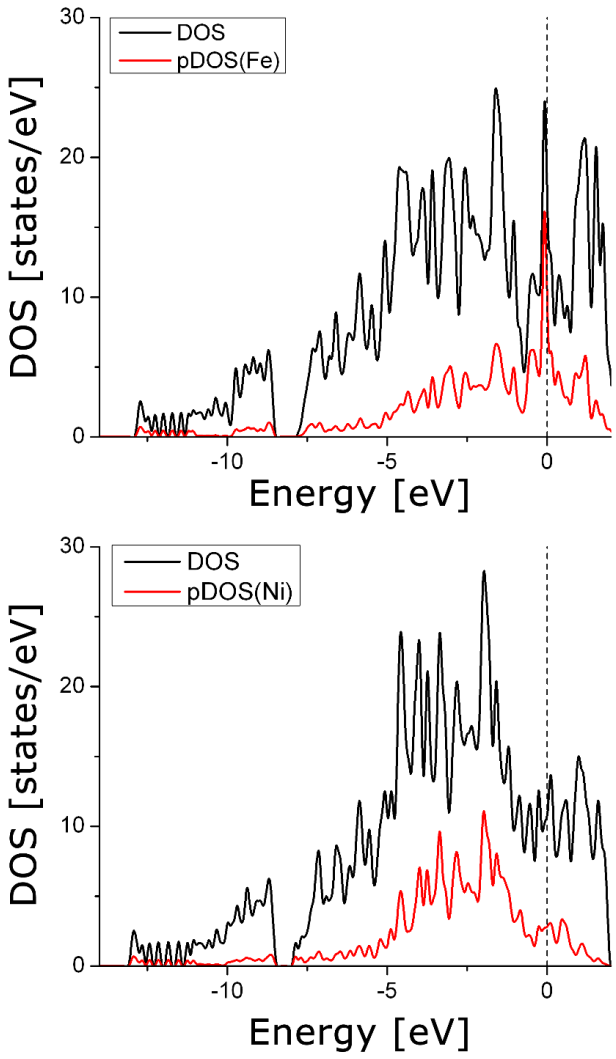

Figure 21: *non-spin polarized DOS of $TiFe_{1-x}Os_{2+x}B_2$ (top) and $TiNi_{1-x}Os_{2+x}B_2$ (bottom). The partial DOS of Fe or Ni, respectively, is shown in red.*

We performed spin-polarized calculations to identify the magnetic ground state of $TiFeOs_2B_2$ using an orthorhombic supercell (*Amm*2, $a' = nc$, $b' = a\sqrt{3}$, $c' = a$ with $n = 2$ or 3) and multiple magnetic models (see table) to test the strength and character of various Fe-Fe interactions. We can use three different criteria to distinguish the magnetic models: *i*) the interactions within a triangle (FM vs FiM), *ii*) the interactions between triangles in two adjacent layers (FM or AFM, in *a'*-direction) and *iii*) interactions between triangles in the same layer (FM or AFM, in the *b'c'*-plane). Form the total energy, we can deduce that spin-polarization of the electronic structure is preferred over a non-spin-polarized electronic structure. The magnetic ground state is calculated to be anti-ferromagnetically ordered with FM interactions for (*ii*) and (*iii*) and AFM interactions for (*i*). Moreover, we find that the interaction between triangles in the same layer (*iii*) is very weak. This seems

reasonable as the distances (center-to-center) between triangles is ca. 8.8 Å. The interactions along the *a'*-directions (*ii*) are very substantial and strongly favor FM interactions. Surprisingly, the interactions within each triangle (*i*) are weak and only slightly favor FM-triangles over FiM-triangles. In summary, we find that even though the Fe-Fe distance within a triangle is significantly shorter than the Fe-Fe distance along *c*, the interactions along *c* (*ii*) are much stronger than the interactions within a triangle (*i*). Thus, instead of stacked triangles the structure is more accurately described as a set of three individual, weakly coupled Fe-chains. Ferromagnetic interactions along each chain are strongly preferred, while ferromagnetic interactions between the three chains are only slightly favored.

The magnetic moment obtained from the DFT calculations is 1.84 μ_B per Fe-atom except for the models, for which the interactions along *c* (*ii*) are solely anti-ferromagnetic (then 0.16 μ_B per Fe-atom).

Magnetization of $TiFe_{1-x}Os_{2+x}B_2$

The powder of the Fe-containing sample reacts to a magnet in its proximity. This behavior stops at elevated temperatures. Therefore, we expect ferromagnetic ordering with a Curie-temperature T_c above room temperature. Indeed, we find the susceptibility to increase at T_c = 523(2) K. Above that temperature the inverse susceptibility is approximately linear indicating paramagnetic Curie-Weiss-behavior. A linear fit in the paramagnetic regime gives a negative *y*-intercept and thus a positive Weiss-constant Θ = 554(3) K. Such a large, positive Θ indicates strong ferromagnetic interactions to be the

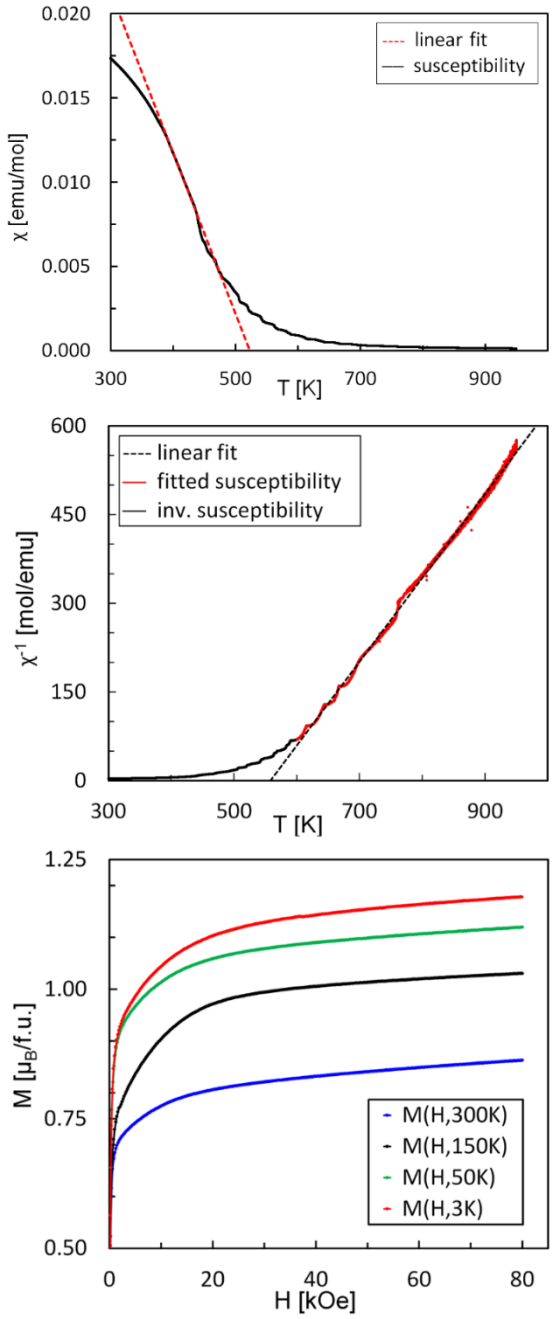

Figure 22: *(top) high-temperature susceptibility data (black) with tangent (red dashed) to the inflection point; (middle) inverse susceptibility with linear fit (back dashed) to the paramagnetic regime (600K - 950K in red); (bottom) magnetization M plotted against the external magnetic field strength H at different temperatures for* $TiFe_{1-x}Os_{2+x}B2$.

primary type of interactions in this compound. This agrees nicely with the strong ferromagnetic Fe-Fe interactions along the c-direction (*ii*) obtained from the DFT calculations. The hysteresis plots at three different temperatures show soft magnetic behavior and confirm the non-zero magnetic moment even at 300 K in $TiFe_{0.64}Os_{2.36}B_2$. The maximum magnetic moment per formula unit at 3 K is ca. 1.2 μ_B/f.u. (data corrected for 41.5(9) wt.-% Os). The calculated moment is 1.84 μ_B/f.u., but this is obtained for the ideal $TiFeOs_2B_2$ without mixed occupancy on the Fe-site. Taking the mixed occupancy into account results in a magnetic moment of 1.88 μ_B/Fe-atom, which is in almost perfect agreement with the calculated magnetic moment.

The large magnetic moment per Fe-atom and the large Weiss-constant Θ together confirm the ferromagnetic behavior. A possible reason why we observe ferromagnetic instead of anti-ferromagnetic behavior as predicted by the DFT calculations could be the weak interaction between triangles of the same layer (*i*), which would affect the observed magnetic ordering only at very low temperatures and in the absence of a magnetic field. The small, but non-zero magnetic field and the minimum temperature of 3 K may not be enough to observe the predicted anti-ferromagnetic ground state experimentally.

The complex metal-rich boride $Nb_6Fe_{0.77(2)}Ir_{6.23(2)}B_8$ also contains ferromagnetic Fe-chains along the *c*-direction, but instead of alternating with trigonal B_4-fragments the Fe atoms are sandwiched between hexagonal B_6-rings. [26,96] The Weiss-constant Θ and the ordering temperature of $TiFe_{0.64}Os_{2.36}B_2$ are even higher than for $Nb_6Fe_{0.77(2)}Ir_{6.23(2)}B_8$, where T_c = 350 K and Θ = 261 K. This observation can be explained by the smaller *c*-lattice parameter of $TiFe_{0.64}Os_{2.36}B_2$ (*c* = 3.02 Å compared to 3.3 Å for $Nb_6Fe_{0.77(2)}Ir_{6.23(2)}B_8$) and the proximity of Fe-chains to each other. One could furthermore speculate that the high ordering temperature for these complex metal-rich borides is caused by the Fe-chains interacting with a B_n-fragment. Other metal-rich borides with Fe-chains such as $Sc_2Fe(Ru/Ir)_5B_2$ order magnetically well below room temperature. [67]

Conclusion

In summary, we have synthesized two new metal borides $TiFe_{1-x}Os_{2+x}B_2$ and $TiNi_{1-x}Os_{2+x}B_2$ (with $x \approx 1/3$) by arc melting. Both isostructural compounds crystallize in the hexagonal $Ti_{1.6}Os_{1.4}RuB_2$-type structure with a trigonal B_4-fragment. The magnetically active elements Fe or Ni, respectively, form stacks of triangles with interatomic distances of about 3 Å. DFT calculations reveal a strong preference for ferromagnetic interactions along the c-direction, but overall an antiferromagnetic ground state is expected. However, the energy differences between AFM and FM ordering are very small due to the long distance between the stacks of triangles. Experimentally, we observe ferromagnetic ordering with a high Curie-temperature T_c of 523(2) K down to 2K. The Weiss constant Θ of 554(3) K reflects the strong FM interactions along the *c*-direction. This work could lead to more high-temperature magnetic borides and enable investigations on low-dimensional magnetism in extended metallic solids.

Acknowledgements

The authors would like to acknowledge the financial support in form of an NSF CARRER grand **(#1654780)** to B.P.T.F., the Dissertation Year Award from UC Riverside to J.P.S. as well as funding for J.F. via the NSF project Research Experience for Undergraduate Students **(MaCReu R'Side, #1359136).** The DFT calculations have been performed at the San Diego Supercomputing Center.

References

18. Scheifers, J. P., Zhang, Y. & Fokwa, B. P. T. Boron: Enabling Exciting Metal-Rich Structures and Magnetic Properties. *Acc. Chem. Res.* **50**, 2317–2325 (2017).

26. Mbarki, M., St. Touzani, R. & Fokwa, B. P. T. Unexpected Synergy between Magnetic Iron Chains and Stacked B_6 Rings in $Nb_6Fe_{1-x}Ir_{6+x}B_8$. *Angew. Chemie Int. Ed.* **53**, 13174–13177 (2014).

55. Rodriguez-Carvajal, J. *FULLPROF 2000: A Rietveld Refinement and Pattern Matching Analysis Program*. *Abstract of the Satellite Meeting on Powder Diffraction of the XV Congress of the IUCr, Toulouse, France* (2008).

57. Sheldrick, G. M. Crystal structure refinement with SHELXL. *Acta Crystallogr. Sect. C Struct. Chem.* **71**, 3–8 (2015).

60. Blöchl, P. E. Projector augmented-wave method. *Phys. Rev. B* **50**, 17953–17979 (1994).

66. Fokwa, B. P. T., Lueken, H. & Dronskowski, R. Rational synthetic tuning between itinerant antiferromagnetism and ferromagnetism in the complex boride series Sc2FeRu 5-nRhnB2($0 \leq n \leq 5$). *Chem. - A Eur. J.* **13**, 6040–6046 (2007).

67. Hermus, M., Yang, M., Grüner, D., DiSalvo, F. J. & Fokwa, B. P. T. Drastic Change of Magnetic Interactions and Hysteresis through Site-Preferential Ru/Ir Substitution in $Sc_2FeRu_{5-x}Ir_xB_2$. *Chem. Mater.* **26**, 1967–1974 (2014).

74. Roisnel, T. & Rodriguez-Carvajal, J. WinPLOTR: a Windows tool for powder diffraction patterns analysis. in *Materials Science Forum, Proceedings of the Seventh European Powder Diffraction Conference (EPDIC 7)* (eds. Delhez, R. & Mittenmeijer, E. J.) 118–123 (2000).

75. Farrugia, L. J. WinGX suite for small-molecule single-crystal crystallography. *J. Appl. Crystallogr.* **32**, 837–838 (1999).

77. Kresse, G. Vienna ab initio simulation package. (1999).

78. Kresse, G. & Hafner, J. Ab initio molecular dynamics for liquid metals. *Phys. Rev. B* **47**, 558–561 (1993).

79. Monkhorst, H. J. & Pack, J. D. Special points for Brillouin-zone integrations. *Phys. Rev. B* **13**, 5188–5192 (1976).

96. Sharma, N., Mbarki, M., Zhang, Y., Huq, A. & Fokwa, B. P. T. Structural-Distortion-Driven Magnetic Transformation from Ferro- to Ferrimagnetic Iron Chains in B_6 -based $Nb_6FeIr_6B_8$. *Angew. Chemie Int. Ed.* **57**, 10323–10327 (2018).

110. Zheng, Q. *et al.* TM 7 TM' 6B 8 (TM = Ta, Nb; TM' = Ru, Rh, Ir): New compounds with [B 6] ring polyanions. *Inorg. Chem.* **51**, 7472–7483 (2012).

113. Küpers, M., Lutz-Kappelman, L., Zhang, Y., Miller, G. J. & Fokwa, B. P. T. Spin Frustration and Magnetic Ordering from One-Dimensional Stacking of Cr_3 Triangles in $TiCrIr_2B_2$. *Inorg. Chem.* **55**, 5640–5648 (2016).

114. Fokwa, B. P. T., Von Appen, J. & Dronskowski, R. Synthesis of a missing structural link: The first trigonal planar B 4 units in the novel complex boride Ti1+xOs 2-xRuB2 (x = 0.6). *Chem. Commun.* 4419–4421 (2006) doi:10.1039/b608903h.

115. Clark, R. C. & Reid, J. S. The analytical calculation of absorption in multifaceted crystals. *Acta Crystallogr. Sect. A Found. Crystallogr.* **51**, 887–897 (1995).

116. Farrugia, L. J. WinGX suite for small-molecule single-crystal crystallography. *J. Appl. Crystallogr.* **32**, 837–838 (1999).

117. Spek, A. L. Single-crystal structure validation with the program PLATON. *J. Appl. Crystallogr.* **36**, 7–13 (2003).

118. Momma, K. & Izumi, F. VESTA 3 for three-dimensional visualization of crystal, volumetric and morphology data. *J. Appl. Crystallogr.* **44**, 1272–1276 (2011).

119. Perdew, J. P., Burke, K. & Ernzerhof, M. Generalized Gradient Approximation Made Simple. *Phys. Rev. Lett.* **77**, 3865–3868 (1996).

120. Takeya, H., Shishido, T. & Takei, H. Studies on the perovskite solid solution Er(Rh, M)3By (M ≡ Pd, Pt and $0 \leq y \leq 1$). *J. Less-Common Met.* **134**, 263–273 (1987).

121. Landrum, G. A. & Dronskowski, R. The Orbital Origins of Magnetism: From Atoms to Molecules to Ferromagnetic Alloys. *Angew. Chemie Int. Ed.* **39**, 1560–1585 (2000).

122. Dronskowski, R. Itinerant ferromagnetism and antiferromagnetism from the perspective of chemical bonding. *Int. J. Quantum Chem.* **96**, 89–94 (2004).

Chapter 6: Site-preferential Substitution of Si by Cu leads to Cu-chains in the New Ternary Silicide $Ir_{4-x}CuSi_2$

*Jan P. Scheifers, Boniface P. T. Fokwa**

Abstract:

The binary Ru_4Si_3 remained the only compound in its structure type -derived from RuSi by unit cell twinning - for more than 60 years. Herein, we report the synthesis and crystal structure of the first ternary silicide in the Ru_4Si_3-type structure. According to single-crystal X-ray diffraction, Ir vacancies exist along the twin boundary. $Ir_{4-x}CuSi_2$ exhibits a distorted structure compared to Ru_4Si_3, as the larger Cu selectively replaces Si on only one of three possible sites, leading to zigzag chains with short Cu-Cu distances. Furthermore, DFT calculations show that the rigid band approximation does not apply to this structure type, but the similarities of electronic structures of the ideal binary and ternary compositions suggest that this structure type can accommodate a large variety of elemental substitutions without a significant change of its electronic structure if a similar valence electron count is maintained, hinting at a potentially rich substitutional chemistry.

Introduction:

The binary silicide Ru_4Si_3, synthesized 50 years ago, [123] is part of the series $(Ru_2Si)_p(RuSi)_q$ (with p/q = 0 , 1/2, 2/1 and ∞), the structures of which are derived from the parent CsCl-type RuSi. [124,125] Compared to RuSi, all other members of the series contain less Si. The missing Si is compensated for by the formation of twin boundaries in the unit cell, i.e. unit cell twinning, which is also an instance of chemical twinning as the twinning changes the composition. The smaller p/q, the larger the twin domains with CsCl-structure are. This type of structure-composition relation has been found not only for silicides but for many compounds including germanides and others. [126]

Here, we report the existence and the single crystal structure of $Ir_{4-x}CuSi_2$ (x = 0.161(4)), the second silicide and first ternary compound in the Ru_4Si_3-type structure. To the best of our knowledge, there is only one other silicide, $CeCu_{1.78}Ir_{0.22}Si_2$, reported that contains both Cu and Ir, but it is a quaternary solid solution in the $ThCr_2Si_2$-type structure (Cu and Ir are mixed on the Cr site). [127] There are many other ternary iridium silicides, but most of them contain early transition metal (groups III to V), alkaline-earth metals or rare-earth elements. The three ternary Iridium silicides containing late-transition metals are MnIrSi (TiNiSi-type, *Pnma*) [128], Mn_3IrSi ($AlAu_4$-type, $P2_13$), [129] and a solid solution of Fe and Ir in the FeSi-type structure. [130]

In the new $Ir_{4-x}CuSi_2$, we observe Ir vacancies located at the twin boundaries and a highly unusual substitution, where one of the Si atoms - a main group metalloid - is selectively replaced by the transition metal Cu. We show how this substitution affects the electronic structure using density functional theory (DFT) calculations.

Results and Discussion:

Synthesis:

The first synthesis of $Ir_{4-x}CuSi_2$ was serendipitous as we found large single crystal flakes when removing Cu flux from a mixture that was sealed in fused silica tubes. The mixture contained among other elements Ir, the Cu flux and a reducing agent, Sc, which reacted at 1573 K with the fused silica resulting in Sc_2O_3 and elemental Si.

For subsequent syntheses from the elements, we employed both an arc-furnace and a tube furnace. Three sets of samples were prepared: Two samples of $Ir_{3.84}CuSi_2$ (composition as obtained from single-crystal measurements), two samples of Ir_4CuSi_2 (theoretical composition in the absence of Ir-vacancies) and two samples with excess Cu ($Ir_{3.84}Cu_2Si_2$ and $Ir_{3.84}Cu_3Si_2$). The elemental powders were mixed in the corresponding ratios and pressed into pellets.

- One sample of the $Ir_{3.84}CuSi_2$ and Ir_4CuSi_2 were briefly arc-melted in an arc-furnace under purified Ar-atmosphere by applying a current of 15 A.
- The remaining four samples were individually sealed in fused silica tubes under vacuum and heated to 1500 K in 2 hrs (200 K/hr) in an electrical tube furnace. The dwell time was 24 hrs before cooling down to 1100 K over 72 hrs (ca. -5.6 K/hr). At 1100 K the furnace was turned off and allowed to cool to room temperature naturally.

The powder X-ray diffraction (PXRD) data of all samples contained reflections of multiple phases, as shown by the Rietveld refinement presented in the supporting information (**Figure S1**). Only samples that were heated in a tube furnace showed a set

of reflections that could be indexed with an orthorhombic unit cell with the approximate lattice parameters a = 5.26 Å, b = 3.95 Å, c = 17.60 Å, which roughly agreed with those of Ru_4Si_3 in *Pnma* (a = 5.19 Å, b = 4.02 Å, c = 17.14 Å) [123], but with a much larger c value. The arc-melted samples did not contain the anticipated phase.

All samples contained the binary silicides Ir_3Si (I4/*mcm*) [131–133] and/or Ir_3Si_2 ($P6_3/mmc$) [132–134], while the two Cu-rich samples also included a small amount of Cu (< 5 wt.-%). The excess of Cu in two of the samples increased the relative yield of the intended $Ir_{4-x}CuSi_2$ phase from 40 wt.-% to about 60 wt.-% (**Table 7**).

***Table 7**: Overview of the different synthesis conditions, the amount of $Ir_{4-x}CuSi_2$ and side phases obtained. *relative phase fraction due presence of unknown compound(s)*

Loaded composition	$Ir_{3.84}CuSi_2$	$Ir_{3.84}CuSi_2$	Ir_4CuSi_2	Ir_4CuSi_2	$Ir_{3.84}Cu_2Si_2$	$Ir_{3.84}Cu_3Si_2$
Furnace type	tube	arc	tube	arc	tube	tube
$Ir_{4-x}CuSi_2$ (wt.-%)	40(1)	-	41(1)	-	58(2)	59(2)
Ir_3Si (wt.-%)	16.5(6)	26(1)	24.7(8)	36(1)	21.5(9)	36(1)
Ir_3Si_2 (wt.-%)	43(2)	-	34(1)	-	19(2)	-
"IrSi"	-	34(1)	-	21(1)	-	-
Ir2Si	-	40(1)	-	40(1)	-	-
Cu (wt.-%)	-	-	-	-	1.6(4)	4.6(8)

Crystal structure refinement:

Multiple very thin, flake-like single crystal of $Ir_{4-x}CuSi_2$ with metallic luster was removed from Cu flux by dissolving the flux in diluted nitric acid. Its centrosymmetric space group *Pnma,* which is the same space group as for Ru_4Si_3, was obtained from systematic absence analysis of the collected reflections. The Ir atoms were identified and located

upon solving the crystal structure, while the Cu and Si atoms emerged as peaks in the difference electron density map after a few refinement cycles. The final refinement showed conspicuous peaks/holes in the difference electron density map (close to the Ir positions). We initially suspected the single crystal to be of less than ideal quality but testing several other crystals did not yield a better refinement. We were able to decrease the differences by improving the absorption correction, which could indicate that the reason for differences in the electron density map is the absorption of the heavy Ir atoms. An alternative explanation could be that $Ir_{4-x}CuSi_2$ exhibits systematic defects of varying twin domain thickness. A TEM study on Ru_4Si_3 found systematic defects, where the size of the twin domains varies depending on how many CsCl building blocks are stacked in each domain. [135] A previous Rietveld refinement study on Ru_4Si_3 found a Ru deficiency which was attributed to roughly 10% Ru vacancies on all four available Ru sites resulting in the chemical formula $Ru_{4-x}Si_3$ with $x = 0.29$. [136] Thus, one may expect to find a similar situation in the new isotypic ternary phase. Indeed, refinement of the Ir sites also indicates the presence of vacancies, but these Ir vacancies are exclusively located at the twin boundary (Ir3). The refined chemical formula therefore is $Ir_{4-x}CuSi_2$ with $x = 0.160(4)$. The presence of all three elements and the Ir deficiency have been confirmed by semi-quantitative EDX analysis (**Figure S2**). The final refinement results are given in **Tables 8 and 9**.

***Table 8**: Results of the single-crystal refinement of the new ternary silicide $Ir_{4-x}CuSi_2$.*

Chemical formula	$Ir_{3.840(4)}CuSi_2$
Formula weight [g/mol]	857.77
Crystal system, space group	orthorhombic, *Pnma*, no. 62
Lattice parameters	a = 5.3165(5) Å b = 4.0017(5) c = 17.842(2) Å α = β = γ = 90°
Volume [Å^3], Z	379.60(8), 4
Density [Mg/m^3]	15.009
Absorption coefficient [mm^{-1}]	140.047
F(000)	1411
Crystal size [mm^3]	0.189 x 0.161 x 0.021
Θ range [°]	3.999 to 33.292
Index ranges	$-7 \leq h \leq 7$, $-6 \leq k \leq 5$, $-26 \leq l \leq 26$
Reflections (collected / independent / R(int))	4839 / 797 / 0.0992
data/restraints/parameters	797 / 0 / 45
Goodness-of-fit on F^2	1.071
Final R indices (I >2sigma(I))	$R1$ = 0.0436, $wR2$ = 0.0933
R indices (all data)	$R1$ = 0.0569, $wR2$ = 0.1008
Extinction coefficient	0.00074(10)
Largest diff. Peak / hole [e$^-$/Å^3]	5.001 / -6.129

***Table 9**: Wyckoff sites, fractional coordinates, occupancies and equivalent displacement parameters for all atoms in $Ir_{4-x}CuSi_2$ as obtained from single-crystal X-ray diffraction.*

atom	Wyckoff site	*x*	*y*	*z*	Occupancy [%]	U_{eq} [Å²]
Ir1	*4c*	0.1271(1)	¼	0.4537(1)	100	0.009(1)
Ir2	*4c*	0.2823(1)	¼	0.1725(1)	100	0.010(1)
Ir3	*4c*	0.4145(1)	¼	0.7680(1)	84.0(4)	0.010(1)
Ir4	*4c*	0.5634(1)	¼	0.6157(1)	100	0.010(1)
Si1	*4c*	0.089(1)	¼	0.5944(4)	100	0.008(1)
Si2	*4c*	0.315(1)	¼	0.3143(4)	100	0.010(1)
Cu1	*4c*	0.1234(4)	¼	0.0291(2)	100	0.009(1)

Structure Analysis:

The crystal structure of $Ir_{4-x}CuSi_2$ is a distorted variant of the Ru_4Si_3-type structure, as indicated by the distorted cubes around Cu and Si atoms (**Figure 22, left**. The Ru_4Si_3-type structure is related to the CsCl-type RuSi by unit cell twinning. The twin boundaries, which coincide with the *a*-glide planes at z = ¼ and z = ¾ exist in the structure of the new ternary phase as well. The twin domains in-between are slabs of CsCl-type structure with the face of the distorted Ir-cubes ({100}-planes of CsCl) approximately parallel to the (-3 0 13) plane in $Ir_{4-x}CuSi_2$. Thus, the orientation of the twin domains differs by 74.5° around [010] **(Figure 22, right)**. The axis of rotation corresponds to <110> of the underlying Cs-Cl-type structure. The Ir-cubes of each domain are filled with Si and Cu, where Cu occupies the distorted Ir-cubes in the center of each twin domain, while Si occupies the Ir-cubes closer to the twin boundaries. The substitution of Si by Cu is rather

unusual for silicides and intermetallics in general, as a metalloid is replaced by a late transition metal, which are chemically drastically different. In the next paragraphs, we will first analyze how this substitution affects the structure before looking at its influence on the electronic structure.

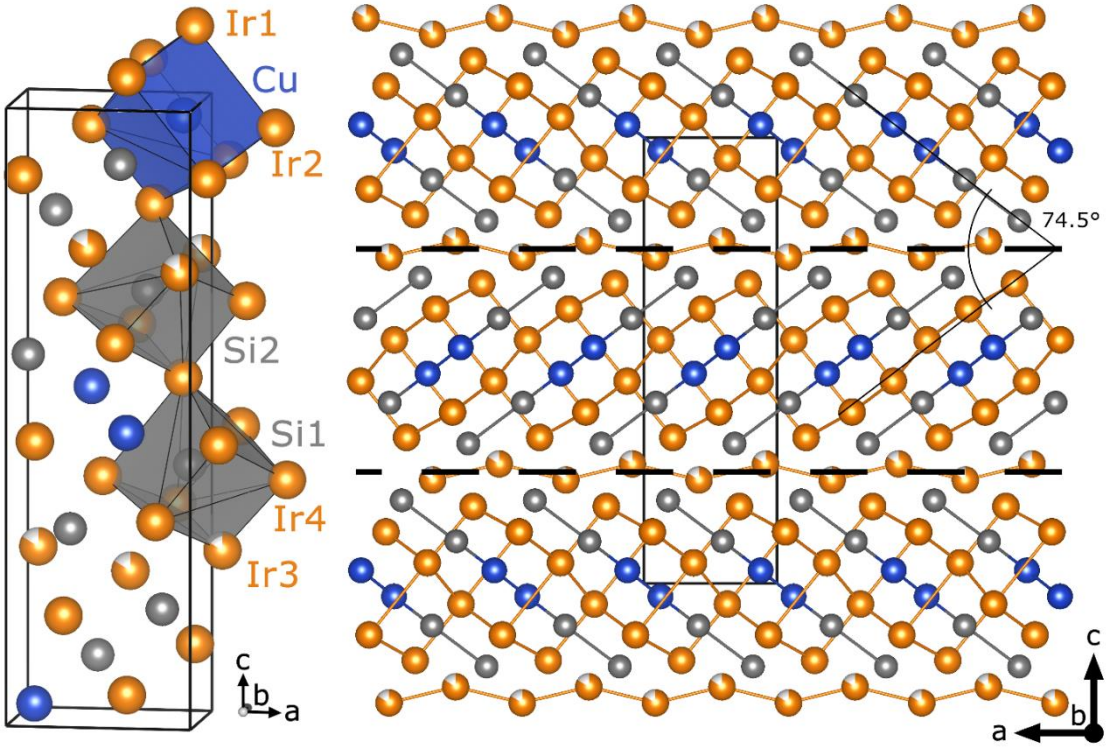

Figure 23: *Perspective view of the unit cell of $Ir_{4-x}CuSi_2$ (left). Iridium atoms are orange, silicone atoms gray and copper atoms blue trough-out the manuscript. Projection of the crystal structure along (010) emphasizing the twin boundaries (a-glide plane indicated by dashed line).*

In the CsCl-type structure, anions and cations form two alternating 4^4-square nets ((100)-planes). Due to the unit cell twinning we find ribbons of a distorted 4^4 Ir-net alternating with ribbons of a distorted 4^4 $CuSi_2$-net instead. The central Cu atoms line up in a zigzag chain along the *b*-direction with Cu-Cu distance of 2.608(4) Å (Cu-Cu-Cu angle is 100.2(2) deg). The Cu-Cu distance is slightly larger than in elemental Cu (2.55 Å) [137] or in $Cu_2Ir_4B_3$ (2.46 Å) [138]. This, however, is expected since the Cu-Cu contact

in $Ir_{4-x}CuSi_2$ is through a face of the distorted Ir-cubes (second coordination sphere), while Cu is part of the first coordination polyhedron in Cu and in $Cu_2Ir_4B_3$. Zigzag chains of copper have been observed in many coordination polymers, metalorganic compounds or ionic compounds (e.g. $SrCuO_2$) [139], but these compounds contain copper cations, so they do not compare.

The metallic radius of Cu is about 23% larger than the radius of Si (1.35 Å and 1.10 Å, respectively after Slater 1964[140]), which causes a severe distortion of the CsCl motif in $Ir_{4-x}CuSi_2$ compared to Ru_4Si_3, more so because Cu replaces only one out of three Si sites. Consequently, the distorted Ir-cube surrounding Cu is about 16% larger by volume than the Ir cubes surrounding the silicon atoms. The Cu-Ir distances range from 2.603(3) Å to 2.751(2) Å with an average of 2.698 Å. This is almost identical to the Cu-Ir distance of 2.696 Å in $Cu_2Ir_4B_3$ [138]. The Ir-Si1 distances fall in the range of 2.461(2) Å to 2.819(2) Å with an average Ir-Si1 distance of 2.563 Å, while the Ir-Si2 distances are between 2.445(3) Å and 2.844(2) Å, leading to a 0.4 % shorter average than the Ir-Si1 distance. The Ir-Si distances in Ir_2Si [132,133], which is also based on the CsCl-type structure like Ru_4Si_3, are between 2.479 Å and 2.815 Å with an average of 2.555 Å, which is in the

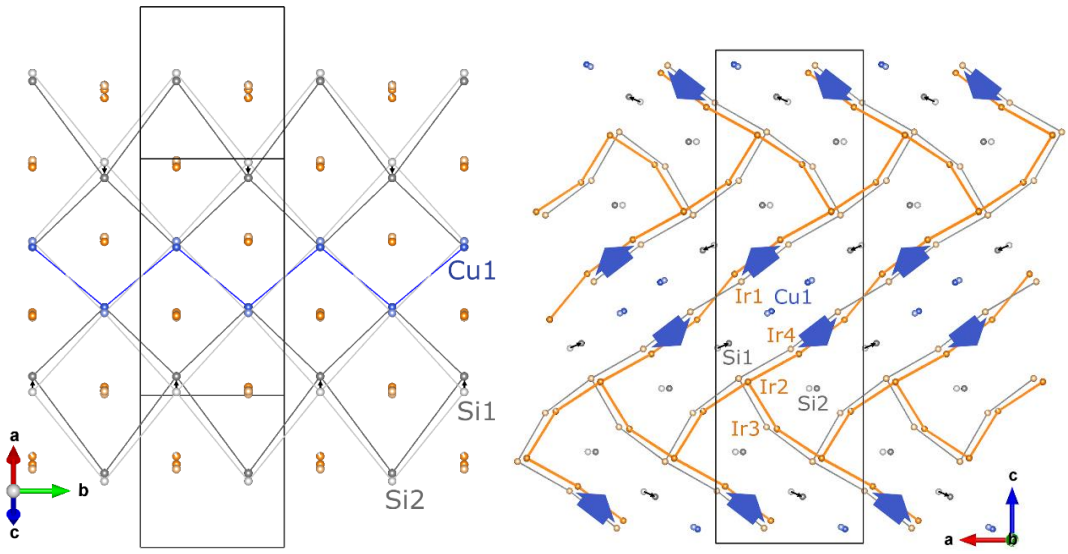

***Figure 24**: Projected crystal structure of $Ir_{4-x}CuSi_2$ with overlaid Ru_4Si_3. (Left) top-down view highlighting a $CuSi_2$-ribbon. (Right) Projection along the (010)-direction emphasizing the Ir- and Ru-networks. The pale atoms represent Ru_4Si_3, the more intensely colored atoms represent $Ir_{4-x}CuSi_2$. Black arrows indicate the shift of Si1 towards the Cu-atoms, while blue arrows indicate the spread of the Ir-atoms away from the Cu-atoms.*

same range as in $Ir_{4-x}CuSi_2$. Therefore, it can be summarized that the interatomic distances in $Ir_{4-x}CuSi_2$ are in excellent agreement with known Cu-Ir and Ir-Si compounds. By overlying the parent Ru_4Si_3 with the new ternary $Ir_{4-x}CuSi_2$, it becomes obvious that the Cu atoms, which are at the center of each twin domain barely shift compared to the respective Si atoms in Ru_4Si_3, while the Ir1 atoms are shifted away from the Cu atom. Thus, the Ir ribbons in between the Si-Cu-ribbons are severely buckled. Furthermore, the Si atoms shift closer to the central Cu atoms in each twin domain due to the increased distance between the Ir1 and Ir4 atoms. This observation is conclusive as an expansion in one direction (Ir1-Ir4 distance between ribbons) causes a contraction in a perpendicular direction (Cu-Si1 distance within a ribbon). Interestingly the Cu-Cu distance is shorter (both relative and absolute) than the distance of the corresponding Si-atoms in Ru_4Si_3

despite the larger radius of Cu and the larger lattice parameters of $Ir_{4-x}CuSi_2$. The shift of Si1 towards the center of the twin domain does not cause the $CuSi_2$-ribbon to buckle but it is distorted in-plane with the Si1-Si2 distance being 20% longer than the Cu-Si1 distance and about 30% longer than the Cu-Cu distance even though the larger Cu is not part of this bond.

Overall, the larger Cu-atoms cause an anisotropic distortion of their coordination environment with increased distances in one direction and shorter distances in the perpendicular direction.

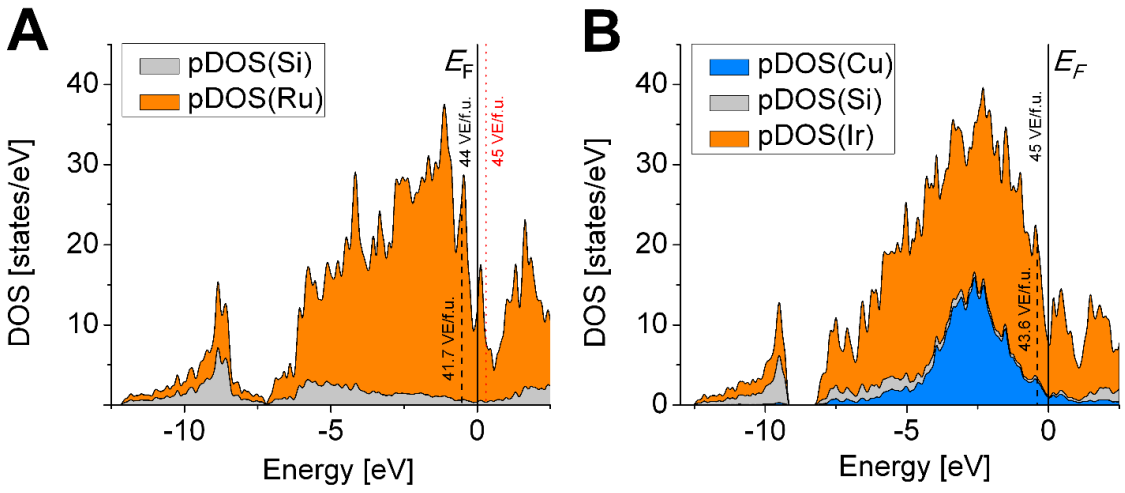

***Figure 25**. Density of states of (A) Ru_4Si_3 and (B) Ir_4CuSi_2. The contributions of each element to the total DOS are indicated by the differently colored areas. EF represents the Fermi level. Dotted lines represent the predicted Fermi levels assuming the rigid band approximation model.*

We have calculated the density of states for both Ru_4Si_3 and Ir_4CuSi_2. For both compounds we observe a peak in the DOS at around -9 eV with a major contribution from Si states. In the DOS of Ru_4Si_3 (**Figure 24, left**) a deep broad pseudo-gap can be found in the range from -8 to -6 eV. In contrast, Ir_4CuSi_2's DOS (**Figure 24, right**) exhibits an actual narrow gap in the DOS at -8 eV. Between -6 and 0 eV both compounds

feature a high density of states, which mainly corresponds to the d-states of the metal atoms. In particular, the states of copper are almost evenly distributed around -2.5 eV. The contribution of Si to the DOS in this range is small and does not fluctuate much. The Fermi level for both compounds lies in a narrow pseudo-gap at the upper limit of the d-bands with only a small contribution of Si and Cu, respectively. Considering that a late transition metal has substituted a group-XIV metalloid, the DOS of both compounds appear very similar. Also, the valence electron (VE) count for Ir_4CuSi_2 (45 e^-/f.u.) is greater by an electron than that of Ru_4Si_3 (44 e^-/f.u), if we consider only open subshells. This means that the rigid band model (RBM) is not valid here since the Fermi level lies in the same narrow pseudo-gap in both cases despite the VE count being different. The RBM would wrongly predict the Fermi level of the ternary phase using the binary's DOS (**Figure 24, left, red dotted line**). Furthermore, if the RBM would apply here, the Fermi-level would fall on a small peak in the DOS (**Figure 24, right, blue dotted line**), which is commonly associated with an electronic instability, since the valence electron count of the experimental $Ir_{3.84(4)}CuSi_2$ (43.6 e^-/f.u.) is 1.4 e^- less than the VE count of the ideal Ir_4CuSi_2 (used for the calculations) This, however, is contradicting the experimental finding that $Ir_{3.84(4)}CuSi_2$ forms at low temperatures but not when arc-melted. The same situation is observed in the DOS of the binary system where the experimentally reported $Ru_{3.71}Si_3$, (41.7 e^-/f.u.) would have its Fermi level predicted to be closer to a peak (Figure 3A), too. Consequently, it would be erroneous to apply the rigid band approximation in this structure type. Nevertheless, the similarities of electronic structures of the ideal binary and ternary compositions suggest that the Ru_4Si_3-type structure can accommodate

a large variety of elemental substitutions without a significant change of its electronic structure as long as a similar VE count is maintained, hinting at a potentially rich substitutional chemistry, especially because strong structural distortions are possible.

Conclusion

We have synthesized the first ternary compound in the Ir-Cu-Si system from the elements in a high-temperature reaction. The structure of $Ir_{4-x}CuSi_2$ is a substitutional variant of the Ru_4Si_3-type structure and only the second compound reported in the Ru_4Si_3-type structure. The incorporation of the larger Cu atoms causes a distortion of the CsCl-type related slabs. The unusual substitution of the small metalloid Si by the larger late transition metal Cu is possible because the *3d*-states of copper only weakly affect the electronic structure, according to DFT calculations.

Experimental Section:

The resulting bulk samples were crushed, and powder diffraction data were collected on a RIKAGU MiniFlex 600 benchtop diffractometer equipped with a graphite monochromator and a scintillation counter (SC-70) detector utilizing Cu-K_α radiation (λ = 1.543 Å). We indexed the obtained powder diffraction patterns and carried out a full-matrix least-squares Rietveld refinement as implemented in the FullProf suite 2017 [72,73]. The powder X-ray diffraction pattern and the refined fit were plotted using WinPLOTR [74].

Using a RIGAKU XtalLAB mini benchtop diffractometer equipped with a graphite monochromator and SHINE optics with Mo-anode (λ_{Mo} = 0.71073 Å), we collected single-crystal data on a thin, shiny flake-like crystal. The intensities were corrected via an analytical numeric absorption correction [115]. The crystal structure solution was obtained using direct methods in SHELXS and refinement (full matrix least squares on F^2) was performed with SHELXL as implemented in the SHELX-2008 software suite [56]. The subroutines ADDSYM and STRUCTURE TIDY of the PLATON software implemented in WinGX 2014.1 [75,141,117] were executed standardizing the crystal structure data.

The composition of the single crystal was analyzed by energy dispersive X-ray spectroscopy (EDX) using the ultra-high-resolution low-energy system Nova NanoSEM450 equipped with a 50mm^2 X-Max50 SD EDX detector.

The Vienna *ab-initio* simulation package (VASP) [77,78] in conjunction with the projector augmented wave (PAW) method of Blöchl [60,142] was employed to calculate the electronic structure of Ir_4CuSi_2 and Ru_4Si_3. The generalized gradient approximation (GGA) was used for all calculations and the Perdew-Burke-Enzerhoff (PBE) functional was used to handle exchange and correlations [119]. The k-point grid was generated with the Monkhorst package [79]. For the calculations, we assumed the site of Ir2 to be fully occupied to simplify the structural model. An initial structure relaxation was performed before calculating the electronic structures (cut-off energy 500 eV) and the Fermi-level E_F was set to 0 eV.

Acknowledgements

The authors would like to acknowledge the financial support by UC Riverside (Dissertation Year Award for J.P.S and start-up funding for B.P.T.F). Furthermore, the authors thank Sarah Hoang, Alexis Puente, Nicole Zuno and Kellie Albright, who are students of the Valley View Highschool in Moreno Valley, CA, for their help preparing the samples and sealing them in quartz tubes. Finally, the authors acknowledge the support by the San Diego Supercomputing Center, where the DFT calculations were carried out.

References

56. Sheldrick, G. M. A short history of SHELX. *Acta Crystallogr. Sect. A Found. Crystallogr.* **64**, 112–122 (2008).

60. Blöchl, P. E. Projector augmented-wave method. *Phys. Rev. B* **50**, 17953–17979 (1994).

72. Rodriguez-Carvajal, J. FullProf: A Program for Rietveld Refinement and Profile Matching Analysis of Complex Powder Diffraction Patterns. in *Satellite Meeting on Powder Diffraction of the XV Congress of the IUCr* 127 (1990).

73. Rodríguez-Carvajal, J. Recent advances in magnetic structure determination by neutron powder diffraction. *Phys. B Condens. Matter* **192**, 55–69 (1993).

74. Roisnel, T. & Rodriguez-Carvajal, J. WinPLOTR: a Windows tool for powder diffraction patterns analysis. in *Materials Science Forum, Proceedings of the Seventh European Powder Diffraction Conference (EPDIC 7)* (eds. Delhez, R. & Mittenmeijer, E. J.) 118–123 (2000).

75. Farrugia, L. J. WinGX suite for small-molecule single-crystal crystallography. *J. Appl. Crystallogr.* **32**, 837–838 (1999).

77. Kresse, G. Vienna ab initio simulation package. (1999).

78. Kresse, G. & Hafner, J. Ab initio molecular dynamics for liquid metals. *Phys. Rev. B* **47**, 558–561 (1993).

79. Monkhorst, H. J. & Pack, J. D. Special points for Brillouin-zone integrations. *Phys. Rev. B* **13**, 5188–5192 (1976).

115. Clark, R. C. & Reid, J. S. The analytical calculation of absorption in multifaceted crystals. *Acta Crystallogr. Sect. A Found. Crystallogr.* **51**, 887–897 (1995).

117. Spek, A. L. Single-crystal structure validation with the program PLATON. *J. Appl. Crystallogr.* **36**, 7–13 (2003).

119. Perdew, J. P., Burke, K. & Ernzerhof, M. Generalized Gradient Approximation Made Simple. *Phys. Rev. Lett.* **77**, 3865–3868 (1996).

123. Engstroem, I. & Johnsson, T. The crystal structure of Ru4Si3. *Ark. foer Kemi* **30**, 141–147 (1968).

124. Andersson, S. & Hyde, B. G. Twinning on the unit cell level as a structure-building operation in the solid state. *J. Solid State Chem.* (1974) doi:10.1016/0022-4596(74)90059-0.

125. Hyde, B. G., Andersson, S., Bakker, M., Plug, C. M. & O'Keeffe, M. The (twin) composition plane as an extended defect and structure-building entity in crystals. *Progress in Solid State Chemistry* (1979) doi:10.1016/0079-6786(79)90002-5.

126. Parthé, E. *Modern Perspectives in Inorganic Crystal Chemistry*. (Springer Netherlands, 1992).

127. Mielke, A., Rieger, J. J., Scheidt, E. W. & Stewart, G. R. Important role of coherence for the heavy-fermion state in CeCu2Si2. *Phys. Rev. B* **49**, 10051–10053 (1994).

128. Eriksson, T. *et al.* Cycloidal magnetic order in the compound IrMnSi. *Phys. Rev. B* **71**, 174420 (2005).

129. Eriksson, T. *et al.* Crystal and magnetic structure of Mn3IrSi. *Phys. Rev. B - Condens. Matter Mater. Phys.* **69**, (2004).

130. Sales, B. C. *et al.* Magnetic, transport, and structural properties of Fe1-xIrxSi. *Phys. Rev. B* **50**, 8207–8213 (1994).

131. Kimmel, G. On the U3Si (Doc) crystallographic type. *J. Less Common Met.* **59**, P83–P86 (1978).

132. Bhan, S. & Schubert, K. Zum Aufbau der Systeme Kobalt-Germanium, Rhodium-Silizium sowie einiger verwandter Legierungen. *ZEITSCHRIFT FUR Met.* **51**, 327–339 (1960).

133. Schubert, K. *et al.* Einige strukturelle Ergebnisse an metallischen Phasen (5). *Naturwissenschaften* **47**, 303–303 (1960).

134. Finnie, L. N. Structures and compositions of the silicides of ruthenium, osmium, rhodium and iridium. *J. Less Common Met.* **4**, 24–34 (1962).

135. Andersson, S., Leygraf, C. & Johnsson, T. The structure of defect Ru4Si3. *J. Solid State Chem.* **14**, 78–84 (1975).

136. Weitzer, F., Rogl, P. & Schuster, J. C. X-ray investigations in the systems ruthenium-silicon and ruthenium-silicon-nitrogen. *Zeitschrift fuer Met.* **79**, 154–156 (1988).

137. Straumanis, M. E. & Yu, L. S. Lattice parameters, densities, expansion coefficients and perfection of structure of Cu and of Cu–In α phase. *Acta Crystallogr. Sect. A* **25**, 676–682 (1969).

138. Klünter, W. & Jung, W. Das Kupfer-Iridiumborid Cu2Ir4B3 mit einer vom ZnIr4B3-Typ abgeleiteten Schichtstruktur. *Zeitschrift für Anorg. und Allg. Chemie* **626**, 502–505 (2000).

139. Weller, M. T. & Lines, D. R. Structure and oxidation state relationships in ternary copper oxides. *J. Solid State Chem.* **82**, 21–29 (1989).

140. Slater, J. C. Atomic Radii in Crystals. *J. Chem. Phys.* **41**, 3199–3204 (1964).

141. Farrugia, L. J. WinGX and ORTEP for Windows: An update. *J. Appl. Crystallogr.* **45**, 849–854 (2012).

142. Kresse, G. & Joubert, D. From ultrasoft pseudopotentials to the projector augmented-wave method. *Phys. Rev. B* **59**, 1758–1775 (1999).

Chapter 7: $Fe_5Ge_2Te_2$ and the series $(Fe_2Ge)_n(FeTe_2)$

Introduction:

Layered van der Waals (vdW) materials have attracted a great deal of interest since the discovery of graphene through exfoliation of graphite. [143,144] The prospect of realizing nanoscale spintronic devices constructed from atomically thin 2D ferromagnetic (FM) materials through combination of large spin polarization and high Curie temperature (T_C) has propelled these materials to a high level of interest in the scientific community. The first intrinsically 2D FM materials were realized from exfoliation of the FM CrI_3 (insulator with bulk $T_C = 61$ K) [29], FM $Cr_2Ge_2Te_6$ (insulator with bulk $T_C = 60$ K) [34], and recently FM VI_3 (semiconductor with bulk $T_C = 50$ K) [145]. However, T_C of these materials remains somewhat low for spintronic applications, thus creating new challenges for both experimentalists and theoreticians to search for new 2D intrinsic ferromagnets with much higher T_C. In contrast, itinerant FM vdW $Fe_{3-x}GeTe_2$ (FGT), discovered in 2006 by Deiseroth *et al.* [146,147], has a high T_C ranging from 150 to 220 K (depending on Fe vacancy x) [148] and thus has recently attracted the attention of the scientific community.

Herein, we present the crystal structure of $Fe_{5-x}Ge_2Te_2$, which turned out to be the second member of the new series $(Fe_{2-x}Ge)_n(FeTe_2)$.

Experimental:

Hexagonal plate-like crystals were selected under a light microscope for single crystal X-ray diffraction. The data was collected with a RIGAKU XtalLAB mini bench-top diffractometer equipped with a graphite monochromator and SHINE optics using Mo-radiation (λ_{Mo} = 0.71073 Å). The intensities were corrected according to an analytical numeric absorption correction [115]. The structure solution and refinement (full matrix least square on F^2) were performed using the SHELX-2008 software suite [57,149]. The structure was solved using direct methods in SHELXS and the refinement was done using SHELXL. ADDSYM and STRUCTURE TIDY subroutines of the PLATON software implemented in WinGX 2014.1 were carried out to verify and standardize the crystal structure data [76,116,117]. The obtained single crystal structure was confirmed using X-ray powder diffraction. The powder diffraction data was collected from 5 to 90 ° 2Θ with a RIKAGU MiniFlex 600 benchtop diffractometer using Cu-K_α radiation (λ = 1.543 Å) in reflection geometry, which is equipped with a graphite monochromator and scintillation counter (SC-70) detector. We carried a full-matrix least-squares based Rietveld refinement as implemented in the FullProf suite 2017 [55,150] and the powder X-ray diffraction patter was plotted together with the obtained fit using WinPLOTR [74]. For the refinement of the highly anisotropic $Fe_{4.84(2)}Ge_{1.96(2)}Te_2$, we took preferred orientation and presence of $Fe_{2-x}Ge$ and $Fe_{3-x}GeTe_2$ (both *$P6_3/mmc$*) into account

.

Results:

We determined the trigonal space group $P\bar{3}m1$ (no. 164) to be correct. The lattice parameters are $a = b = 4.0121(3)$ Å and $c = 10.7777(8)$ Å (see **Table 11**). In contrast to other layered tellurides [151] we do not observe severe stacking disorder along [001], but we do observe significant disorder on three different sites (see **Figure 25**).

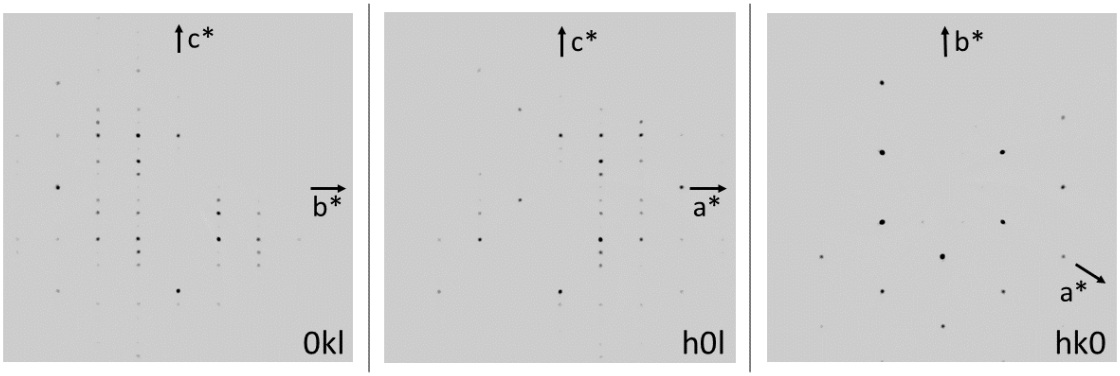

***Figure 26**: Diffraction patterns of the three fundamental planes 0kl, h0l and hk0 of $Fe_{4.84(2)}Ge_{1.96(2)}Te_2$ do not indicate stacking faults.*

First, we find significant electron density at Wyckoff site *1b* (0,0,1/2) indicating a partially occupied site. It corresponds to an additional Fe-site (Fe3) with an occupancy of 16(1) %. Second, refining the occupancy of Fe1 (site *2d*) results in an occupancy of only 84(1) %. Third, we observe enlarged anisotropic displacement parameters (ADP) for Ge in a preliminary solution refining. However, efforts to improve the solution by refining the occupancy only resulted in a small improvement of the ADPs while the occupancy is 98.6%. Additionally, small peaks in the electron density map are observed ca. 0.6 Å from Ge.

Table 10: *Details on the crystal data and structure refinement for* $Fe_{4.84(2)}Ge_{1.96(2)}Te_2$.

Empirical formula	$Fe_{4.84(2)}Ge_{1.96(2)}Te_2$
Formula weight [g/mol]	669.89
Wavelength [Å]	0.71073
Crystal system	Trigonal
Space group, number	$P\bar{3}m1$, 164
Unit cell dimensions	a = 4.0121(3) Å α = 90° b = 4.0121(3) Å β = 90° c = 10.7777(8) Å γ = 120°
Volume [$Å^3$]	150.25(3)
Z	2
Density (calculated) [Mg/m3]	15.023
Absorption coefficient [mm^{-1}]	61.939
F(000)	596
Theta range for data collection [°]	3.781 to 33.692
Index ranges	$-5 \leq h \leq 5$, $-6 \leq k \leq 3$, $-16 \leq l \leq 15$
Reflections collected	1357
Independent reflections	268 [R(int) = 0.0365]
Completeness to theta = 25.242°	99.3 %
Refinement method	Full-matrix least-squares on F^2
Data / restraints / parameters	268 / 0 / 21
Goodness-of-fit on F^2	1.069
Final R indices [I>2σ(I)]	R1 = 0.0346, wR2 = 0.0855
R indices (all data)	R1 = 0.0427, wR2 = 0.0912
Extinction coefficient	0.004(3)
Largest diff. peak and hole [$e/Å^{-3}$]	3.239 and -2.993

Introducing a triply split site for Ge (site *6i*) resulted in improved R-values, decreased ADPs and eliminated the peaks in the electron density. The occupancy of the split site is refined as 32.7(3) %, which is close to the ideal 33.3% (see **Table 13**). All other sites are fully occupied within the margin of error. Thus, the overall chemical formula is $Fe_{4.84(2)}Ge_{1.96(2)}Te_2$ with R-values of $R_{obs} = 0.035$ and $R_{all} = 0.043$ EDX. The Wyckoff sequence is *164,id²cba* indicating a new structure type (see **Table 12**).

***Table 11**: Atomic coordinates and equivalent isotropic displacement parameters (Å²). $U_{(eq)}$ is defined as one third of the trace of the orthogonalized U^{ij} tensor.*

Atom	Wyckoff site	x	y	z	sof [%]	$U_{(eq)}$
Ge	*6i*	0.3571(6)	0.714(1)	0.1095(1)	32.7(3)	0.011(1)
Fe1	*2d*	0.66667	0.33333	0.1283(2)	84(1)	0.012(1)
Te	*2d*	0.66667	0.33333	0.3661(1)	100	0.012(1)
Fe2	*1c*	0	0	0.2391(2)	100	0.012(1)
Fe3	*1b*	0	0	0.5	16(1)	0.010(4)
Fe4	*1a*	0	0	0	100	0.011(1)

***Table 12:** Anisotropic displacement parameters (Å²x 10³) for $Fe_{4.84(2)}Ge_{1.96(2)}Te_2$. The anisotropic displacement factor exponent takes the form: $-2\pi^2[h^2a^{*2}U^{11} + ... + 2\ h\ k\ a^*\ b^*\ U^{12}]$. [a] refined isotropically*

Atom	U^{11}	U^{22}	U^{33}	U^{23}	U^{13}	U^{12}
Ge[a]	-	-	-	-	-	-
Fe1	12(1)	12(1)	11(1)	0	0	6(1)
Te	13(1)	13(1)	11(1)	0	0	6(1)
Fe2	11(1)	11(1)	12(1)	0	0	6(1)
Fe3	10(5)	10(5)	10(7)	0	0	5(3)
Fe4	10(1)	10(1)	12(1)	0	0	5(1)

The Rietveld refinement confirmed the single crystal structure (see **Figure 26**). The sample contains 88(2) wt.-% $Fe_{4.84(2)}Ge_{1.96(2)}Te_2$, 6.8(3) wt.-% $Fe_{2-x}Ge$ and 4.3(4) wt.-% $Fe_{3-x}GeTe_2$. The refined lattice parameters of $Fe_{4.84(2)}Ge_{1.96(2)}Te_2$ are $a = b = 4.002(3)$ Å and $c = 10.7699(8)$ Å and the occupancies of Ge1 and Fe1 are in good agreement with the single crystal structure solution. However, the occupancy of the Fe3 site found in the refinement is slightly higher than expected. The R-values $R_{Bragg} = 6.86$ and $R_f = 4.83$ indicate the good quality of the refinement.

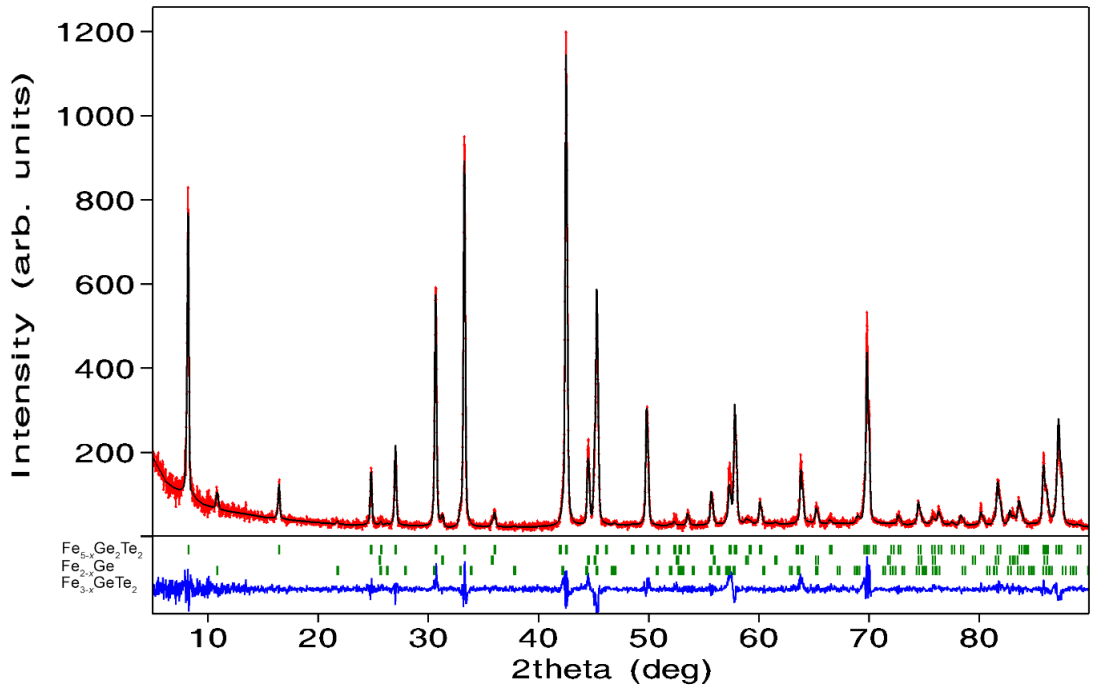

Figure 27: *Comparison of powder X-ray diffraction data (red) with the fit obteind by Rietveld refinement (black). The difference (blue) and the reflection positions (green) of $Fe_{5-x}Ge_2Te_2$, $Fe_{2-x}Ge$ and $Fe_{3-x}GeTe_2$ (top to bottom) are indicated.*

Discussion:

The new structure is built from slabs stacked along [001] (see **Figure 27**) and separated by a Van-der-Waals gap (VdW gap) of 2.886(2) Å. The VdW gap is slightly larger than for comparable tellurides such as $NiTe_2$, where the VdW gap is about 2.6 Å [152]. Each slab consists of seven layers. Three {3,6}-layers of Fe (B, B' and B'') are stacked on top of each other (B with Fe2, B' with Fe4 and B'' with Fe2 again). The Fe atoms form two layers of face-sharing trigonal prisms which are alternatingly filled by Fe1 and Ge. The two layers with Fe1 and Ge are labeled C and C'. The Te-atoms reside on top of every Fe-filled prism, which results in {3,6}-layers of Te (A and A') terminating each slab. Due to the double layer of Fe-prisms and the alternate arrangement of Ge and Fe1 within the double layer, the layers A and A' of the same slab are offset to each other. This has two important consequences: (1) only a single slab is required per unit cell to achieve translational symmetry along [001] and (2) the Te-atoms of two neighboring slabs form trigonal anti-prisms and tetrahedra at the VdW gap. In the center of the trigonal anti-prisms, we find significant electron density reflecting a partially occupied atomic position at (0,0,0). The electron density accounts for 15.9% Fe6.

Examining the structure more closely reveals that the layers C and C' are not perfectly flat; that is Fe1 and Ge do not have the same *z*-coordinate. In fact, the Fe1-Ge distance is rather short (2.325 Å in average perpendicular to *c*), which is the reason for both the vacancies on the Fe1 site, the puckering of the layer and the split site for Ge, which is also observed in Fe_3Ge_2 [153]. This contrasts with $Fe_{5-\delta}GeTe_2$, where Ge is displaces along

c creating a doubly split site instead [154]. The displacement of the Fe1 atom towards the VdW gap increases the Fe1-Ge distance and shortens the Fe1-Te distance, which is even shorter than the Fe2-Te distance (2.563(3) Å and 2.691(1) Å, respectively). The short Fe1-Te distance reflects a strong bond, which explains why Te prefers to cap the Fe-filled trigonal prisms over the Ge-filled ones.

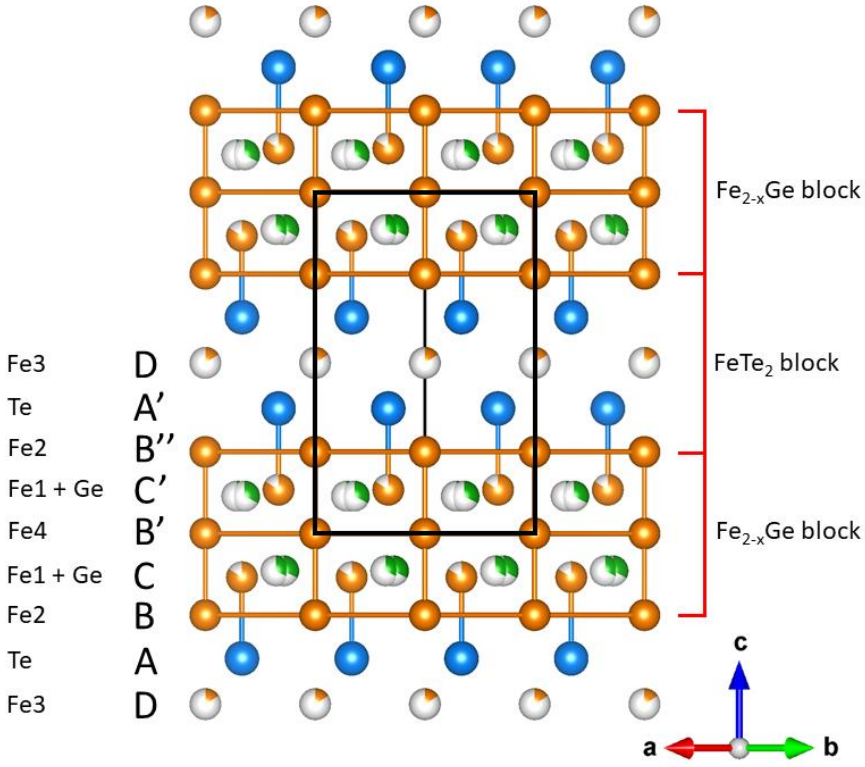

Figure 28: *crystal structure of $Fe_{5-x}Ge_2Te_2$. Fe in orange, Ge in green and Te in blue*

The structure is closely related to other layered tellurides in particular to $Fe_{3-x}GeTe_2$ [33]. In contrast to $Fe_{4.84(2)}Ge_{1.96(2)}Te_2$ $Fe_{3-x}GeTe_2$ exhibits thinner slabs with a single layer of Fe-prisms corresponding to a stacking sequence of ABCB'A'. The offset stacking of those thinner slabs and the mirror plane in the C-layer require two slabs per unit cell,

which explains the larger c lattice parameter for $Fe_{3-x}GeTe_2$ despite thinner slabs. Removing one Fe-layer and one $Fe_{1-x}Ge$-layer from $Fe_{4.84(2)}Ge_{1.96(2)}Te_2$ reduces the number of stacked trigonal prisms as well as it changes the composition. Since it is possible to incorporate two or three Fe-layers in the structure it seems natural to find analog structures with even more (or less) such layers. This results in the series $(Fe_{2-x}Ge)_n(Fe_{1+y}Te_2)_m$, where n and m are integers, $0 < x < 0.25$ and $0 < y < 1$. $Fe_{3-x}GeTe_2$ corresponds to $n = 1$ and $m = 1$, $Fe_{4.84(2)}Ge_{1.96(2)}Te_2$ has $n = 2$, $m = 1$. A hypothetical structure with the formula $Fe_{7-x}Ge_3Te_2$ would result from $n = 3$, $n = 1$ (see **Figure 28**).

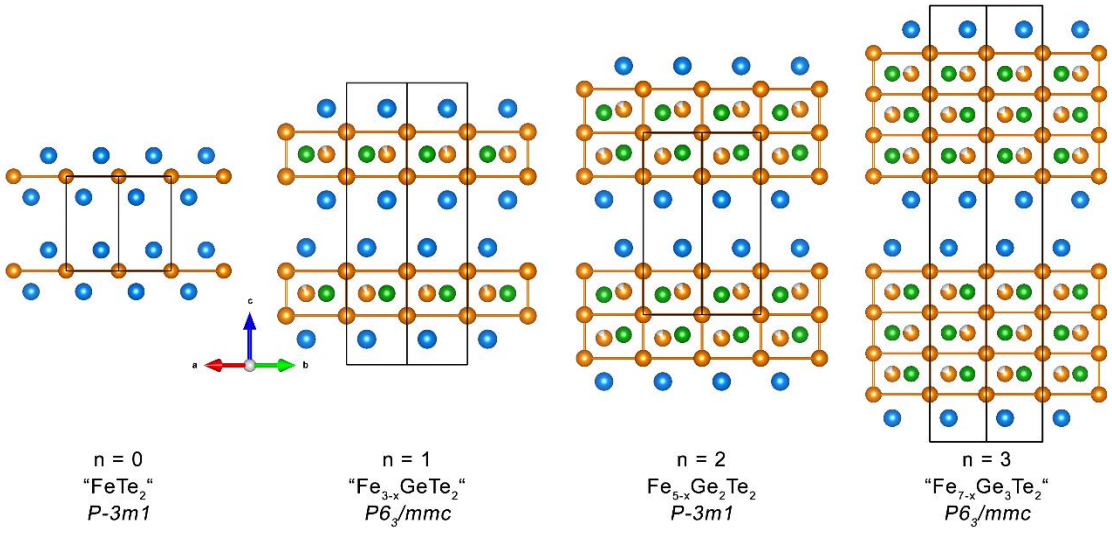

***Figure 29**: the structures of the series $(Fe_2Fe)_n(FeTe2)$.*

Another excellent known example in this series occurs for $n = 1$ and $m = 0$. $Fe_{2-x}Ge$ ($P6_3/mmc$, no 194, $Co_{1.75}Ge$-type) consists of alternating layers of Fe and $Fe_{1-x}Ge$ [155]. The a lattice parameter (4.023 Å) is slightly larger than for both $Fe_{3-x}GeTe_2$ and $Fe_{4.84(2)}Ge_{1.96(2)}Te_2$, while $c = 5.105$ Å, which corresponds to two Fe- and $Fe_{1-x}Ge$-layers each. Even the triply split site for Ge has been observed in this structure. The other end

of the series is "$Fe_{1+y}Te_2$" ($n = 0$, $m = 1$, $y = 0$) in the CdI_2-type structure ($P\bar{3}m1$, no. 164). This compound has not been observed yet and remains hypothetical. However, there is a close crystallographic relation to an already existing compound (see **Figure 29**): In the CdI_2-type structure Te would form layers of trigonal anti-prisms with every other layer of prisms being occupied by Fe, while the empty anti-prisms form the VdW gap. By including the partially occupied layer D in the VdW gap ($0 < y < 1$), the $TlCdS_2$-type structure ($P\bar{3}m1$, no 164) is obtained, where the two layers of trigonal prisms can be distinguished (in case of $TlCdS_2$ by the metal occupying the anti-prisms, in case of "$Fe_{1+y}Te_2$" with the additional D-layer by the Fe-occupancies). If the two layers cannot be distinguished and the Fe-atoms are evenly distributed, we arrive at $Fe_{1/2+y/2}Te$ (= ½ $Fe_{1+y}Te_2$) in the NiAs-type structure ($P6_3/mmc$, no. 194) [156]. If the layers A, B and D are taken into account, the composition of the "$Fe_{1+y}Te_2$" building block equals $Fe_{0.58}Te$. Thus, the Fe-deficient $Fe_{1-y}Te$ in NiAs-type structure is simply a disordered version of the member of the series $(Fe_{2-x}Ge)_n(Fe_{1+y}Te_2)_m$ where $n = 0$ and $m = 1$. An interesting detail here is the fact that the *a* lattice parameter of NiAs-type $Fe_{1-x}Te$ is only 3.816 Å and as such significantly smaller than respective lattice parameter in $Fe_{2-x}Ge$ (see above). The *a* lattice parameters of both $Fe_{3-x}GeTe_2$ and $Fe_{48.4(2)}Ge_{1.96(2)}Te_2$ lie in between and approach the lattice parameter of $Fe_{2-x}Ge$ the larger *n* is. The two structures of $Fe_{2-x}Ge$ and $Fe_{1+y}Te_2$ can easily intergrow since they share the common {3,6} Fe-layers, which form the interface between the two building blocks. From symmetry considerations we can deduce that for *n* = 'odd' two slabs per unit cell result in the high symmetry space group $P6_3/mmc$, while *n* = 'even' will give only one slab per unit cell in the space group

$P\bar{3}m1$, if $m = 1$ (see Fig.). If $n < m$, we predict blocks of disordered $Fe_{1-y}Te$ to be separated by individual layers of trigonal Fe-prisms as most of the structure belongs to the NiAs-type. However, we cannot predict whether the blocks occur in the ordered $TlCdS_2$-type or the disordered NiAs-type. Each layer of trigonal Fe-prisms adds ca. 2.6 Å to the *c* lattice parameter, while each VdW gap corresponds to approximately 5.6 Å. Thus, $c \approx 2.6\ Å \cdot n + 5.6\ Å \cdot m$ or double that, if there are two slabs in the unit cell.

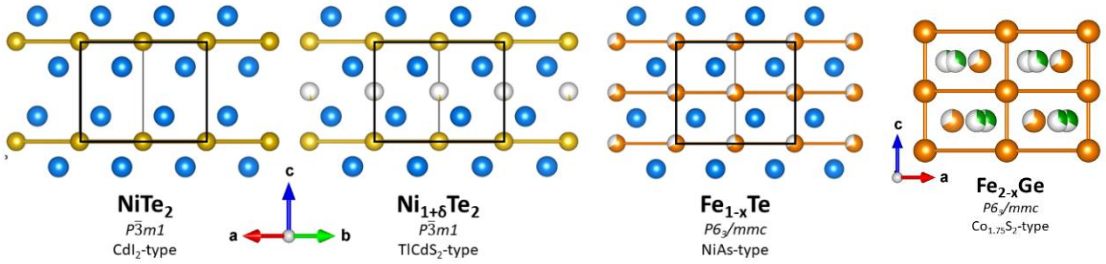

***Figure 30**: relation between ordered $NiTe_2$ (far left) and disordered FeTe (right) and Fe_2Ge (far right).*

Potentially, even more complicated stacking sequences in the series $(Fe_{2-x}Ge)_n(Fe_{1+y}Te_2)_m$ could be realized by combining any two simple stacking sequences. If $n_1 = 1$, $m_1 = 1$ is combined with $n_2 = 2$, $m_2 = 1$ the resulting $Fe_8Ge_3Te_4$ ($n_1 + n_2 = 3$, $m_1 + m_2 = 2$) has alternating single and double slabs (see **Figure 30**). In general, *n* and *m* should be divided by their greatest common divisor to avoid the description of an unnecessary superstructure.

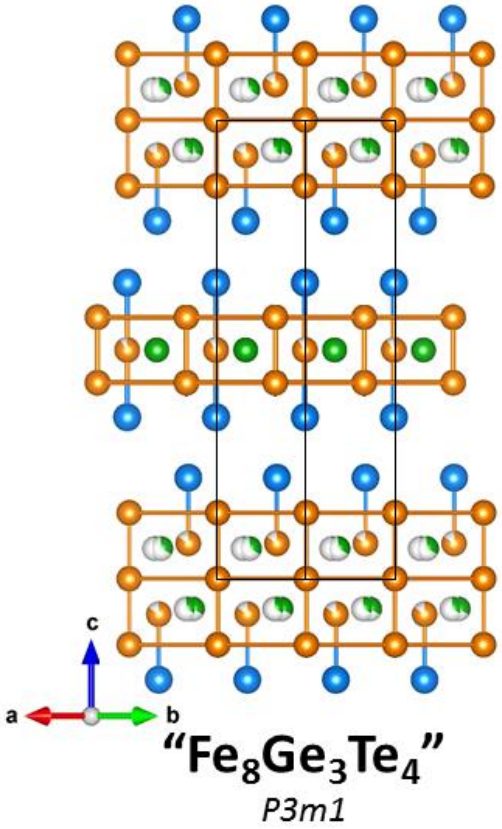

***Figure 31**: predicted structure of the hypothetical $Fe_8Ge_3Te_4$.*

Surprisingly, the recently published $Fe_{5-\delta}GeTe_2$ does not belong the series $(Fe_{2-x}Ge)_n(Fe_{1+y}Te_2)_m$ [151,154]. It contains additional {3,6} Fe-layers which is reflected in the formula $Fe_{5-\delta}GeTe_2$ = $(Fe_{2-x}Ge)_1(Fe_{1+y}Te_2)_1Fe_2$. We refrain from generalizing our current model for the series $(Fe_{2-x}Ge)_n(Fe_{1+y}Te_2)_m$ by including those additional Fe-layers since it remains to be seen if similar compounds with additional layers exist.

Despite our best efforts we have not been able to synthesize $Ni_{5-\delta}Ge_2Te_2$ yet, but the compound with $n = 1$ and $m = 1$ has already been reported in the series $(Ni_{2-x}Ge)_n(Ni_{1+y}Te_2)_m$. [33] Moreover, $Ni_{2-x}Ge$ in $Co_{1.75}S$-type structure ($n = 1$, $m = 0$) and $NiTe_2$ ($n = 0$, $m = 1$, $y = 0$) also exist. [157] In contrast to Fe, not only the disordered, metal-deficient NiAs-type has been observed for Ni and Te but the ordered $TlCdS_2$- and the ideal CdI_2-type do occur. [152,158]

Finally, we can speculate that other VdW materials could be potentially incorporated into the presented system. On the one hand it would be interesting to see how the magnetic properties are affected if the $Fe_{2-x}Ge$ blocks are further separated by other non-magnetic

blocks such as $ZrTe_2$ (also CdI_2-type) or $MoTe_2$ (*P6₃/mmc,* no. 194, MoS_2-type). [159,160] On the other hand would it be highly exciting to introduce a new property in the system. For exsample it seems not completely impossible to incorporate blocks of the topological insulator Bi_2Te_3 ($R\bar{3}m$, no. 166, Bi_2Te_3-type) [161] inbetween the $Fe_{2-x}Ge$ blocks. In this way novel 2D heterostructures could be obtained simply from crystal growth instead of complex postsynthetic assembly of primary 2D materials. A key aspect here would be the lattice parameters *a* since a mismatch could cause commensurate or even incommensurate modulation in the *ab*-plane. The *a* lattice parameter of $ZrTe_2$ is inbetween the *a* lattice parameters of $Fe_{2-x}Ge$ and $Fe_{1+y}Te$, whereas the *a* lattice parameters of $MoTe_2$ and Bi_2Te_3 are significantly smaller and larger, respectively.

References:

29. Huang, B. *et al.* Layer-dependent ferromagnetism in a van der Waals crystal down to the monolayer limit. *Nature* **546**, 270–273 (2017).

33. Deiseroth, H.-J., Aleksandrov, K., Reiner, C., Kienle, L. & Kremer, R. K. Fe3GeTe2 and Ni3GeTe2 – Two New Layered Transition-Metal Compounds: Crystal Structures, HRTEM Investigations, and Magnetic and Electrical Properties. *Eur. J. Inorg. Chem.* **2006**, 1561–1567 (2006).

34. Gong, C. *et al.* Discovery of intrinsic ferromagnetism in two-dimensional van der Waals crystals. *Nature* **546**, 265–269 (2017).

55. Rodriguez-Carvajal, J. *FULLPROF 2000: A Rietveld Refinement and Pattern Matching Analysis Program*. *Abstract of the Satellite Meeting on Powder Diffraction of the XV Congress of the IUCr, Toulouse, France* (2008).

57. Sheldrick, G. M. Crystal structure refinement with SHELXL. *Acta Crystallogr. Sect. C Struct. Chem.* **71**, 3–8 (2015).

74. Roisnel, T. & Rodriguez-Carvajal, J. WinPLOTR: a Windows tool for powder diffraction patterns analysis. in *Materials Science Forum, Proceedings of the Seventh European Powder Diffraction Conference (EPDIC 7)* (eds. Delhez, R. & Mittenmeijer, E. J.) 118–123 (2000).

76. Farrugia, L. J. WinGX and ORTEP for Windows : an update. *J. Appl. Crystallogr.* **45**, 849–854 (2012).

115. Clark, R. C. & Reid, J. S. The analytical calculation of absorption in multifaceted crystals. *Acta Crystallogr. Sect. A Found. Crystallogr.* **51**, 887–897 (1995).

116. Farrugia, L. J. WinGX suite for small-molecule single-crystal crystallography. *J. Appl. Crystallogr.* **32**, 837–838 (1999).

117. Spek, A. L. Single-crystal structure validation with the program PLATON. *J. Appl. Crystallogr.* **36**, 7–13 (2003).

143. Li, H., Ruan, S. & Zeng, Y. J. Intrinsic Van Der Waals Magnetic Materials from Bulk to the 2D Limit: New Frontiers of Spintronics. *Advanced Materials* vol. 31 (2019).

144. Gibertini, M., Koperski, M., Morpurgo, A. F. & Novoselov, K. S. Magnetic 2D materials and heterostructures. *Nature Nanotechnology* vol. 14 408–419 (2019).

145. Kong, T. *et al.* VI 3 —a New Layered Ferromagnetic Semiconductor. *Adv. Mater.* **31**, (2019).

146. Spirovski, F., Reiner, C., Deiseroth, H.-J., Kienle, L. & Mikus, H. M3GeTe2 and M5GeTe2 – new layered tellurides (M = Fe, Ni). *Zeitschrift für Anorg. und Allg. Chemie* **632**, 2103–2103 (2006).

147. Merker, H.-B., Schfer, H. & Krebs, B. Neue PdxAly-Phasen und die Verbindung Pd5AII2. *Zeitschrift fur Anorg. und Allg. Chemie* **462**, 49–56 (1980).

148. Spirovski, F., Reiner, C., Deiseroth, H.-J., Kienle, L. & Mikus, H. M3GeTe2 and M5GeTe2 – new layered tellurides (M = Fe, Ni). *Zeitschrift für Anorg. und Allg. Chemie* **632**, 2103–2103 (2006).

149. Sheldrick, G. M. A short history of SHELX. *Acta Crystallographica Section A: Foundations of Crystallography* vol. 64 112–122 (2008).

150. Rodríguez-Carvajal, J. Recent advances in magnetic structure determination by neutron powder diffraction. *Phys. B Phys. Condens. Matter* **192**, 55–69 (1993).

151. Stahl, J., Shlaen, E. & Johrendt, D. The van der Waals Ferromagnets Fe5-δGeTe2 and Fe5-δ-xNixGeTe2 - Crystal Structure, Stacking Faults, and Magnetic Properties. *Zeitschrift für Anorg. und Allg. Chemie* **644**, 1923–1929 (2018).

152. Bensch, W. *et al.* Anionic Polymeric Bonds in Nickel Ditelluride : Crystal Structure , and Experimental and Theoretical Band Structure. *J. Solid State Chem.* **94**, 87–94 (1996).

153. Albertini, F. *et al.* A magnetic and structural study of Mn , Co , and Ni substituted Fe3Ge2 hexagonal germanides. *J. Appl. Phys.* **84**, 401–410 (1998).

154. May, A. F. *et al.* Ferromagnetism Near Room Temperature in the Cleavable van der Waals Crystal Fe5GeTe2. *ACS Nano* **13**, 4436–4442 (2019).

155. Sologub, O., Rogl, P. & Giester, G. The tau-borides τ-(Fe0.54Ir0.46)20Fe3B6 and τ-(Co0.64Ir0.36)21Co0.16B4B6. *Intermetallics* **18**, 694–701 (2010).

156. Terzieff, P. The magnetism of the NiAs-type solid solution CrxFe2-xTe3. *Phys. B+C* **122**, 43–48 (1983).

157. Putintsev, Y., INORGANIC, A. G.- & 1982, undefined. ENTHALPIES OF COMPOUNDS WITH COMPOSITIONS CLOSE TO MN5GE3, FE5GE3, CO5GE3, NI5GE3 IN TEMPERATURE INTERVAL 500-1400. *233 SPRING ST, NEW YORK, NY ...*.

158. Tervieff, P., Schicketanv, H. & Komarek, K. L. The magnetic and thermoelectric properties of single-crystal Ni0.786Te. *J. Less Common Met.* **115**, 35–43 (1986).

159. Hahn, H. & Ness, P. Über das System Zirkon/Tellur. *ZAAC - J. Inorg. Gen. Chem.* **302**, 136–154 (1959).

160. Knop, O. & MacDonald, R. D. CHALKOGENIDES OF THE TRANSITION ELEMENTS: III. MOLYBDENUM DITELLURIDE. *Can. J. Chem.* **39**, 897–904 (1961).

161. Atuchin, V. V. *et al.* Structural and vibrational properties of PVT grown Bi 2Te 3 microcrystals. *Solid State Commun.* **152**, 1119–1122 (2012).

Chapter 8: Conclusion

The research summarized in this dissertation led to the discovery of four compounds (such as $Nb_{1-x}Os_{1+x}B$ and $Ti_{5-x}Fe_{1-y}Os_{6+x+y}B_6$) synthesized by various solid-state methods that crystallize in hitherto unknown crystal structures (**chapters 2** and **3**, respectively). Moreover, several new compounds in known structure types are synthesized. All of this results in the identification of a new class of complex metal-rich borides based on the AlB_2-Re_3B intergrowth and the crystallographic relations between these compounds are uncovered (in **chapter 4**). It turns out that the structures are formed by capped trigonal prisms as the primary building unit. Two of these are further combined into the secondary building unit which can be arranged into various patterns. Each of those tiling patterns observed for the SBUs corresponds to a different structure type. A general chemical formula, $(insert)A_{6-x}A'_xT_6B_{2+y}$, is developed describing all compounds that belong to this class of complex, metal-rich borides. It includes a relation that explains the presence of 1D-chains of magnetically active atoms and can explain the observed boron fragment. Establishing the structure-building principles is accompanied by identifying conditions for the electronic stability. Together, they allow the prediction of new compounds and even new structure types, some of which have very promising physical properties such as the magnetic properties of $TiFe_{1-x}Os_{2+x}B_2$ (see **chapter 5**).

The new telluride $Fe_{5-x}Ge_2Te_2$, a 2D intergrowth structure, and the silicide $Ir_{4-x}CuSi_2$ rationalized by electron counting, exhibit nicely that similar structure-building principles apply to other classes of compounds (see **chapters 6** and **7**, respectively).

The ability to predict new structure types for metal borides makes this set of structure-building principles very important and a powerful tool for future synthetic chemists. The ability to predict new crystal structures is quite rare and only certain algorithms such as USPEX can do so, but they do not provide the underlying structure-building principles. Therefore, this work is an important step for the modern solid-state chemistry of intermetallics towards the long-standing goal of materials-by-design.

Bibliography

1. Eckert, M. Max von Laue and the discovery of X-ray diffraction in 1912. *Ann. Phys.* **524**, A83–A85 (2012).

2. Bragg, W. H. & Bragg, W. L. The reflection of X-rays by crystals. *Proc. R. Soc. London. Ser. A, Contain. Pap. a Math. Phys. Character* **88**, 428–438 (1913).

3. Conway, J. H. Sphere Packings, Lattices, Codes, and Greed. in *Proceedings of the International Congress of Mathematicians* 45–56 (Birkhäuser Basel, 1995). doi:10.1007/978-3-0348-9078-6_7.

4. Weisstein, E. W. Sphere Packing.

5. Pauling, L. THE PRINCIPLES DETERMINING THE STRUCTURE OF COMPLEX IONIC CRYSTALS. *J. Am. Chem. Soc.* **51**, 1010–1026 (1929).

6. Grin', Y. N. The Intergrowth Concept as a Useful Tool to Interpret and Understand Complicated Intermetallic Structures. in *Modern Perspectives in Inorganic Crystal Chemistry* 77–96 (Springer Netherlands, 1992). doi:10.1007/978-94-011-2726-4_5.

7. Baerlocher, C., McCusker, L. & Olson, D. *Atlas of zeolite framework types*. (2007).

8. Gramlich-Meier, R. & Meier, W. M. Constituent units and framework conformations in zeolite networks. *J. Solid State Chem.* **44**, 41–49 (1982).

9. Davy, H. III. The Bakerian Lecture. An account of some new analytical researches on the nature of certain bodies, particularly the alkalies, phosphorus, sulphur, carbonaceous matter, and the acids hitherto undecompounded; with some general observations on chemical. *Philos. Trans. R. Soc. London* **99**, 39–104 (1809).

10. Berzelius, J. J. Untersuchungen über die Flussspatsaure und deren merkwürdigste Verbindungen. *Ann. Phys.* **10**, 113 (1824).

11. Pauling, L. THE ARCHITECTURE OF MOLECULES. *Proc. Natl. Acad. Sci.* **51**, 977–984 (1964).

12. Albert, B. & Hillebrecht, H. Boron: Elementary Challenge for Experimenters and Theoreticians. *Angew. Chemie Int. Ed.* **48**, 8640–8668 (2009).

13. White, M. A., Cerqueira, A. B., Whitman, C. A., Johnson, M. B. & Ogitsu, T. Determination of Phase Stability of Elemental Boron. *Angew. Chemie Int. Ed.* **54**, 3626–3629 (2015).

14. Richards, S. M. & Kaspar, J. S. The crystal structure of YB66. *Acta Crystallogr. Sect. B Struct. Crystallogr. Cryst. Chem.* **25**, 237–251 (1969).

15. Givord, D., Li, H. S. & Moreau, J. M. Magnetic properties and crystal structure of Nd2Fe14B. *Solid State Commun.* **50**, 497–499 (1984).

16. Rogl, P. Competition Between Trigonal Prisms and other Coordination Polyhedra in Borides, Carbides, Silicides and Phosphides. in *Modern Perspectives in Inorganic Crystal Chemistry* 267–278 (Springer Netherlands, 1992). doi:10.1007/978-94-011-2726-4_13.

17. Iyer, A. K., Zhang, Y., Scheifers, J. P. & Fokwa, B. P. T. Structural variations, relationships and properties of M2B metal borides. *J. Solid State Chem.* **270**, 618–635 (2019).

18. Scheifers, J. P., Zhang, Y. & Fokwa, B. P. T. Boron: Enabling Exciting Metal-Rich Structures and Magnetic Properties. *Acc. Chem. Res.* **50**, 2317–2325 (2017).

19. Rahman, M., Wang, C. C., Chen, W., Akbar, S. A. & Mroz, C. Electrical Resistivity of Titanium Diboride and Zirconium Diboride. *J. Am. Ceram. Soc.* **78**, 1380–1382 (1995).

20. Chung, H. Y. *et al.* Synthesis of ultra-incompressible superhard rhenium diboride at ambient pressure. *Science (80-.).* **316**, 436–439 (2007).

21. Wong, J. *et al.* YB66: A new soft-X-ray monochromator for synchrotron radiation. *Nucl. Inst. Methods Phys. Res. A* **291**, 243–249 (1990).

22. Lafferty, J. M. Boride cathodes. *J. Appl. Phys.* **22**, 299–309 (1951).

23. Nagamatsu, J., Nakagawa, N., Muranaka, T., Zenitani, Y. & Akimitsu, J. Superconductivity at 39 K in magnesium diboride. *Nature* **410**, 63–64 (2001).

24. Tomsic, M. *et al.* Overview of MgB_2 Superconductor Applications. *Int. J. Appl. Ceram. Technol.* **4**, 250–259 (2007).

25. Hermus, M., Yang, M., Grüner, D., DiSalvo, F. J. & Fokwa, B. P. T. Drastic Change of Magnetic Interactions and Hysteresis through Site-Preferential Ru/Ir Substitution in $Sc_2FeRu_{5-x}Ir_xB_2$. *Chem. Mater.* **26**, 1967–1974 (2014).

26. Mbarki, M., St. Touzani, R. & Fokwa, B. P. T. Unexpected Synergy between

Magnetic Iron Chains and Stacked B_6 Rings in $Nb_6Fe_{1-x}Ir_{6+x}B_8$. *Angew. Chemie Int. Ed.* **53**, 13174–13177 (2014).

27. Fokwa, B. P. T., Lueken, H. & Dronskowski, R. Rational Design of Complex Borides - One-Electron-Step Evolution from Soft to Semi-Hard Itinerant Ferromagnets in the New Boride Series Ti2FeRu5-nRhnB2 ($1 \leq n \leq 5$). *Eur. J. Inorg. Chem.* **2011**, 3926–3930 (2011).

28. Fokwa, B. P. T., Eck, B. & Dronskowski, R. Ti2Rh6B - a new boride with a double perovskite-like structure containing octahedral Rh6 cluster. *Zeitschrift für Krist.* **221**, 445–449 (2006).

29. Huang, B. *et al.* Layer-dependent ferromagnetism in a van der Waals crystal down to the monolayer limit. *Nature* **546**, 270–273 (2017).

30. Ajayan, P., Kim, P. & Banerjee, K. Two-dimensional van der Waals materials. *Phys. Today* **69**, 38–44 (2016).

31. Burch, K. S., Mandrus, D. & Park, J. G. Magnetism in two-dimensional van der Waals materials. *Nature* vol. 563 47–52 (2018).

32. Fleischauer, P. D., Lince, J. R., Bertrand, P. A. & Bauer, R. Electronic structure and lubrication properties of molybdenum disulfide: a qualitative molecular orbital approach. *Langmuir* **5**, 1009–1015 (1989).

33. Deiseroth, H.-J., Aleksandrov, K., Reiner, C., Kienle, L. & Kremer, R. K. Fe3GeTe2 and Ni3GeTe2 – Two New Layered Transition-Metal Compounds: Crystal Structures, HRTEM Investigations, and Magnetic and Electrical Properties. *Eur. J. Inorg. Chem.* **2006**, 1561–1567 (2006).

34. Gong, C. *et al.* Discovery of intrinsic ferromagnetism in two-dimensional van der Waals crystals. *Nature* **546**, 265–269 (2017).

35. Li, J. *et al.* Intrinsic magnetic topological insulators in van der Waals layered MnBi2Te4-family materials. *Sci. Adv.* **5**, eaaw5685 (2019).

36. Scheifers, J. P., Zhang, Y. & Fokwa, B. P. T. Boron: Enabling Exciting Metal-Rich Structures and Magnetic Properties. *Acc. Chem. Res.* **50**, 2317–2325 (2017).

37. Yeung, M. T., Mohammadi, R. & Kaner, R. B. Ultraincompressible, Superhard Materials. *Annu. Rev. Mater. Res.* **46**, 465–485 (2016).

38. Mori, T. Novel physical properties of rare earth higher borides. *J. Phys. Conf. Ser.* **176**, 012036 (2009).

39. Villars, P. & Calvert, L. D. *〖Person's Handbook of Crystallographic Data for Intermetallic Phases〗*. (ASM International, 1991).

40. Kuz'ma, Yu.B.; Yarmolyuk, Y. P. The crystal structure of Ti3Co5B2. *Zhurnal Strukt. Khimii* **12**, 458 (1971).

41. Ade, M., Kotzott, D. & Hillebrecht, H. Synthesis and crystal structures of the new metal-rich ternary borides Ni12AlB8, Ni12GaB8 and Ni 10.6Ga0.4B6-examples for the first B5 zig-zag chain fragment. *J. Solid State Chem.* **183**, 1790–1797 (2010).

42. Lundstrom, T. Structure, defects and properties of some refractory borides. *Pure Appl. Chem.* **57**, 1383–1390 (1985).

43. Chepiga, M.V.; Kuzma, Yu.B.; Kripyakevich, P. I. Crystal structure of the (Re, Co)7 B4 compound. *Dopovidi Akad. Nauk Ukr. RSR, Seriya A Fiz. ta Mat. Nauk.* 856–858 (1972).

44. Fokwa, B. P. T. & Hermus, M. All-Boron Planar B(6) Ring in the Solid-State Phase Ti(7) Rh(4) Ir(2) B(8). *Angew. Chemie Int. Ed.* **124**, 1734–1737 (2012).

45. Goerens, C. & Fokwa, B. P. T. The complex metal-rich boride Ti1+xRh2−x+yIr3−yB3 (x=0.68, y=1.06) with a new structure type containing B4 zigzag fragments: Synthesis, crystal chemistry and theoretical calculations. *J. Solid State Chem.* **192**, 113–119 (2012).

46. Zheng, Q. *et al.* Synthesis, crystal structure and properties of the new superconductors TaRuB and NbOsB. *J. Phys. Condens. Matter* **27**, 415701 (2015).

47. Rundqvist, S. *et al.* Crystal Structure Refinements of Ni3B, o-Ni4B3, and m-Ni4B3. *Acta Chemica Scandinavica* vol. 21 191–194 (1967).

48. Malik, Z., Grytsiv, A., Rogl, P., Giester, G. & Bursik, J. Phase relations and structural features in the system Ni-Zn-B. *J. Solid State Chem.* **198**, 150–161 (2013).

49. Mbarki, M., Touzani, R. St. & Fokwa, B. P. T. Experimental and Theoretical Investigations of the Ternary Boride NbRuB with a Layerlike Structure Type. *Eur. J. Inorg. Chem.* **2014**, 1381–1388 (2014).

50. Schob, O. & Parthé, E. AB compounds with Sc, Y and rare earth metals. I. Scandium and yttrium compounds with CrB and CsCl structure. *Acta Crystallogr.* **19**, 214–224 (1965).

51. Khazaei, M., Ranjbar, A., Arai, M., Sasaki, T. & Yunoki, S. Electronic properties and applications of MXenes: a theoretical review. *J. Mater. Chem. C* **5**, 2488–2503 (2017).

52. Dronskowski, R. & Bloechl, P. E. Crystal orbital Hamilton populations (COHP): energy-resolved visualization of chemical bonding in solids based on density-functional calculations. *J. Phys. Chem.* **97**, 8617–8624 (1993).

53. Fokwa, B. P. T. Borides: Solid-State Chemistry. in *Encyclopedia of Inorganic and Bioinorganic Chemistry* 1–14 (John Wiley & Sons, Ltd, 2014). doi:10.1002/9781119951438.eibc0022.pub2.

54. Mbarki, M., Touzani, R. S., Rehorn, C. W. G., Gladisch, F. C. & Fokwa, B. P. T. New ternary tantalum borides containing boron dumbbells: Experimental and theoretical studies of Ta2OsB2 and TaRuB. *J. Solid State Chem.* **242**, 28–33 (2016).

55. Rodriguez-Carvajal, J. *FULLPROF 2000: A Rietveld Refinement and Pattern Matching Analysis Program*. *Abstract of the Satellite Meeting on Powder Diffraction of the XV Congress of the IUCr, Toulouse, France* (2008).

56. Sheldrick, G. M. A short history of SHELX. *Acta Crystallogr. Sect. A Found. Crystallogr.* **64**, 112–122 (2008).

57. Sheldrick, G. M. Crystal structure refinement with SHELXL. *Acta Crystallogr. Sect. C Struct. Chem.* **71**, 3–8 (2015).

58. Sheldrick, G. M. SADABS, Program for Empirical Absorption Correction of Area Detector Data; Göttingen, Germany, 1996. (1996).

59. Kresse, G. & Joubert, D. From ultrasoft pseudopotentials to the projector augmented-wave method. *Phys. Rev. B* **59**, 1758–1775 (1999).

60. Blöchl, P. E. Projector augmented-wave method. *Phys. Rev. B* **50**, 17953–17979 (1994).

61. Perdew, J. P., Burke, K. & Ernzerhof, M. Generalized Gradient Approximation Made Simple. *Phys. Rev. Lett.* **77**, 3865–3868 (1996).

62. Tank, R. W. & Jepsen, O. The STUTTGART TB-LMTO-ASA program. *Cell* 1–27 (1998).

63. Kohn, W. & Sham, L. J. Self-consistent equations including exchange and

correlation effects. *Phys. Rev.* **140**, 1133–1138 (1965).

64. Lowdin, P.-O. A Note on the Quantum-Mechanical Perturbation Theory. *J. Chem. Phys.* **19**, 1396–1171 (1951).

65. Chung, H. Y. *et al.* Synthesis of ultra-incompressible superhard rhenium diboride at ambient pressure. *Science (80-.).* **316**, 436–439 (2007).

66. Fokwa, B. P. T., Lueken, H. & Dronskowski, R. Rational synthetic tuning between itinerant antiferromagnetism and ferromagnetism in the complex boride series Sc2FeRu 5-nRhnB2($0 \leq n \leq 5$). *Chem. - A Eur. J.* **13**, 6040–6046 (2007).

67. Hermus, M., Yang, M., Grüner, D., DiSalvo, F. J. & Fokwa, B. P. T. Drastic Change of Magnetic Interactions and Hysteresis through Site-Preferential Ru/Ir Substitution in $Sc_2FeRu_{5-x}Ir_xB_2$. *Chem. Mater.* **26**, 1967–1974 (2014).

68. Shankhari, P., Zhang, Y., Stekovic, D., Itkis, M. E. & Fokwa, B. P. T. Unexpected Competition between Antiferromagnetic and Ferromagnetic States in Hf2MnRu5B2: Predicted and Realized. *Inorg. Chem.* **56**, 12674–12677 (2017).

69. Fokwa, B. P. T., Samolyuk, G. D., Miller, G. J. & Dronskowski, R. Ladders of a Magnetically Active Element in the Structure of the Novel Complex Boride $Ti_9Fe_2Ru_{18}B_8$: Synthesis, Structure, Bonding, and Magnetism. *Inorg. Chem.* **47**, 2113–2120 (2008).

70. Küpers, M., Lutz-Kappelman, L., Zhang, Y., Miller, G. J. & Fokwa, B. P. T. Spin Frustration and Magnetic Ordering from One-Dimensional Stacking of Cr_3 Triangles in $TiCrIr_2B_2$. *Inorg. Chem.* **55**, 5640–5648 (2016).

71. Scheifers, J. P., Zhang, Y. & Fokwa, B. P. T. Boron: Enabling Exciting Metal-Rich Structures and Magnetic Properties. *Acc. Chem. Res.* **50**, 2317–2325 (2017).

72. Rodriguez-Carvajal, J. FullProf: A Program for Rietveld Refinement and Profile Matching Analysis of Complex Powder Diffraction Patterns. in *Satellite Meeting on Powder Diffraction of the XV Congress of the IUCr* 127 (1990).

73. Rodríguez-Carvajal, J. Recent advances in magnetic structure determination by neutron powder diffraction. *Phys. B Condens. Matter* **192**, 55–69 (1993).

74. Roisnel, T. & Rodriguez-Carvajal, J. WinPLOTR: a Windows tool for powder diffraction patterns analysis. in *Materials Science Forum, Proceedings of the Seventh European Powder Diffraction Conference (EPDIC 7)* (eds. Delhez, R. & Mittenmeijer, E. J.) 118–123 (2000).

75. Farrugia, L. J. WinGX suite for small-molecule single-crystal crystallography. *J.*

Appl. Crystallogr. **32**, 837–838 (1999).

76. Farrugia, L. J. WinGX and ORTEP for Windows : an update. *J. Appl. Crystallogr.* **45**, 849–854 (2012).

77. Kresse, G. Vienna ab initio simulation package. (1999).

78. Kresse, G. & Hafner, J. Ab initio molecular dynamics for liquid metals. *Phys. Rev. B* **47**, 558–561 (1993).

79. Monkhorst, H. J. & Pack, J. D. Special points for Brillouin-zone integrations. *Phys. Rev. B* **13**, 5188–5192 (1976).

80. Decker, B. F. & Kasper, J. S. The crystal structure of TiB. *Acta Crystallogr.* **7**, 77–80 (1954).

81. Hirt, S., Hilfinger, F. & Hillebrecht, H. Synthesis and crystal structures of the new ternary borides Fe3Al2B2 and Ru9Al3B8 and the confirmation of Ru4Al3B2 and Ru9Al5B8-x (x ≈ 2). *Zeitschrift fur Krist. - Cryst. Mater.* **233**, 295–307 (2018).

82. Forsythe, R., Scheifers, J. P., Zhang, Y. & Fokwa, B. P. T. HT-NbOsB: Experimental and Theoretical Investigations of a Boride Structure Type Containing Boron Chains and Isolated Boron Atoms. *Eur. J. Inorg. Chem.* **2018**, (2018).

83. Hartung, H., Schiffer, J., Nagelschmitz, E. A. & Jung, W. Synthese und Kristallstrukturen des Zink-Rhodiumborids Zn5Rh8B4 und der Lithium-Magnesium-Rhodiumboride LixMg5−xRh8B4 (x = 1.1 und 0.5) und Li8Mg4Rh19B12. *Zeitschrift für Anorg. und Allg. Chemie* **633**, 1645–1650 (2007).

84. Eibenstein, U. & Jung, W. Zn11Rh18B8 and Zn10MRh18B8 with M = Sc, Ti, V, Cr, Mn, Fe, Co, Ni, Cu, Al, Si, Ge, Sn - New Ternary and Quaternary Zinc Rhodium Borides. *Zeitschrift für Anorg. und Allg. Chemie* **624**, 802–806 (1998).

85. Houben, A. *et al.* Synthesis, crystal structure, and magnetic properties of the semihard itinerant ferromagnet RhFe3N. *Angew. Chemie - Int. Ed.* **44**, 7212–7215 (2005).

86. Shankhari, P., Scheifers, J. P., Hermus, M., Yubuta, K. & Fokwa, B. P. T. Unexpected Trend Deviation in Isoelectronic Transition Metal Borides A3T5B2 (A = group 4, T = group 9): Ti3Co5B2- vs. Perovskite-Type Studied by Experiments and DFT Calculations. *Zeitschrift fur Anorg. und Allg. Chemie* **643**, (2017).

87. Glass, C. W., Oganov, A. R. & Hansen, N. USPEX-Evolutionary crystal structure prediction. *Comput. Phys. Commun.* **175**, 713–720 (2006).

88. Hellenbrandt, M. The inorganic crystal structure database (ICSD) - Present and future. in *Crystallography Reviews* vol. 10 17–22 (Taylor & Francis, 2004).

89. Fokwa, B. P. T. Borides: Solid-State Chemistry. in *Encyclopedia of Inorganic and Bioinorganic Chemistry* 1–14 (John Wiley & Sons, Ltd, 2014). doi:10.1002/9781119951438.eibc0022.pub2.

90. Zheng, Q. *et al.* Ternary borides Nb7Fe3B8 and Ta7Fe3B8 with Kagome-type iron framework. *Dalt. Trans.* **45**, 9590–9600 (2016).

91. Ade, M. & Hillebrecht, H. Ternary Borides Cr_2AlB_2, Cr_3AlB_4, and Cr_4AlB_6: The First Members of the Series $(CrB_2)_nCrAl$ with $n = 1, 2, 3$ and a Unifying Concept for Ternary Borides as MAB-Phases. *Inorg. Chem.* **54**, 6122–6135 (2015).

92. Kota, S. *et al.* Synthesis and characterization of an alumina forming nanolaminated boride: MoalB. *Sci. Rep.* **6**, 1–11 (2016).

93. Hillebrecht, H. & Gebhardt, K. Crystal Structures from a Building Set: The First Boridecarbides of Niobium. *Angew. Chemie Int. Ed.* **40**, 1445–1447 (2001).

94. Kuzma, Y., Tsolkovskii, T. & Baburova, O. The Systems Nb-Fe-B and Nb-Co-B. *Inorg. Mater.* **4**, 950–953 (1968).

95. Kuzma, Y. B. CRYSTAL STRUCTURES OF NbFeB AND TaFeB COMPOUNDS,. (1969).

96. Sharma, N., Mbarki, M., Zhang, Y., Huq, A. & Fokwa, B. P. T. Structural-Distortion-Driven Magnetic Transformation from Ferro- to Ferrimagnetic Iron Chains in B_6-based $Nb_6FeIr_6B_8$. *Angew. Chemie Int. Ed.* **57**, 10323–10327 (2018).

97. Xie, W. *et al.* Fragment-based design of NbRuB as a new metal-rich boride superconductor. *Chem. Mater.* **27**, 1149–1152 (2015).

98. Scheifers, J. P. *et al.* Transformation of trigonal planar B 4 into zigzag B 4 unit within the new boride series (Ti 1–x M x) 3 Ir 3 B 3 (x = ½ for M = V-Mn and x = ⅓ for M = Mn- Ni). *Solid State Sci.* (2020).

99. Fokwa, B. P. T., Von Appen, J. & Dronskowski, R. Synthesis of a missing

structural link: The first trigonal planar B 4 units in the novel complex boride Ti1+xOs 2-xRuB2 (x = 0.6). *Chem. Commun.* 4419–4421 (2006) doi:10.1039/b608903h.

100. Mbarki, M., Touzani, R. S. & Fokwa, B. P. T. Experimental and theoretical investigations of the ternary boride NbRuB with a layerlike structure type. *Eur. J. Inorg. Chem.* 1381–1388 (2014) doi:10.1002/ejic.201301488.

101. Goerens, C. & Fokwa, B. P. T. The complex metal-rich boride Ti 1xRh 2-xyIr 3-yB 3 (x=0.68, y=1.06) with a new structure type containing B 4 zigzag fragments: Synthesis, crystal chemistry and theoretical calculations. *J. Solid State Chem.* **192**, 113–119 (2012).

102. Andersson, S. & Hyde, B. G. Twinning on the unit cell level as a structure-building operation in the solid state. *J. Solid State Chem.* **9**, 92–101 (1974).

103. Ivantchev, S., Kroumova, E., Madariaga, G., Pérez-Mato, J. M. & Aroyo, M. I. SUBGROUPGRAPH: A computer program for analysis of group-subgroup relations between space groups. *J. Appl. Crystallogr.* **33**, 1190–1191 (2000).

104. Sologub, O. L., Hester, J. R., Salamakha, P. S., Leroy, E. & Godart, C. Ab initio structure determination of new boride CePt 3 B, a distorted variant of CaTiO 3. **337**, 10–17 (2002).

105. Kluenter, W. & Jung, W. In3Ir3B, In3Rh3B and In5Ir9B4, the First Indium Platinum Metal Borides. *ChemInform* **37**, no-no (2006).

106. Mirgel, R. & Jung, W. The ternary alkali metal platinum borides LiPt3B, NaPt3B1+x and Na3Pt9B5 - new structure variants of the CeCo3B2 type. *J. Less-Common Met.* **144**, 87–99 (1988).

107. Petry, K., Klünter, W. & Jung, W. Zn3Pt9B4, Ga2, 7Ir9B5und Ga3Pt9B4, Zink- und Gallium-Übergangs-metallboride mit neuen Kanalstrukturen. *Zeitschrift fur Krist. - New Cryst. Struct.* **209**, 151–156 (1994).

108. Eibenstein, U., Klünter, W. & Jung, W. Zn5Ir7B3, Zn5Rh7B3 und Zn7+xRh9–xB3 (x≈0,4) – neue ternäre Zink-Platinmetallboride. *Zeitschrift für Anorg. und Allg. Chemie* **625**, 719–724 (1999).

109. Fokwa, B. P. T. & Hermus, M. All-Boron Planar B6 Ring in the Solid-State Phase Ti7Rh4Ir2B8. *Angew. Chemie Int. Ed.* **51**, 1702–1705 (2012).

110. Zheng, Q. *et al.* TM 7 TM' 6B 8 (TM = Ta, Nb; TM' = Ru, Rh, Ir): New compounds with [B 6] ring polyanions. *Inorg. Chem.* **51**, 7472–7483 (2012).

111. Aronsson, B., Bäckman, M., Rundqvist, S., Varde, E. & Westin, G. The Crystal Structure of Re3B. *Acta Chem. Scand.* **14**, 1001–1005 (1960).

112. Konrad, T. & Jeitschko, W. U5Mo10B24, a boride containing three different kinds of boron polyanions. *Journal of Alloys and Compounds* vol. 233 (1996).

113. Küpers, M., Lutz-Kappelman, L., Zhang, Y., Miller, G. J. & Fokwa, B. P. T. Spin Frustration and Magnetic Ordering from One-Dimensional Stacking of Cr_3 Triangles in $TiCrIr_2B_2$. *Inorg. Chem.* **55**, 5640–5648 (2016).

114. Fokwa, B. P. T., Von Appen, J. & Dronskowski, R. Synthesis of a missing structural link: The first trigonal planar B 4 units in the novel complex boride Ti1+xOs 2-xRuB2 (x = 0.6). *Chem. Commun.* 4419–4421 (2006) doi:10.1039/b608903h.

115. Clark, R. C. & Reid, J. S. The analytical calculation of absorption in multifaceted crystals. *Acta Crystallogr. Sect. A Found. Crystallogr.* **51**, 887–897 (1995).

116. Farrugia, L. J. WinGX suite for small-molecule single-crystal crystallography. *J. Appl. Crystallogr.* **32**, 837–838 (1999).

117. Spek, A. L. Single-crystal structure validation with the program PLATON. *J. Appl. Crystallogr.* **36**, 7–13 (2003).

118. Momma, K. & Izumi, F. VESTA 3 for three-dimensional visualization of crystal, volumetric and morphology data. *J. Appl. Crystallogr.* **44**, 1272–1276 (2011).

119. Perdew, J. P., Burke, K. & Ernzerhof, M. Generalized Gradient Approximation Made Simple. *Phys. Rev. Lett.* **77**, 3865–3868 (1996).

120. Takeya, H., Shishido, T. & Takei, H. Studies on the perovskite solid solution Er(Rh, M)3By (M ≡ Pd, Pt and $0 \leq y \leq 1$). *J. Less-Common Met.* **134**, 263–273 (1987).

121. Landrum, G. A. & Dronskowski, R. The Orbital Origins of Magnetism: From Atoms to Molecules to Ferromagnetic Alloys. *Angew. Chemie Int. Ed.* **39**, 1560–1585 (2000).

122. Dronskowski, R. Itinerant ferromagnetism and antiferromagnetism from the perspective of chemical bonding. *Int. J. Quantum Chem.* **96**, 89–94 (2004).

123. Engstroem, I. & Johnsson, T. The crystal structure of Ru4Si3. *Ark. foer Kemi* **30**, 141–147 (1968).

124. Andersson, S. & Hyde, B. G. Twinning on the unit cell level as a structure-building operation in the solid state. *J. Solid State Chem.* (1974) doi:10.1016/0022-4596(74)90059-0.

125. Hyde, B. G., Andersson, S., Bakker, M., Plug, C. M. & O'Keeffe, M. The (twin) composition plane as an extended defect and structure-building entity in crystals. *Progress in Solid State Chemistry* (1979) doi:10.1016/0079-6786(79)90002-5.

126. Parthé, E. *Modern Perspectives in Inorganic Crystal Chemistry*. (Springer Netherlands, 1992).

127. Mielke, A., Rieger, J. J., Scheidt, E. W. & Stewart, G. R. Important role of coherence for the heavy-fermion state in CeCu2Si2. *Phys. Rev. B* **49**, 10051–10053 (1994).

128. Eriksson, T. *et al.* Cycloidal magnetic order in the compound IrMnSi. *Phys. Rev. B* **71**, 174420 (2005).

129. Eriksson, T. *et al.* Crystal and magnetic structure of Mn3IrSi. *Phys. Rev. B - Condens. Matter Mater. Phys.* **69**, (2004).

130. Sales, B. C. *et al.* Magnetic, transport, and structural properties of Fe1-xIrxSi. *Phys. Rev. B* **50**, 8207–8213 (1994).

131. Kimmel, G. On the U3Si (Doc) crystallographic type. *J. Less Common Met.* **59**, P83–P86 (1978).

132. Bhan, S. & Schubert, K. Zum Aufbau der Systeme Kobalt-Germanium, Rhodium-Silizium sowie einiger verwandter Legierungen. *ZEITSCHRIFT FUR Met.* **51**, 327–339 (1960).

133. Schubert, K. *et al.* Einige strukturelle Ergebnisse an metallischen Phasen (5). *Naturwissenschaften* **47**, 303–303 (1960).

134. Finnie, L. N. Structures and compositions of the silicides of ruthenium, osmium, rhodium and iridium. *J. Less Common Met.* **4**, 24–34 (1962).

135. Andersson, S., Leygraf, C. & Johnsson, T. The structure of defect Ru4Si3. *J. Solid State Chem.* **14**, 78–84 (1975).

136. Weitzer, F., Rogl, P. & Schuster, J. C. X-ray investigations in the systems ruthenium-silicon and ruthenium-silicon-nitrogen. *Zeitschrift fuer Met.* **79**, 154–156 (1988).

137. Straumanis, M. E. & Yu, L. S. Lattice parameters, densities, expansion coefficients and perfection of structure of Cu and of Cu–In α phase. *Acta Crystallogr. Sect. A* **25**, 676–682 (1969).

138. Klünter, W. & Jung, W. Das Kupfer-Iridiumborid Cu2Ir4B3 mit einer vom ZnIr4B3-Typ abgeleiteten Schichtstruktur. *Zeitschrift für Anorg. und Allg. Chemie* **626**, 502–505 (2000).

139. Weller, M. T. & Lines, D. R. Structure and oxidation state relationships in ternary copper oxides. *J. Solid State Chem.* **82**, 21–29 (1989).

140. Slater, J. C. Atomic Radii in Crystals. *J. Chem. Phys.* **41**, 3199–3204 (1964).

141. Farrugia, L. J. WinGX and ORTEP for Windows: An update. *J. Appl. Crystallogr.* **45**, 849–854 (2012).

142. Kresse, G. & Joubert, D. From ultrasoft pseudopotentials to the projector augmented-wave method. *Phys. Rev. B* **59**, 1758–1775 (1999).

143. Li, H., Ruan, S. & Zeng, Y. J. Intrinsic Van Der Waals Magnetic Materials from Bulk to the 2D Limit: New Frontiers of Spintronics. *Advanced Materials* vol. 31 (2019).

144. Gibertini, M., Koperski, M., Morpurgo, A. F. & Novoselov, K. S. Magnetic 2D materials and heterostructures. *Nature Nanotechnology* vol. 14 408–419 (2019).

145. Kong, T. *et al.* VI 3 —a New Layered Ferromagnetic Semiconductor. *Adv. Mater.* **31**, (2019).

146. Spirovski, F., Reiner, C., Deiseroth, H.-J., Kienle, L. & Mikus, H. M3GeTe2 and M5GeTe2 – new layered tellurides (M = Fe, Ni). *Zeitschrift für Anorg. und Allg. Chemie* **632**, 2103–2103 (2006).

147. Merker, H.-B., Schfer, H. & Krebs, B. Neue PdxAly-Phasen und die Verbindung Pd5AII2. *Zeitschrift fur Anorg. und Allg. Chemie* **462**, 49–56 (1980).

148. Spirovski, F., Reiner, C., Deiseroth, H.-J., Kienle, L. & Mikus, H. M3GeTe2 and M5GeTe2 – new layered tellurides (M = Fe, Ni). *Zeitschrift für Anorg. und Allg. Chemie* **632**, 2103–2103 (2006).

149. Sheldrick, G. M. A short history of SHELX. *Acta Crystallographica Section A: Foundations of Crystallography* vol. 64 112–122 (2008).

150. Rodríguez-Carvajal, J. Recent advances in magnetic structure determination by

neutron powder diffraction. *Phys. B Phys. Condens. Matter* **192**, 55–69 (1993).

151. Stahl, J., Shlaen, E. & Johrendt, D. The van der Waals Ferromagnets Fe5-δGeTe2 and Fe5-δ-xNixGeTe2 - Crystal Structure, Stacking Faults, and Magnetic Properties. *Zeitschrift für Anorg. und Allg. Chemie* **644**, 1923–1929 (2018).

152. Bensch, W. *et al.* Anionic Polymeric Bonds in Nickel Ditelluride : Crystal Structure , and Experimental and Theoretical Band Structure. *J. Solid State Chem.* **94**, 87–94 (1996).

153. Albertini, F. *et al.* A magnetic and structural study of Mn , Co , and Ni substituted Fe3Ge2 hexagonal germanides. *J. Appl. Phys.* **84**, 401–410 (1998).

154. May, A. F. *et al.* Ferromagnetism Near Room Temperature in the Cleavable van der Waals Crystal Fe5GeTe2. *ACS Nano* **13**, 4436–4442 (2019).

155. Sologub, O., Rogl, P. & Giester, G. The tau-borides τ-(Fe0.54Ir0.46)20Fe3B6 and τ-(Co0.64Ir0.36)21Co0.16B4B6. *Intermetallics* **18**, 694–701 (2010).

156. Terzieff, P. The magnetism of the NiAs-type solid solution CrxFe2-xTe3. *Phys. B+C* **122**, 43–48 (1983).

157. Putintsev, Y., INORGANIC, A. G.- & 1982, undefined. ENTHALPIES OF COMPOUNDS WITH COMPOSITIONS CLOSE TO MN5GE3, FE5GE3, CO5GE3, NI5GE3 IN TEMPERATURE INTERVAL 500-1400. *233 SPRING ST, NEW YORK, NY ...*.

158. Tervieff, P., Schicketanv, H. & Komarek, K. L. The magnetic and thermoelectric properties of single-crystal Ni0.786Te. *J. Less Common Met.* **115**, 35–43 (1986).

159. Hahn, H. & Ness, P. Über das System Zirkon/Tellur. *ZAAC - J. Inorg. Gen. Chem.* **302**, 136–154 (1959).

160. Knop, O. & MacDonald, R. D. CHALKOGENIDES OF THE TRANSITION ELEMENTS: III. MOLYBDENUM DITELLURIDE. *Can. J. Chem.* **39**, 897–904 (1961).

161. Atuchin, V. V. *et al.* Structural and vibrational properties of PVT grown Bi 2Te 3 microcrystals. *Solid State Commun.* **152**, 1119–1122 (2012).

Appendices

Table S1: *Parameters of the Rietveld powder refinement of $Nb_{(1-x)}Os_{(1+x)}B$.*

Phase	$Nb_{(1-x)}Os_{(1+x)}B$	Os
space group, *Z*	*Pnma (no. 61); 6*	$P\frac{63}{m}mc$ *(no. 194); 1*
a (Å)	11.2782(6)	2.7352(1)
b (Å)	3.003(2)	-
c (Å)	12.901(7)	4.3296(3)
V (Å^3)	436.9(4)	28.051(2)
2θ-range (°)	10-82.9	
refinement method	least squares method	
profile function	pseudo-Voigt	
R_{Bragg}	6.89	7.89
Weight fraction (wt.-%)	62.4(9) [a)]	37.6(3) [a)]

a) relative due to unidentified reflections in the powder XRD data

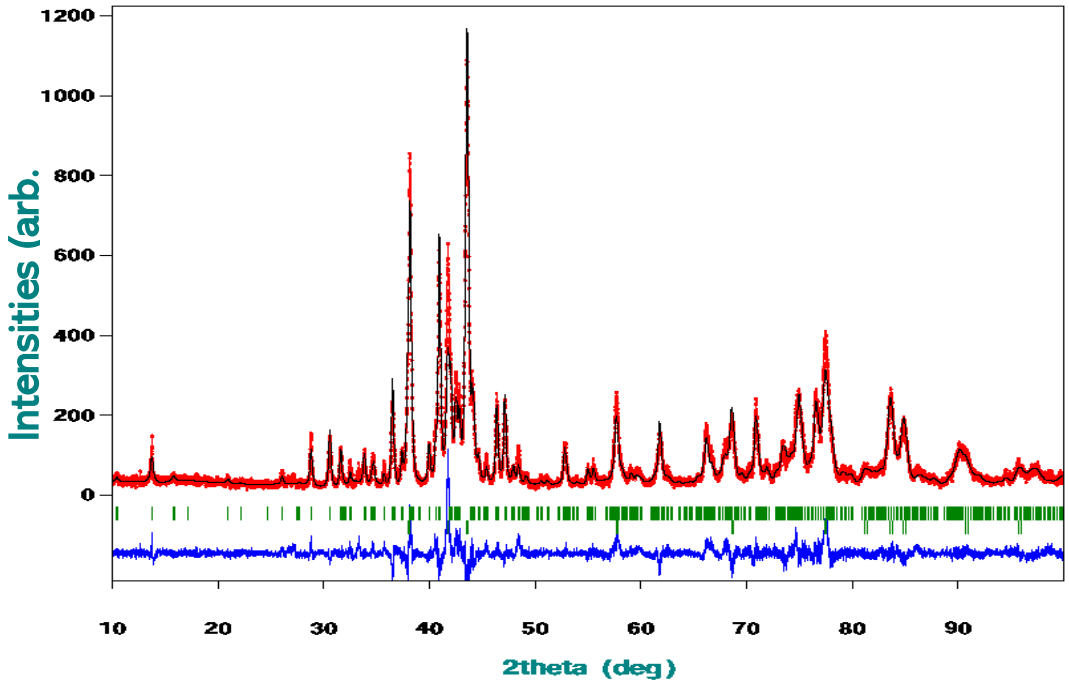

Figure S2 *Rietveld refinement of the powder data for $Nb_{(1-x)}Os_{(1+x)}B$, showing measured (red) and fitted intensities (black). The green lines are the position of the Bragg reflections for the product and osmium metal. The difference intensity curve is in blue. A small peak at 33° could not be matched to any existing phases in the ICSD database.*

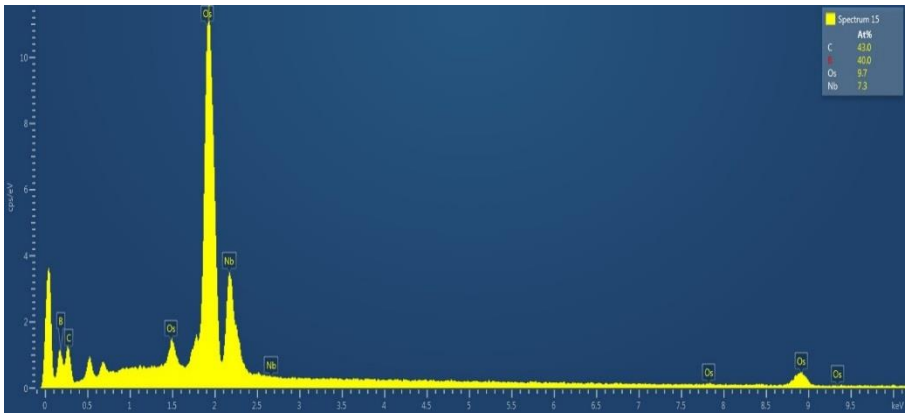

Figure S3 *EDX spectra for a $Nb_{(1-x)}Os_{(1+x)}B$ single crystal, which supports an excess of osmium.*

Table S4 *List of nearest neighbor interactions in the crystal structure of $Nb_{(1-x)}Os_{(1+x)}B$.*

Bond	D_{exp}, Å	Avg -ICOHP
Nb2-Os3	2.748	1.00812
Os1-Os3	2.759	0.689815
Nb3-Os3	2.802	0.79247
Nb3-Os2	2.807	0.78628
Nb2-Os1	2.81	0.844375
Nb1-Os1	2.813	0.861655
Nb3-Os1	2.837	0.762945
Nb1-Os2	2.839	0.90914
Nb2-Os2	2.84	0.8805
Os2-Os3	2.857	0.81492
Nb1-Os3	2.87	0.866215
Os1-Os2	2.882	0.530345
Nb1-Os1	2.885	0.679085
Os2-Os3	2.894	0.476225
Nb2-Nb3	2.949	0.59165
Nb1-Nb1	2.977	0.660515
Nb1-Nb1	3.01	0.62526
Nb2-Nb2	3.01	0.57203
Nb3-Nb3	3.01	0.530715
Os2-Os2	3.01	0.521185
Os3-Os3	3.01	0.49458
Os1-Os1	3.01	0.413965
Nb2-Nb3	3.158	0.79247

Bond	D_{exp}, Å	Avg -ICOHP
B2-B2	1.77	3.647715
Os1-B3	2.163	1.716575
Os3-B1	2.18	1.665145
Os2-B1	2.2	1.627185
Nb2-B2	2.29	1.14139
Os1-B1	2.31	1.25398
Nb2-B2	2.33	0.936485
Nb3-B2	2.36	1.01642
Nb1-B3	2.38	1.097375
Os2-B3	2.38	1.057445
Nb3-B3	2.43	0.967645
Os3-B2	2.51	0.68019
Nb3-B1	2.54	0.702265

Table S5. *Anisotropic displacement parameters ($Å^2$ x 10^3) for $Ti_{4.34(1)}Fe_{0.73(1)}Os_{6.93(2)}B_6$. The anisotropic displacement factor exponent takes the form: $-2p^2[h^2a^{*2}U^{11} + ... + 2 h k a^* b^* U^{12}]$. The B-atoms are refined isotropically.*

Site	U^{11}	U^{22}	U^{33}	U^{23}	U^{13}	U^{12}
Os1	7(1)	6(1)	6(1)	0(1)	0	0
Os2	6(1)	7(1)	5(1)	-1(1)	0	0
Os3	7(1)	7(1)	5(1)	0(1)	0	0
T1	6(2)	12(2)	14(2)	4(1)	0	0
T2	14(2)	22(2)	14(2)	-1(1)	0	0
Ti	3(3)	7(4)	6(3)	0	0	0
M	1(2)	6(2)	3(2)	0	0	0

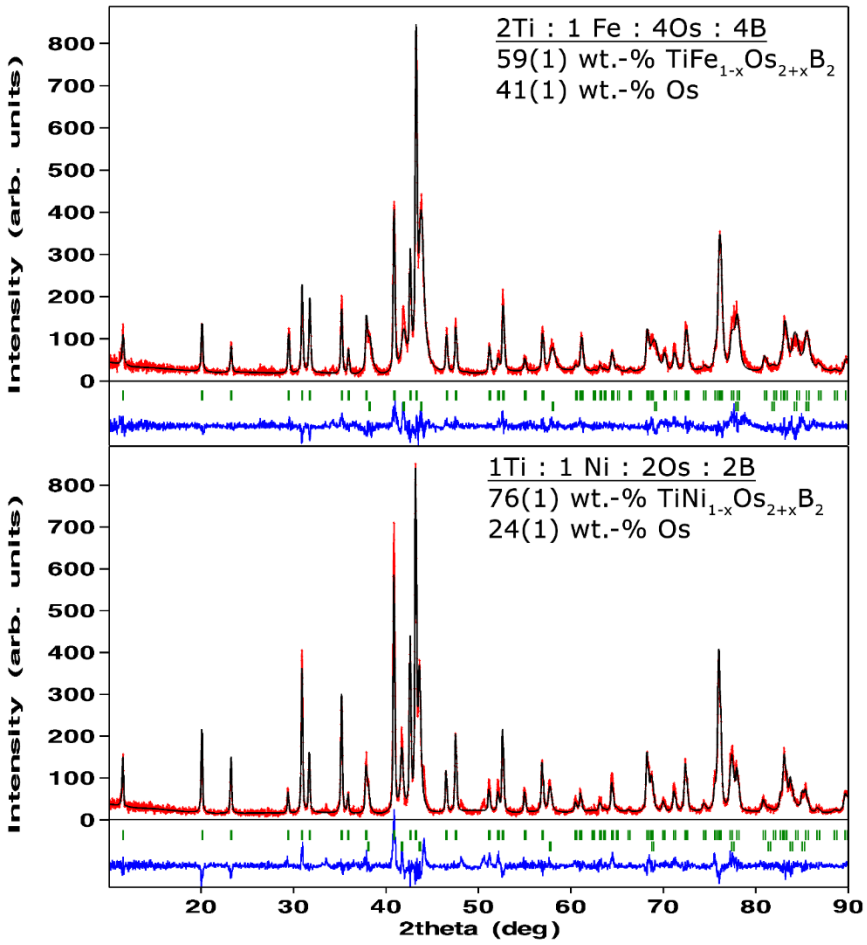

***Figure S6**: graphical summary of two Rietveld refinements (top: M = Fe, bottom M = Ni), the experimental data in red, fitted profile in black, difference curve in blue and the tick marks of the peak positions in green (top row tick marks correspond to $TiM_{1-x}Os_{2+x}B_2$, bottom row corresponds to Os, respectively).*

***Table S7**: Anisotropic displacement parameters (in Å^2) for $TiFe_{1-x}Os_{2+x}B_2$ (top) and $TiNi_{1-x}Os_{2+x}B_2$(bottom). The anisotropic displacement factor exponent takes the form: $-2\pi^2[h^2a^{*2}U_{11} + ... + 2hka^*b^*U_{12}]$.*

$TiFe_{1-x}Os_{2+x}B_2$	U_{11}	U_{22}	U_{33}	U_{23}	U_{13}	U_{12}
Os2	0.002(1)	0.003(1)	0.007(1)	0	0	0.001(1)
Fe1/Os1	0.005(1)	0.005(1)	0.014(1)	0	0	0.002(1)
Ti1	0.003(2)	0.004(2)	0.005(2)	0	0	0.001(1)
$TiNi_{1-x}Os_{2+x}B_2$	U_{11}	U_{22}	U_{33}	U_{23}	U_{13}	U_{12}
Os2	0.004(1)	0.004(1)	0.007(1)	0	0	0.002(1)
Ni1/Os1	0.007(1)	0.007(1)	0.013(2)	0	0	0.004(1)
Ti1	0.007(3)	0.006(3)	0.004(3)	0	0	0.003(2)

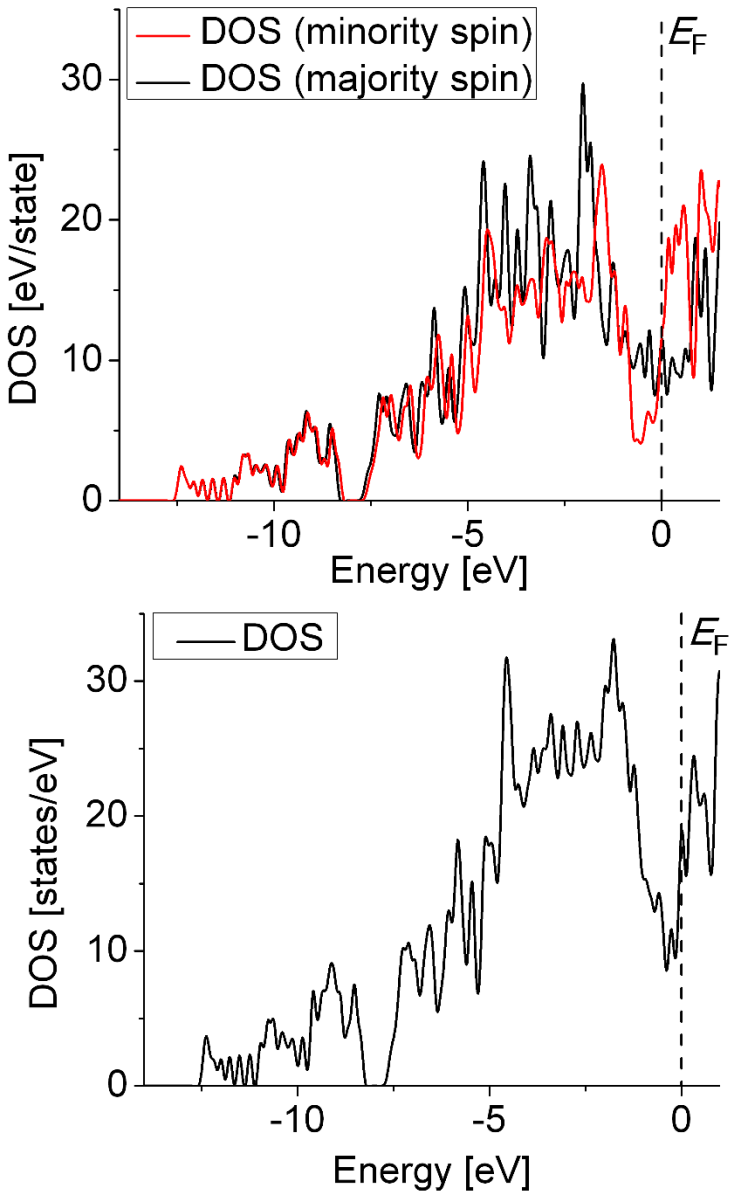

***Figure S8**: Spin-polarized partial DOS of Fe in $TiFe_{1-x}Os_{2+x}B_2$ and the total DOS of $TiFe_{1-x}Os_{2+x}B_2$ after spin-polarization.*